

3D PHOTOACOUSTIC TOMOGRAPHY IN AN ENDOSCOPIC FORM
FACTOR

by

Taylor G. Landry

Submitted in partial fulfillment of the requirements
for the degree of Master of Applied Science

at

Dalhousie University
Halifax, Nova Scotia
October 2020

© Copyright by Taylor G. Landry, 2020

Table of Contents

List of Tables	iv
List of Figures	v
Abstract	x
Acknowledgements	xi
Chapter 1 Introduction	1
1.1 Potential Clinical Applications of Endoscopic PAT	3
1.2 The Photoacoustic Effect	4
1.3 Diode Laser as Pulsed Light Source	5
Chapter 2 Thesis Objectives	8
Chapter 3 Proof of Principle and Beamforming	10
3.1 Selecting a Phantom Imaging Target	13
3.2 Focusing Optics	13
3.3 The Photoacoustic Signal from a Cylindrical Source	16
3.4 Single Element Transducer Experiment and Results	19
3.5 40 MHz 64-Element Phased Array Ultrasound Transducer Experiment	25
3.5.1 Ultrasound System Host Software Update for Photoacoustics	26
3.5.2 Image Processing	26
3.5.3 Images of Hair Target with 40 MHz Transducer	29
Chapter 4 Tissue-mimicking Phantom	32
4.1 Tissue Properties and Materials	32
4.2 Phantom Fabrication Procedure	37
4.3 Verification of Phantom Properties	42
4.3.1 Backscattering of Ultrasound	42
4.3.2 Estimate of Scattering Coefficient	47

Chapter 5	Handheld 3D Photoacoustic Imaging	53
5.1	Fiber Optic Cables and Materials	53
5.2	Optical Coupling	58
5.3	Fabrication Process for Fibers	61
5.3.1	Fabrication of Transducer End	62
5.3.2	Fabrication of Fiber Bundle End	63
5.4	Fabrication of the Photoacoustic Endoscopic 40MHz 2D Array and 30MHz 3D Array Transducers	67
5.4.1	2D Ultrasound and Photoacoustic Imaging with Tissue Mimicking Phantom	68
5.5	Photoacoustic 3D Imaging	71
5.5.1	3D Photoacoustic Imaging with Side illumination	71
5.5.2	3D Photoacoustic Imaging with coupled fiber optics	72
Chapter 6	Conclusion	76
Appendix A	Image Improvement Through Adaptive Beamforming	82
Appendix B	Copyright Agreement Letters	84
B.1	Figure 1.1	84
B.2	Figure 1.2	85
B.3	Figure 1.4	86
B.4	Figure 3.4	87
B.5	Figure 3.15	88
B.6	Figure 4.1	89
B.7	Figure 4.5	90
Bibliography		91

List of Tables

4.1	Phantom Fabrication Procedure	39
5.1	Transducer End Fiber Fabrication Procedure	63
5.2	Fiber Bundle Fabrication Procedure	66

List of Figures

Figure 1.1	An image of fast functional photoacoustic microscopy of the mouse brain from an experiment by Yao, Wang, et. al. [37]. The left shows a representative x-y projected brain vasculature image through in intact skull. The middle shows the x-z projected brain vasculature image. Finally, the right image shows photoacoustic microscopy of oxygen saturation (sO_2) of hemoglobin in the mouse brain. Where red vessels have a high oxygen (arteries) saturation and blue/green regions have low oxygen saturation (veins). SV = skull vessel.	2
Figure 1.2	Example of a simulated (left) and experimental (right) pressure plot from a cylindrical photoacoustic target [15]. Where p is the pressure and $\hat{\tau}$ is the dimensionless retarded time.	5
Figure 1.3	An image of the 808nm diode laser used in this project.	7
Figure 1.4	a) The diodes bars of our laser that make up the total laser output. b) An example of a diode bar [8] © 1992 IEEE.	7
Figure 3.1	The ultrasound system inner electronics.	11
Figure 3.2	A diagram of the experimental setup.	12
Figure 3.3	A picture of the experimental setup.	12
Figure 3.4	The absorption spectra of major absorbing substances in tissue [38].	14
Figure 3.5	An image of the output of the laser in the near field.	14
Figure 3.6	A diagram of the front face of the laser diode.	15
Figure 3.7	A diagram of the focusing system.	16
Figure 3.8	Simulated impulse response of a hair target with a delta function pulse.	17
Figure 3.9	Simulated photoacoustic signal resulting from the convolution of the gaussian pulse and the photoacoustic signal from a delta function excitation.	18
Figure 3.10	Simulated frequency spectrum of the photoacoustic signal resulting from the convolution of the gaussian pulse and the photoacoustic signal from a delta function.	18
Figure 3.11	The 22 MHz 8-element annular array with the element we used indicated (left) and the full annular array transducer assembled (right).	20

Figure 3.12	Raw oscilloscope results from the single-element ultrasound transducer (left) and oscilloscope results from the single-element ultrasound transducer averaged 512 times (right).	21
Figure 3.13	Plot of simulated and experimental results of the lateral point spread function for Ultrasound imaging of the hair target with the single element transducer.	22
Figure 3.14	Plot of simulated and filtered experimental results of the lateral point spread function for Photoacoustic imaging of the hair target with the single element transducer.	22
Figure 3.15	Diagram of the beam width at various distances from the transducer face [3].	23
Figure 3.16	Raw PAT channel data of the 64-element phased array transducer with the 808 nm diode bar laser focused on a hair target in water.	27
Figure 3.17	A flowchart detailing the steps of processing the raw channel data into a beamformed image.	27
Figure 3.18	A diagram showing how the delays are applied to the channel data [2]. Where n is a given element of a transducer, d , is the element pitch ($38 \mu\text{m}$), x and y represent the coordinates of the focus, and h is the standoff distance.	29
Figure 3.19	Images of a hair target in water using a) ultrasound displayed with a dynamic range of -60 dB b) photoacoustic imaging with delay and sum beamforming applied and a -35 dB dynamic range plotted on a gray scale and c) photoacoustic imaging with coherence factor and delay and sum beamforming applied and a -35 dB dynamic range plotted on a gray scale	30
Figure 3.20	A plot of the lateral point spread function for both an image created using delay and sum (DAS) beamforming and an image created using delay and sum beamforming with a coherence factor applied (DAS+CF).	31
Figure 4.1	Reconstructed images of horse-hair phantom using 5 MHz transducer: PAT images acquired using a pulsed laser diode (PLD-PAT)(top) and a Nd:YAG laser with an optical parametric oscillator (OPO-PAT)(bottom) at 1cm depth. All images have the same scale bar. [30] © 2015 Optical Society of America.	32
Figure 4.2	The backscattering of ultrasound in a scattering medium.	34
Figure 4.3	Image of the scattering of light through a tissue phantom every 2mm in depth.	35

Figure 4.4	The scattering of light in a scattering medium.	36
Figure 4.5	The dependence of the ultrasound backscatter coefficient (BSC) with increasing silica concentration for phantoms G, H, I, J with silica concentration of 0.1, 0.5, 1.0, and 2.0% mass/volume respectively. Error bars were calculated from 2500 positions on 3 samples [5] © 2011 Optical Society of America.	37
Figure 4.6	Model of the staircase mold for mounting hair targets.	40
Figure 4.7	Model of the assembled staircase mold for mounting hair targets. . .	40
Figure 4.8	Pre-soaked hairs are epoxied to the staircase mould.	41
Figure 4.9	Top half of mould is attached as well as a glass slide using UV curing epoxy.	41
Figure 4.10	Phantom in the mold.	42
Figure 4.11	50 MHz Ultrasound image of the tissue phantom with only gelatin and intralipid. The red regions depict the areas used to calculate RMS amplitudes.	43
Figure 4.12	50 MHz Ultrasound image of a rat brain. The red regions depict the areas used to calculate RMS amplitudes.	44
Figure 4.13	50 MHz Ultrasound image of the tissue phantom with gelatin, intralipid, and 0.5% silica. The red regions depict the areas used to calculate RMS amplitudes.	45
Figure 4.14	50 MHz Ultrasound image of the tissue phantom with gelatin, intralipid, and 1% silica. The red regions depict the areas used to calculate RMS amplitudes.	45
Figure 4.15	50 MHz Ultrasound image of the tissue phantom with gelatin, intralipid, and 2% silica. The red regions depict the areas used to calculate RMS amplitudes.	46
Figure 4.16	A box plot representation of the RMS amplitudes of each region in the ultrasound images including the average of the RMS amplitudes for each sample.	46
Figure 4.17	Diagram of the scattering of photons in the sample medium and the resulting diffuse reflectance pattern.	48
Figure 4.18	Diagram of the diffuse reflectance experiment to determine the reduced scattering coefficient.	49

Figure 4.19	Results of the diffuse reflectance experiment to determine the reduced scattering coefficient of the phantom with intralipid and no silica. . .	50
Figure 4.20	Cross-section of the results of the diffuse reflectance experiment to determine the reduced scattering coefficient of the phantom with intralipid and no silica.	51
Figure 4.21	Results of the diffuse reflectance experiment to determine the reduced scattering coefficient of the phantom with intralipid and silica.	51
Figure 5.1	Fiber optic cable layers and light propagation via total internal reflection.	55
Figure 5.2	Photoacoustic fiber optic cables fixed to the ultrasound transducer plastic support using UV epoxy.	56
Figure 5.3	Illumination pattern at 12mm away from the endoscope tip.	57
Figure 5.4	A model of the ideal fiber bundle for coupling to the diode laser.	57
Figure 5.5	Image of the diode laser light in the near field.	59
Figure 5.6	Divergence of the laser in the horizontal direction (slow axis) at an angle of 6.04° and the divergence in the vertical direction (fast axis) at an angle of 0.83°	59
Figure 5.7	Diagram of the coupling optics for coupling the diode laser to the fiber bundle.	60
Figure 5.8	The laser image at the focus. The red circles overlayed on the image represent the fiber bundle fiber bundle cross-section.	61
Figure 5.9	Diagram of the system setup including the coupling system and laser.	61
Figure 5.10	Photoacoustic fiber optic cables temporarily fixed to the 40 MHz 2D phased array ultrasound transducer using wax.	67
Figure 5.11	Photoacoustic fiber optic cables temporarily fixed to the 30 MHz 3D phased array ultrasound transducer using wax.	68
Figure 5.12	Setup of the fabricated photoacoustic probe with a tissue phantom hair target and coupled fiber optics.. . . .	69
Figure 5.13	Ultrasound imaging results for hair targets in the tissue phantom using the 40 MHz 2D Endoscope. This image should ideally have 3 circular images from each of the hair targets located at the red markers.	70

Figure 5.14	Photoacoustic imaging results for hair targets in the tissue phantom using the 40 MHz 2D Endoscope. This image should ideally have 3 circular images from each of the hair targets which can be seen at the red markers.	70
Figure 5.15	3D Photoacoustic image of the hair target with the diode bar laser illuminating from the side.	71
Figure 5.16	3D Photoacoustic image of the hair target in tissue mimicking phantom using the final endoscope.	73
Figure 5.17	3D Photoacoustic image of the hair target in Intralipid and Gelatin phantom using the final endoscope.	73
Figure 5.18	Amplitude of channel 42 for the tissue phantom and the intralipid and gelatin phantom versus depth (mm).	74
Figure A.1	Reconstructed photoacoustic images(35 dB log gray scale dynamic range, 14 mm laterally by 40 mm axially) of a phantom with four point targets using (a) DAS, (b) DAS+MV, (c) DAS+CF, and (d) DAS+CF+MV [22].	83

Abstract

We present the results of a study to introduce photoacoustic tomography capability into a 2D endoscopic 64-element phased and 3D endoscopic 128-element crossed electrode ultrasound array for the use in endoscopic brain surgery. Our approach was to fix fiber optic cables to the ultrasound arrays, couple these fibers to a diode bar laser, and alter the ultrasound system firmware for both endoscopes. Through experiments performed on hair targets, we established requirements for transducer operating frequency, transducer dimensions, illumination intensity and illumination duration. We were able to integrate photoacoustic tomography into both endoscope systems and achieve images but the acquisition time was far too long to be surgically useful.

Acknowledgements

Special thanks to my advisor Dr. Rob Adamson for his help and patience when many stumbling blocks delayed this project, thanks to Chris Samson and Kate Latham for their help in integrating changes into the ultrasound system, and thanks to my family for their love and support.

Chapter 1

Introduction

Minimally-invasive surgical techniques have recently revolutionized the way in which brain surgery is performed [24]. In minimally-invasive surgery, surgery is performed through a small corridor and is sometimes guided by real-time video endoscopic imaging and pre-operative scans. To date, endoscopic imaging is performed primarily using cameras and conventional optical imaging but there may be surgical advantages to using ultrasound-based endoscopic probes and research is on the way to developing them [23]. A need for endoscopic ultrasound tools capable of functioning under tight spatial constraints while still providing adequate contrast has risen with the rise in popularity of these techniques. In previous work, our group has demonstrated the use of an endoscopic 64-element phased ultrasound array that operates with a center frequency of 40 MHz [1]. To date, this ultrasound array is capable of imaging soft tissue in the brain up to 10mm in depth, distinguishes between white and gray matter, and is capable of imaging vasculature using ultrafast Doppler imaging [1, 27]. Doppler imaging allows an overlay to be applied which increases contrast between fast moving blood and the surrounding tissue. However, doppler imaging is blood-velocity dependent, making it challenging to detect slow-moving blood which would be found in veins and microvasculature. Since photoacoustic tomography is independent of blood flow velocity, photoacoustic tomography could help form a more complete vascular map of the brain such as in the examples of photoacoustic images of rodent brains that can be seen in figure 1.1 below. Additionally, photoacoustic tomography can assess oxygenation level by using the absorption difference between oxygenated hemoglobin and deoxygenated hemoglobin which can also be seen in figure 1.1. With real-time mapping of blood optical absorption we would be able to implement functional imaging in the operating room as is currently done with neurophysiological monitoring using awake cortical mapping [12]. Doppler imaging is capable of measuring blood flow but the contrast mechanism is blood velocity rather than blood volume, making it challenging to detect venous flow and microvasculature. With

photoacoustic tomography (PAT), this functional imaging is constructed from the blood-oxygen level-dependent (BOLD) signal. This imaging modality would use the difference between two PAT signals from lasers with different wavelengths to map the location of oxygenated and deoxygenated blood in the brain. This map of oxygenation could be used to guide surgeons so that key functional areas of the brain (areas that metabolize oxygen) are avoided and patient safety is maximized in the operating room.

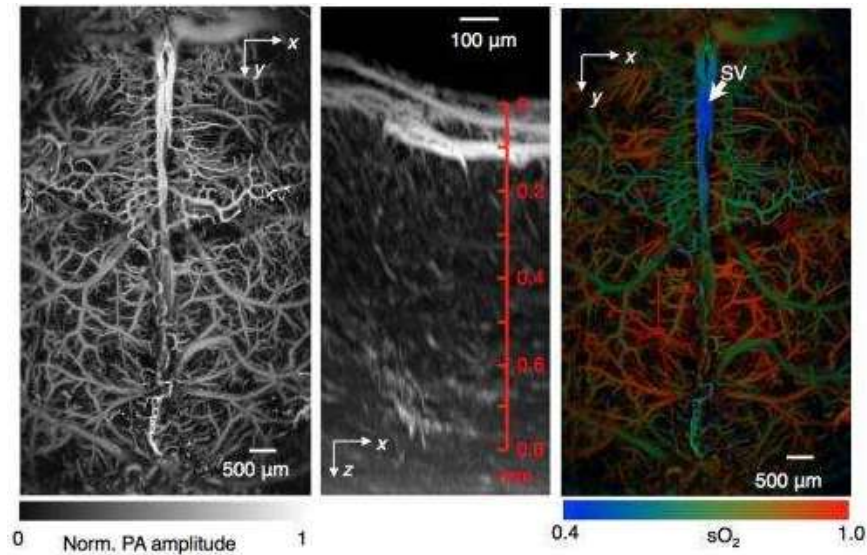


Figure 1.1: An image of fast functional photoacoustic microscopy of the mouse brain from an experiment by Yao, Wang, et. al. [37]. The left shows a representative x-y projected brain vasculature image through in intact skull. The middle shows the x-z projected brain vasculature image. Finally, the right image shows photoacoustic microscopy of oxygen saturation (sO_2) of hemoglobin in the mouse brain. Where red vessels have a high oxygen (arteries) saturation and blue/green regions have low oxygen saturation (veins). SV = skull vessel.

We can achieve this functionality in surgery by adding photoacoustic tomography to intrasurgical ultrasound endoscopes. PAT is an imaging modality that uses generated light and ultrasound to produce an image. PAT works by illuminating a sample medium which absorbs some of the incident photons. In the brain the main optical absorber is blood. The absorption of incident photons by the blood induces a rise in temperature as energy is transformed into heat and this increase in temperature creates a thermal expansion resulting in the formation of an acoustic pressure wave that then propagates through the medium [40, 35]. We intend to construct a photoacoustic phased array by directing laser light to the endoscope tip using fiber optics to generate and measure these pressure waves and use it to

form an image of vasculature that can be overlaid on B-mode ultrasound images.

1.1 Potential Clinical Applications of Endoscopic PAT

A specific example of a clinical application for this endoscopic photoacoustic tomography probe is for the neurosurgical removal of cavernous angioma also known as cerebral cavernous malformations (CCM): a vascular malformation formed by a collection of abnormally dilated blood vessels [29, 25]. These growths can range in size from less than a few millimeters to several centimeters and are characterized by “caverns” of blood-filled vasculature where blood flows very slowly. These structures are highly vascularized and would therefore create strong targets for a photoacoustic imaging system but the slow moving nature of the blood in this vasculature may not be measurable using ultrafast doppler imaging. This, combined with CCMs having undefined borders and dynamic structures that change in size and shape over time, PAT could prove useful in giving surgeons a more accurate representation of these lesions during surgical procedures in combination with pre-operative scans. CCMs are present in around 0.5% of the population and account for 8-15% of all brain and spinal vascular malformations [29].

While the structure of CCMs is ideal for PAT given their vascularization, this system could perhaps be more clinically useful in imaging highly vascularized tumors such as recurrent glioblastoma multiforme (GBM) which cause more serious harm to patients. These tumors, which grow from glial cells (astrocytes and oligodendrocytes), account for approximately 17% of brain tumors and are characterized by a vascularized surface with a necrotic core [41]. Since the tumors recruit blood vessels to aid in rapid growth, vascular images using PAT could help surgeons resect the tumor with better margins, leaving more healthy tissue around the excised lesion. Since GBMs are a highly aggressive form of cancer and patient prognosis depends greatly on the surgeons excision of the tumor, ensuring our system is useful in imaging these structures could affect the lives of many patients if implemented clinically.

Other possible applications of a PAT endoscope for use in brain surgery include minimally invasive in vivo imaging of epileptic seizures, imaging of vascularized glioblastoma tumors, measuring of the metabolic rate of oxygen and glucose, and early-stage theranostics [42, 39, 19]. Additionally, use of contrast agents such as gold nanoparticles, fluorescent proteins, and

organic dyes could be used in combination to increase image contrast [39].

1.2 The Photoacoustic Effect

The photoacoustic effect is a process by which energy from photons is converted into acoustic pressure through absorption and thermal expansion and is the process that makes photoacoustic imaging possible. The local pressure rise p_0 that is found immediately after the light pulse is absorbed by a sample medium is given by equation 1.1 [32].

$$p_0 = \Gamma \eta_{th} \mu_a F \quad (1.1)$$

Where η_{th} is the percentage of incident power converted to heat, μ_a is the absorption coefficient of the medium, F is the fluence, and Γ is known as the Grueneisen Parameter given by:

$$\Gamma = \frac{\beta v_s^2}{C_P} \quad (1.2)$$

where β is the thermal coefficient of volume expansion, v_s is the speed of sound in the sample medium, and C_P is the Specific heat capacity at constant pressure. The Grueneisen Parameter of human blood is 0.16 [36].

Using these equations and the wave equation for ultrasound, a derivation of a formula for the pressure at a particular time resulting from the pulse excitation of a cylindrical absorber is given by the following equation [15]:

$$p_f(\hat{t}) = \frac{ip_0}{2\pi} \int_{-\infty}^{\infty} \frac{J_1(\hat{q}) H_0^{(1)}(\hat{c}\hat{q}\hat{r}) e^{-i\hat{q}\hat{t}}}{\hat{q} [J_1(\hat{q}) H_0^{(1)}(\hat{c}\hat{q}) - \hat{\rho}\hat{c} J_0(\hat{q}) H_1^{(1)}(\hat{c}\hat{q})]} d\hat{q} \quad (1.3)$$

Where J_0 is the zeroth-order Bessel function, J_1 is the first-order Bessel function, and $H_0^{(1)}$ is the zeroth-order Hankel function. With $\hat{t} = v_s t/a$, $\hat{c} = v_s/c_f$, $\hat{r} = r/a$, $\hat{\rho} = \rho_c/\rho_f$, and a is the radial coordinate, c_f is the speed of sound in water, ρ_c is the density of the target, and ρ_f is the density of water. \hat{q} is a dimensionless frequency where $\hat{q} = \omega a/v_s$.

The derivation of this equation involves finding a solution, p , to the wave equation, solving for the pressure in the surrounding medium, p_f , and taking the Fourier transformation. The resulting pressure profile depends on the light source incident on the sample medium and the properties of the sample medium being imaged including its geometric shape. An example of

a photoacoustic signal from a cylindrical source with an incident delta function illuminating light source can be seen in figure 1.2 below.

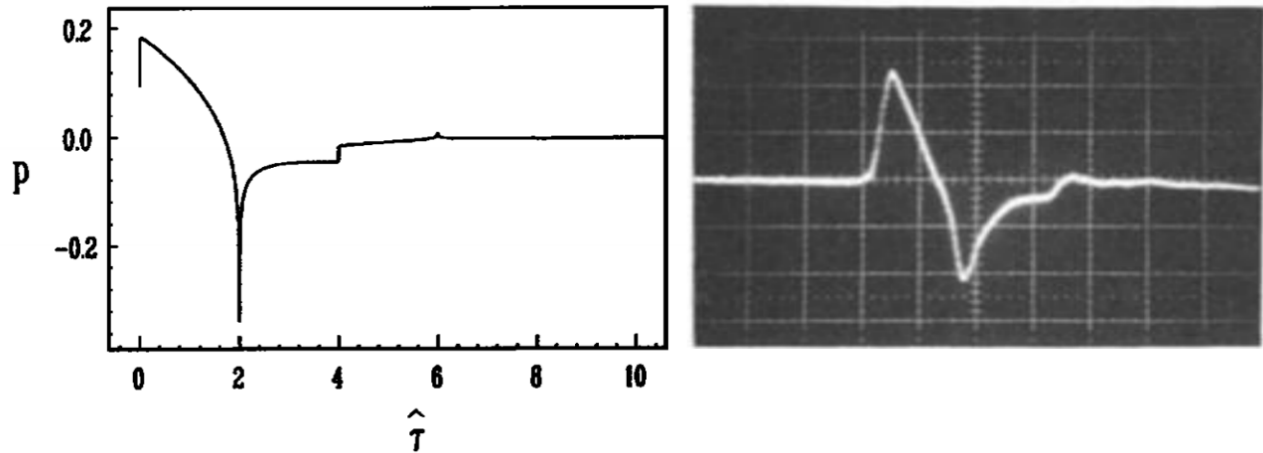


Figure 1.2: Example of a simulated (left) and experimental (right) pressure plot from a cylindrical photoacoustic target [15]. Where p is the pressure and $\hat{\tau}$ is the dimensionless retarded time.

1.3 Diode Laser as Pulsed Light Source

Most photoacoustic systems require use of a short pulsed light source to excite thermal expansion and create an impulsive pressure wave. In the vast majority of PAT systems, neodymium-doped yttrium aluminum garnet (Nd:YAG) lasers in combination with optical parametric oscillators (OPO) or dye lasers are used as the illuminating source but these lasers are expensive, bulky, and have a low repetition rate making them a poor choice for high-speed imaging [30]. It is also often the case that these lasers require the use of a vibrational isolation table making them even more impractical for clinical use. In recent experiments, PAT has been performed using diode lasers which are considerably less expensive (can be up to 5 times less than Nd:YAG/OPO), are smaller, and are capable of higher repetition rates but at lower energy per pulse [30, 7]. A study comparing the imaging of a horse-hair phantom using a pulsed diode laser and a Nd:YAG/OPO laser showed that averaging low energy pulses at a high repetition rate from the diode laser gave better signal-to-noise ratio (SNR) than a smaller number of high energy pulses from the Nd:YAG/OPO laser [30].

In this project, we chose a laser with a wavelength in the “tissue window” for imaging tissue [11]. This window is determined by the optical absorption of various biological substances in skin which shows that the optimal wavelength range to achieve maximum penetration in tissue is between 800 nm and 1000 nm which is mainly determined by the absorption by water [11]. We use an 808nm diode bar laser (QD-Q1R05-ILO MM24007 Quantel Laser Diodes, France) with $500\mu\text{J}$ of pulse energy, 28-53 ns pulse width (FWHM), and a 1kHz repetition rate which is comparable to diode laser experiments previously performed [30, 7]. All of our experiments were performed with the pulse width set to 28 ns. This laser is also very small and portable measuring approximately 60mm by 40mm by 22mm. Having a small laser will be important when it comes to incorporating the PAT system into the casing of the pre-existing ultrasound setup. The diode laser was also inexpensive at a price of \$15,000 compared to more traditional Nd:YAG/OPO laser which cost \$80-100k and so overall we believe this laser to be more clinically practical for photoacoustic tomography in tissue such as brain.

While this 808 nm wavelength is good for imaging blood since both oxygenated hemoglobin (HbO_2) and deoxygenated hemoglobin (HbR) are good absorbers at 808 nm (figure 3.4), the signals from both of these hemoglobin molecules would be identical since their absorption is essentially the same. This means in order to perform BOLD functional imaging we would require a second laser with a wavelength between 600-800 nm where their absorption coefficients are further apart. In taking the difference in PAT signal produced by each laser we could then map the functional regions of the brain due to the metabolism of oxygen in these regions. We could also use fast doppler imaging to perform this functional imaging using blood velocity, however, photoacoustic tomography would provide increased contrast in microvasculature where blood moves very slowly.

The chosen diode laser has a laser diode bar which is a one-dimensional array of broad-area emitters. Our laser consists of 5 rows of one-dimensional arrays with 20 emitters each which can be seen in figure 1.4. A property of diode bars are the rectangular image created which has a “fast axis” direction which corresponds to the vertical direction, and a “slow axis direction corresponding to the horizontal direction. These are named because typically the “fast axis” is fast diverging and the “slow axis” is slowly diverging. However, the manufacturer has included a collimating cylindrical lens in the fast axis which reduces the divergence to 0.83° leaving the slow axis to diverge faster at 6.04° .

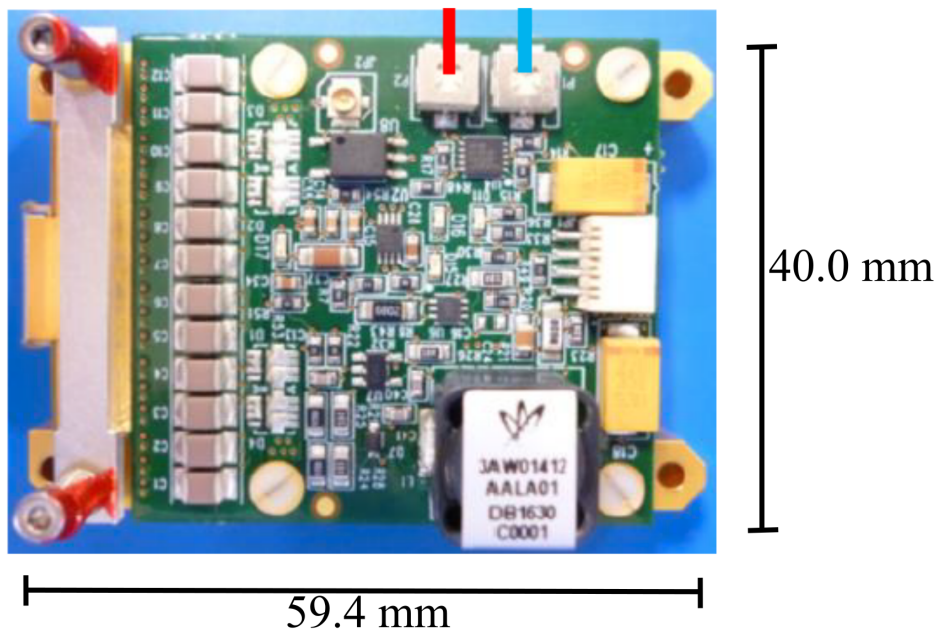


Figure 1.3: An image of the 808nm diode laser used in this project.

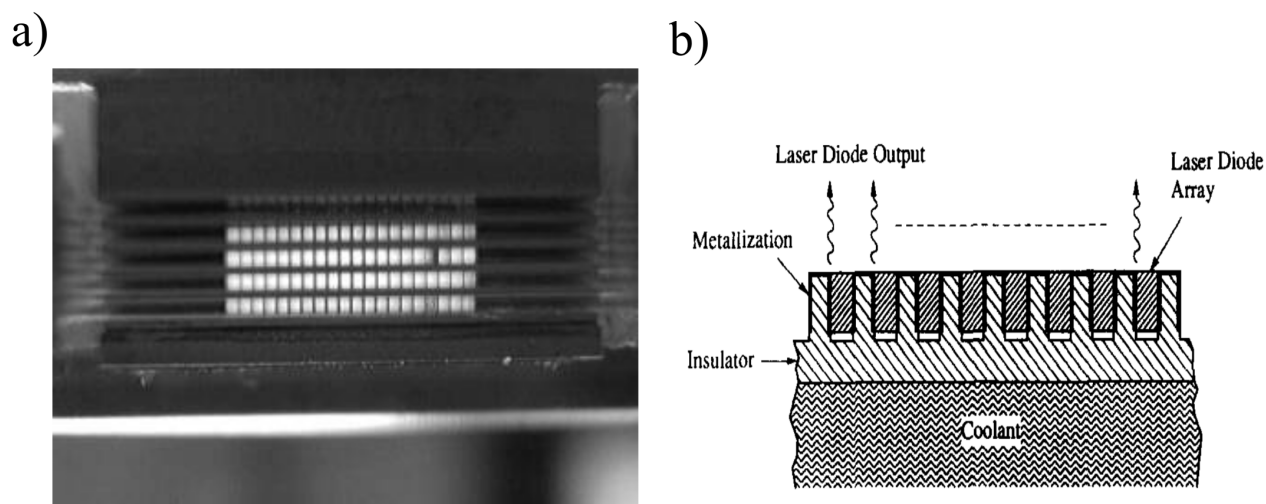


Figure 1.4: a) The diodes bars of our laser that make up the total laser output. b) An example of a diode bar [8] © 1992 IEEE.

The difference in divergence results in two different virtual point sources for the fast and slow axes which results in an astigmatism in the wavefronts at the output and so upon focusing would lead to different focal locations. We needed to correct for this astigmatism before coupling our laser to the fiber optics we attached to the endoscopes so that the wavefronts couple to the fiber bundle efficiently.

Chapter 2

Thesis Objectives

This project aims to introduce photoacoustic tomography into two already existing endoscopic ultrasound probes, a 2D 64-element phased ultrasound array and a 3D 64 x 64-element crossed electrode ultrasound array, using a diode laser as the pulsed light source. We proceed by establishing requirements for optical fluence, transducer operating frequency, device aperture, penetration depth, and contrast. We then present a novel design meeting those requirements in which laser light is delivered through a set of optical fibers via a coupling system designed to minimize the amount of light lost and thus maximizing the fluence reaching the tip of the endoscope. The performance of the device will then be verified by imaging hair targets in water and in custom tissue mimicking phantoms.

Our approach begins with performing preliminary single element transducer experiments on a hair target in water with focused laser light to determine the SNR and resolution required for the intended imaging. We would then use the 2D 64-element phased ultrasound array to image the hair target and make any necessary adjustments to software to include averaging and to the firmware to adjust for any delay changes in the system. Measurements would be taken of the SNR, which is influenced by the fluence and repetition rate, and resolution and bandwidth, which are determined by the ultrasound transducer. A tissue mimicking phantom would then be designed and fabricated in order to verify requirements have been met to image in tissue. An illumination source would then be designed as well as a coupling system to couple to the fiber optics. The coupling efficiency of the design will affect the amount of light that ultimately reaches the photoacoustic target which will affect the amplitude of the resulting pressure produced thus affecting the overall SNR. The fiber optic cable bundle and endoscope tip fiber configuration would be designed and fabricated, attaching fibers to each of the two endoscopes. Images of the tissue phantom would then be taken using the 2D photoacoustic endoscope with fiber optic illumination and these images would be assessed to see if they meet the design requirements established. The experiments and fabrication steps would then be repeated with the 3D 128-element crossed electrode

ultrasound array and resulting images would be also be assessed to see if they meet the design requirements.

Whether or not the endoscopes meet the design requirements will determine their usefulness as a surgical tool. Ultimately, if the images produced by these endoscopes do not provide adequate contrast between the background noise and the photoacoustic signal they will not provide surgical information and this would be affected by optical fluence and the amount of averaging we need to do to create this level of contrast. Since in photoacoustic imaging, we only receive signal from optically absorbing parts of the target there should be improved contrast in photoacoustic images. Therefore, we aim to achieve at minimum a higher contrast than we see in ultrasound images using the same ultrasound system. The current ultrasound system gives a contrast of 22 dB with a target of hair in a water bath and so we aim to achieve a contrast higher than this value in tissue-mimicking phantom. If the transducer operating frequency is too low then images will not be created quickly enough for the surgeon to use this information in the operating room. We aim to show that PAT images could be taken with this system at a frame rate of 1 FPS. Since this is meant to integrate into an already existing system we also need to make sure the penetration depth matches the ultrasound imaging window otherwise data will be lost at greater depth which means we need to image at least 10 mm in depth. Finally, this device is endoscopic and so we aim to keep the device aperture similar to the current ultrasound endoscope aperture which has the dimensions 2.5 x 3.1 mm [1].

Chapter 3

Proof of Principle and Beamforming

In order to begin to integrate photoacoustic capabilities into the ultrasound endoscope, we wanted to first demonstrate that we could obtain a photoacoustic signal using the diode laser and phased array ultrasound transducer. We also wanted to use a simple, controlled case to measure the lateral and axial resolution of the photoacoustic signal when our laser and ultrasound transducer are used in combination.

In order to measure a photoacoustic image and determine these resolution values, an experiment was devised whereby a line target made of human hair, which is a good optical absorber due to its melanin content, would be illuminated by our pulsed light source, an 808nm diode laser with $500\mu\text{J}$ of pulse energy, and the resultant pressure waves would be collected by the pre-existing 64-element phased array. In this setup we would illuminate the target from the side and collect the image from the top using the ultrasound probe which can be seen in figures 3.2 and 3.3. This setup allows us to achieve a photoacoustic image using the pre-existing ultrasound system prior to having to deal with first integrating the light source into the endoscopic form factor, and also allowing us to work out the changes in beamforming that need to take place with a simple case.

The ultrasound system includes three main parts, the motherboard, daughter cards, and transmit/receive boards which can be seen in figure 3.1 [28]. The eight daughter cards relay the information between the motherboard and the transmit/receive boards and the motherboard then sends the collected data to a computer which runs the software to control the rest of the system. There are two versions of the software that run this system. One beamforms the data in real time and displays the sector scan of the ultrasound image and the other collects and displays the raw data from a single channel. Since the channel data program takes the data from each of the 64 elements over time, the software allows us to implement averaging and do our own beamforming in post we decided to make changes to this version of the software. There are two main probes being used with the system: a 40 MHz 64-element phased ultrasound array used for 2D imaging, and a 30 MHz 128-element

crossed electrode ultrasound array used for 3D imaging. We used both of these probes to implement photoacoustic tomography to the system. Other applications being studied with this system include implementing histotripsy which uses focused ultrasound to ablate tissue, doppler imaging which uses the doppler effect to detect movement including that of blood, and ultrafast ultrasound which would aim to make the system faster.

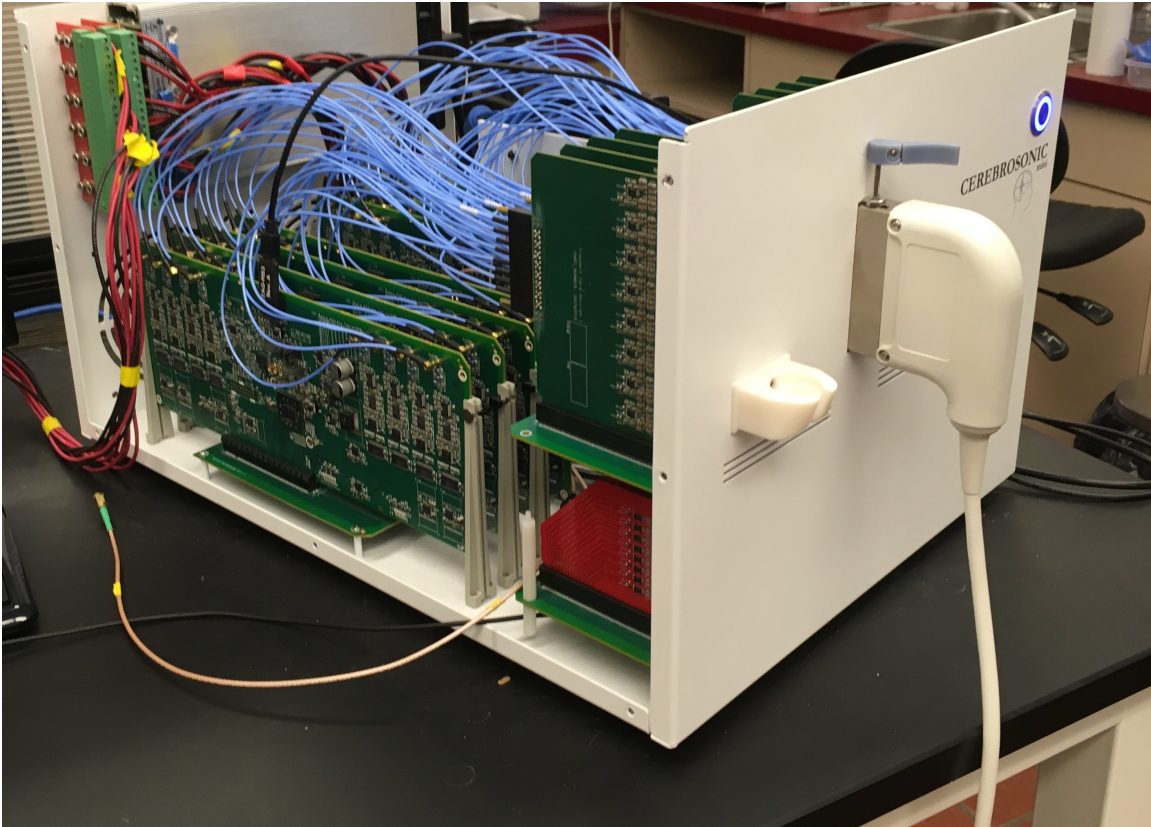


Figure 3.1: The ultrasound system inner electronics.

In order to execute this experiment, it was necessary to complete the following development work. First, we needed to use optics to focus our laser light and maximize the photoacoustic signal we hope to measure. We then used a simplified version of this experiment with a single element transducer to get a preliminary photoacoustic signal and establish the lateral and axial resolution before we moved on to the 64-element transducer. Changes then needed to be made to the ultrasound systems host software so that we can collect images from the pre-existing firmware. Finally, a beamforming algorithm was developed to process the data into a final image.

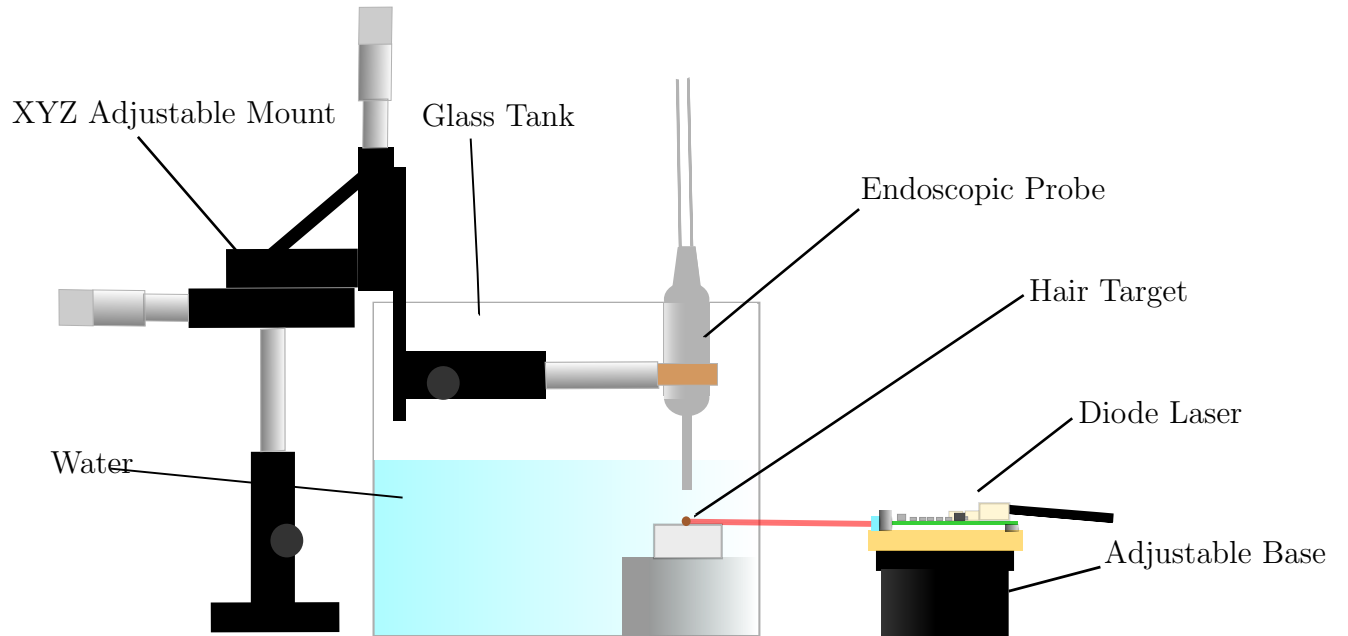


Figure 3.2: A diagram of the experimental setup.

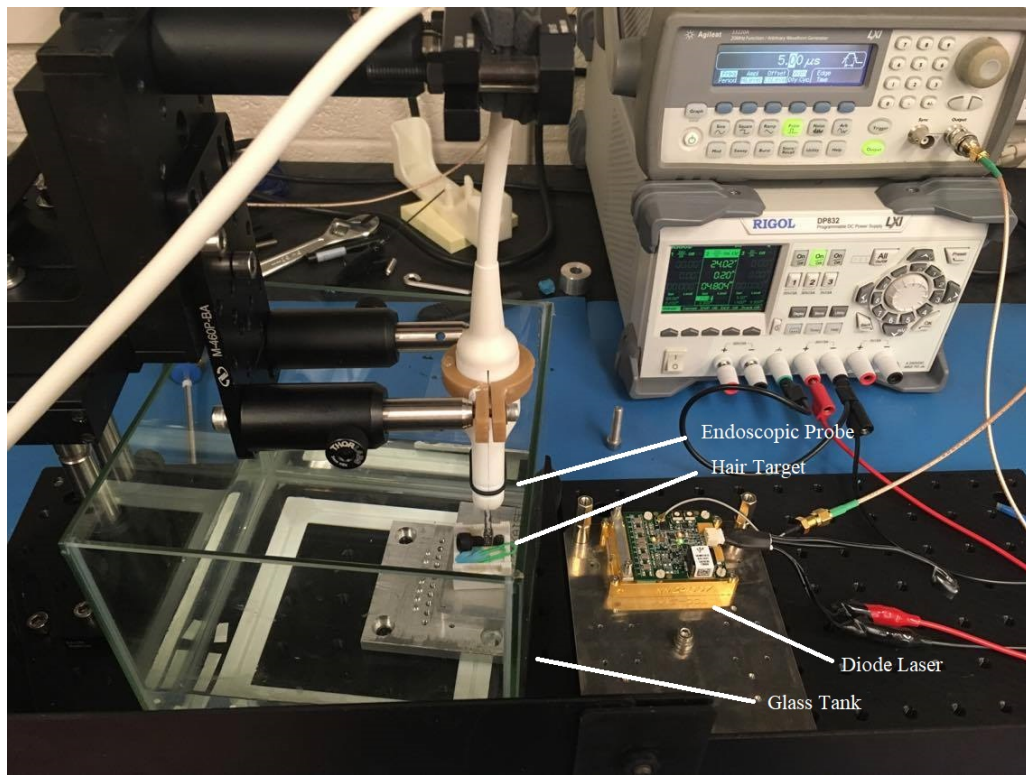


Figure 3.3: A picture of the experimental setup.

3.1 Selecting a Phantom Imaging Target

The properties of the material chosen will affect the amplitude of the photoacoustic pressure wave as in equation 1.1. We therefore use a target material with a high absorption coefficient compared to that of blood since this will be the significant factor in changing the initial pressure at the target in equation 1.1. If we look at the absorption spectra of various substances in the human body in figure 3.4, we can see that oxygenated hemoglobin, HbO_2 , and deoxygenated hemoglobin, HbR , have an absorption coefficient at least an order of magnitude higher than all of the other substances we find in tissue apart from melanin. Since melanin is not commonly found in tissue other than skin and hair, blood is the significant absorber compared to the surrounding tissue in our target tissue in the brain.

While blood would be the ideal target material to use to test our system, since it is the goal to image vasculature, there are significant challenges to working with it. Blood is difficult to obtain because it would either need to be drawn or obtained in an ethical manner, it would need to be properly stored and handled, and quickly coagulates. Blood also creates a challenge in creating a small enough line target due to the fact that most tubes used to contain it would be larger than the resolution of the ultrasound system. We therefore decided to use a comparable substitute that would be much easier to work with and considering everything above, the material chosen for imaging in this experiment was human hair which contains melanin since we know this will have a significant amount of absorption. At $\lambda = 808 \text{ nm}$ melanin has $\mu_a \approx 100 \text{ cm}^{-1}$ compared to 10 cm^{-1} for blood [38]. Other researchers have used hair targets as well due to the fact that it is readily available, has a large optical absorption due to its melanin content and is much more convenient to work with than blood [4, 38].

3.2 Focusing Optics

The material properties of the photoacoustic target are not the only factors that will affect the amplitude of the photoacoustic signal. According to equation 1.1, the fluence, which is the optical energy per unit area, incident on the photoacoustic target is another important contributor to a high amplitude signal. We therefore wish to maximize the fluence on our hair target and in order to do this we need to focus the laser light.

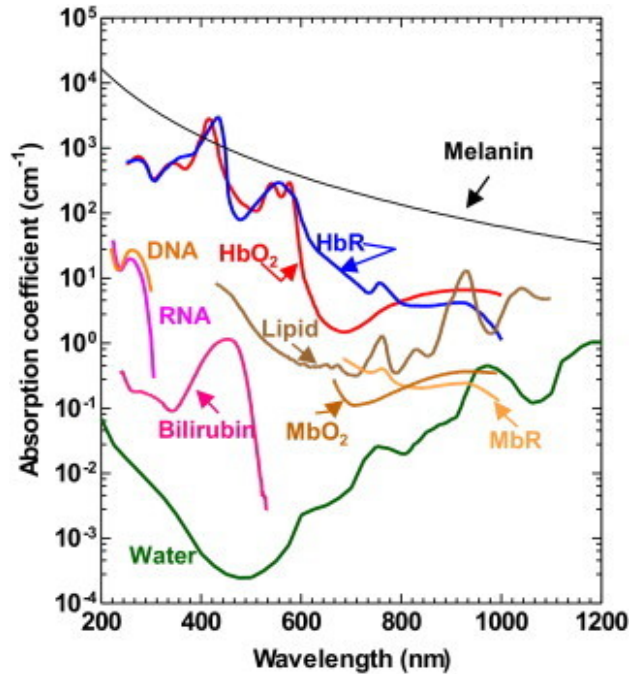


Figure 3.4: The absorption spectra of major absorbing substances in tissue [38].

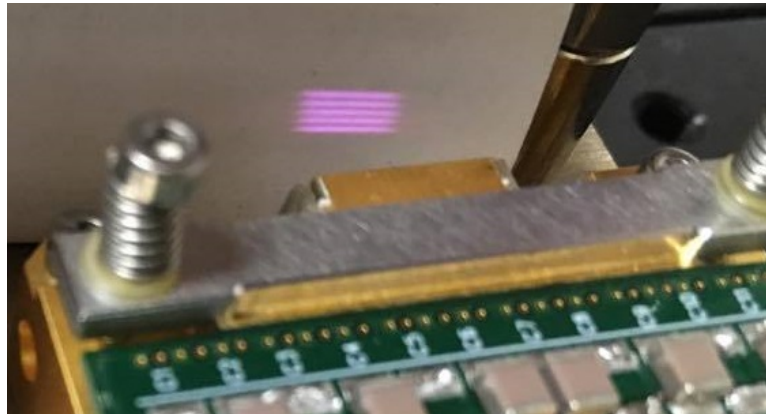


Figure 3.5: An image of the output of the laser in the near field.

The diode bar laser consists of rows of diodes whose added optical output create the laser image. This results in the diode laser having a rectangular image, which can be seen in figure 3.5, where the near field image at the output of the laser is 5 mm in the slow axis (horizontal) and 2.3 mm in the fast axis (vertical). A diagram of the diode face can be seen in figure 3.6. The beam was measured to diverge by 6.04° in the slow axis and 0.83° in the fast axis. This means that when we have the laser as close to the hair as possible while still leaving room for the endoscope to fit above the hair in the water tank (~ 4 cm) the beam is

13.5 mm by 3.46 mm.

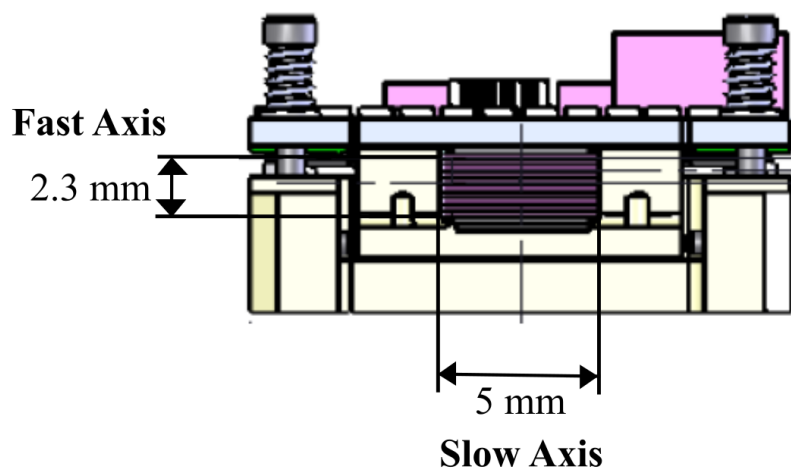


Figure 3.6: A diagram of the front face of the laser diode.

We can also see in figure 3.5 that there are gaps in this laser image due to the gaps between the diode bars in the laser. These gaps mean that this area at 4 cm is not entirely illuminated and if not properly aligned, the hair could be sitting in one of these dark zones with little to no light illuminating it. This is more of an issue at the focus of the laser due to the fact that as the light becomes unfocused this image becomes more uniform. Since the hair is only $40\ \mu\text{m}$ in diameter all of this means that most if not all of our light is not hitting the target. We can drastically increase the amount of light hitting the hair target by focusing the light from the diode laser into a small spot which will also decrease the likelihood that the hair is sitting in a dead zone. The hair is aligned with the laser by placing a white surface behind the hair and manually aligning it by eye. With the light focused it is easier to manually align the hair because the spot is brighter and easier to see.

The focusing optics used to do this can be seen in figure 3.7. A 40 mm cylindrical lens (Thorlabs LJ1125L-B Plano-Convex Cylindrical Lens, Antireflection Coating: 650-1050 nm) corrects the astigmatism by moving the focus in the horizontal direction to the same spot as the focus in the vertical direction which also reduces the 6° divergence in the horizontal direction. Next, a 35 mm spherical lens (Thorlabs AC254-035-C-ML Achromatic Doublet Antireflection Coating: 1050-1700 nm) was used to focus this new image down to an image size of 2 mm by 0.5 mm in air. The unfocused image has an area of $4.67 \times 10^{-5}\ \text{m}^2$ and the focused image has an area of $1.0 \times 10^{-6}\ \text{m}^2$, which gives an increase in fluence from focused

to unfocused of 46.7 times.

This lensing system is designed to maximize the fluence of light on the hair in this case and is only illuminating a fraction of the total ultrasound volume. While this maximizes the photoacoustic signal for preliminary testing, when we move to integrating the fiber optic cables into the final endoscope we will need to illuminate the entire volume within the ultrasound probe's field of view and so will have a reduction in the fluence and thus the photoacoustic signal strength.

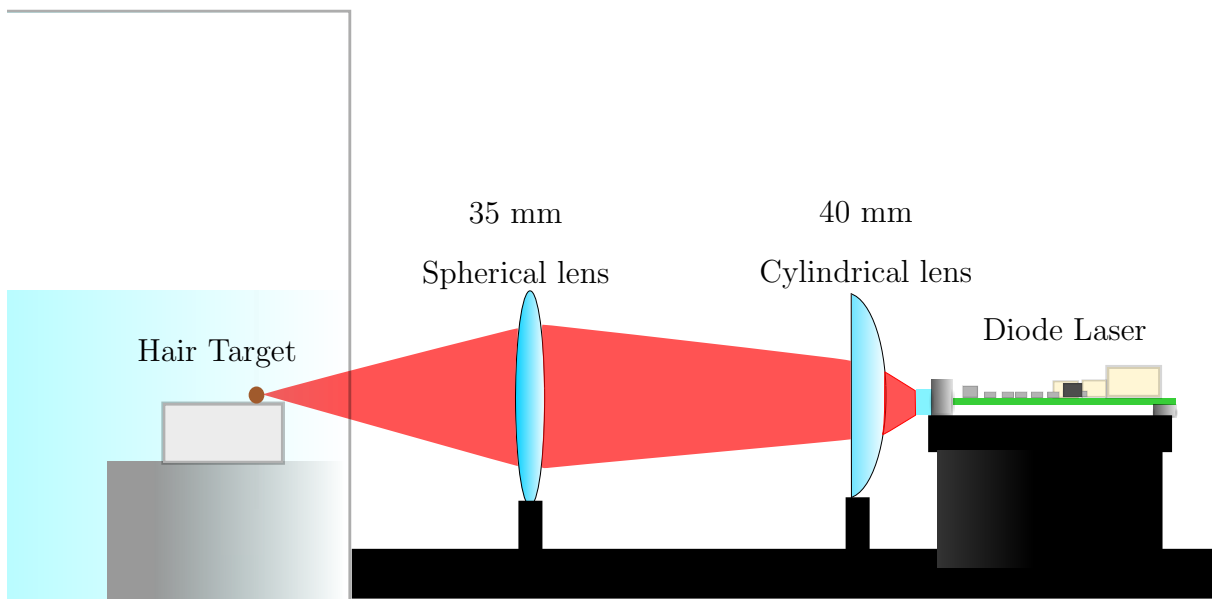


Figure 3.7: A diagram of the focusing system.

3.3 The Photoacoustic Signal from a Cylindrical Source

In order to calculate the photoacoustic signal we expect from a cylindrical hair target and a gaussian light pulse with a full-width half-max (FWHM) of 28 ns, we first find the impulse response of the hair with a delta pulse using equation 1.3. To calculate we convert the normalized values in 1.3 to physical values that model the experimental conditions using a distance from transducer to hair of $r = 6$ mm, a speed of sound in water of $c_f = 1480$ m/s, a speed of sound in hair of $v_s = 2500$ m/s [26], a radius of hair of $a = 20$ μm , and a density

of hair of $\rho_c = 800 \text{ kg/m}^3$. The resulting simulated impulse response can be seen in figure 3.8 below.

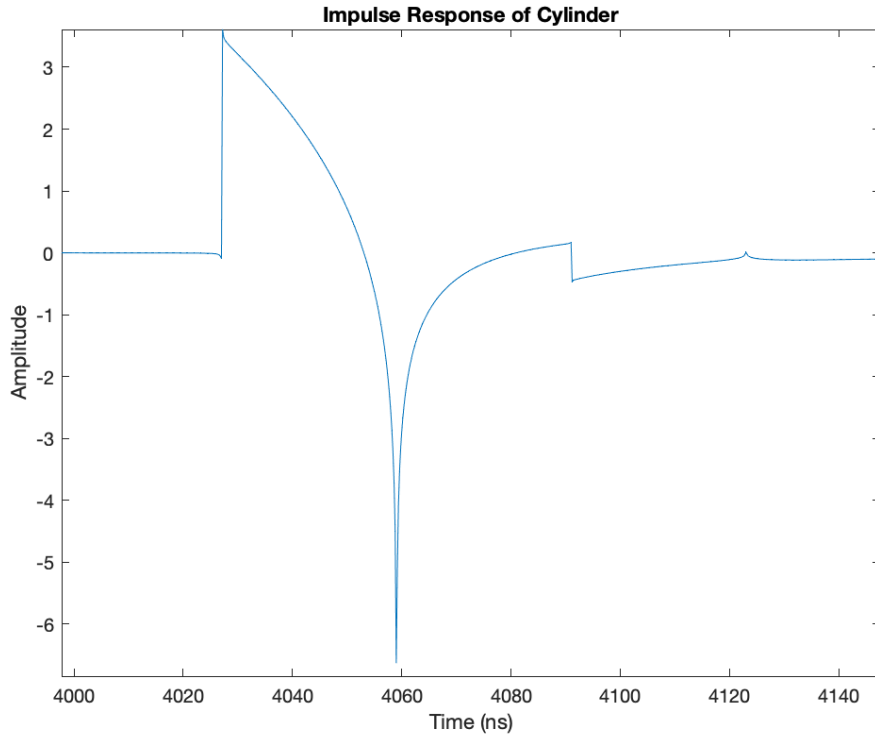


Figure 3.8: Simulated impulse response of a hair target with a delta function pulse.

The simulated impulse response was then convolved with the gaussian intensity profile of the laser pulse given by the following function where $\sigma \approx \text{FWHM}/2.3548 = 28 \text{ ns}/2.3548$ as specified by the manufacturer [34].

$$f(t) = \frac{1}{\sigma\sqrt{2\pi}} e^{-(t)^2/(2\sigma^2)} \quad (3.1)$$

This convolution gives the resulting photoacoustic signal in figure 3.9. Performing frequency analysis on this photoacoustic signal gives the frequency spectrum in figure 3.10 with a center frequency of 7 MHz.

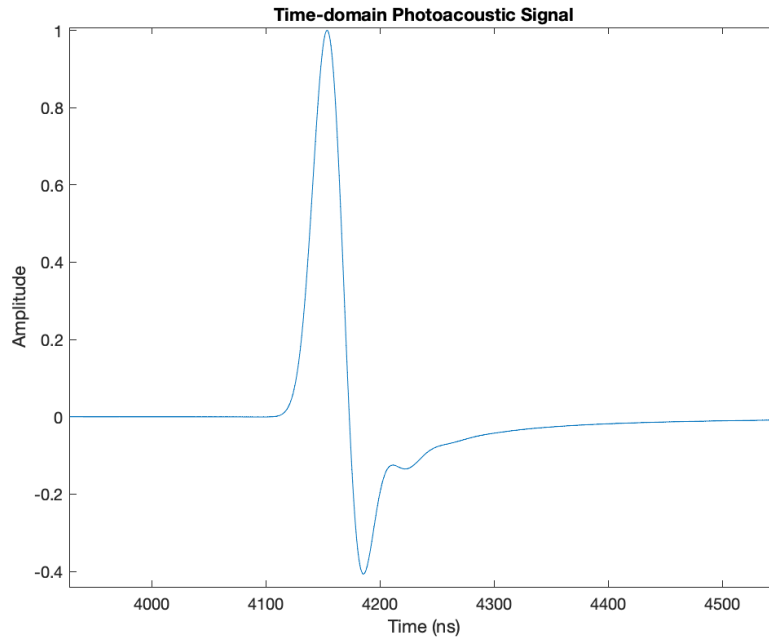


Figure 3.9: Simulated photoacoustic signal resulting from the convolution of the gaussian pulse and the photoacoustic signal from a delta function excitation.

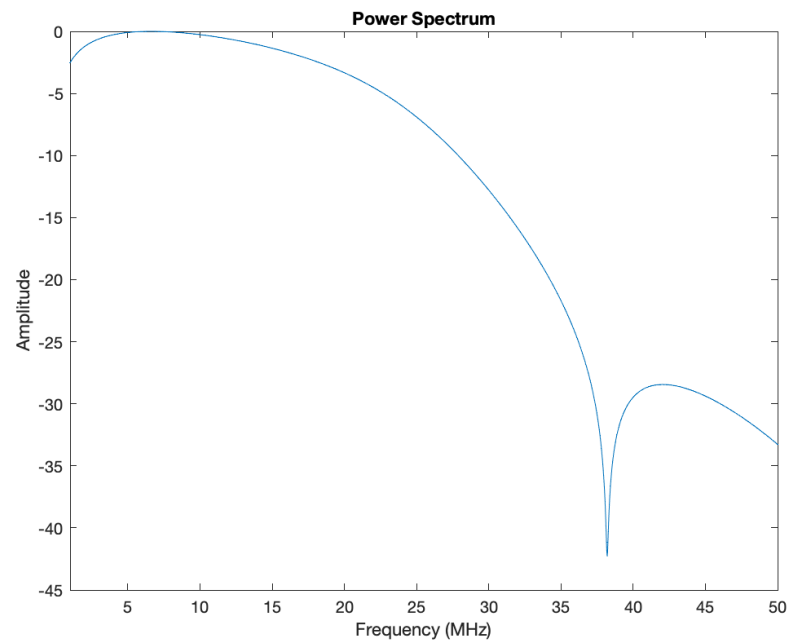


Figure 3.10: Simulated frequency spectrum of the photoacoustic signal resulting from the convolution of the gaussian pulse and the photoacoustic signal from a delta function.

These simulations indicate that the photoacoustic signal from the hair target peaks at a frequency of 7 MHz, significantly lower than the center frequency of the transducers used in this thesis. However, the simulations also indicate that the bandwidth of the photoacoustic signal is quite wide (310% fractional 6 dB bandwidth) so that the photoacoustic signal strength is only 9 dB lower than its peak value at 22 MHz (the center frequency of the transducer used in Chapter 3) and 26 dB lower at 30 MHz (the center frequency of the transducer used in Chapter 5). The low peak frequency of the PA signal is due primarily to the 28 ns pulse width of the laser. The center frequency of the photoacoustic emission spectrum would be increased to 22 MHz if the pulse width could be reduced to 8.2 ns and to 30 MHz if the pulse width could be reduced to 6 ns. Unfortunately, reductions in the laser pulse width could only be achieved through a redesign of the bar laser and/or laser drive electronics which was outside the scope of this work. The peak photoacoustic emission frequency is also weakly dependent on the hair target diameter and could be increased if a lower diameter target were used.

While not optimal, the PA center frequency predicted from these simulations remains suitable for verifying the concept of a photoacoustic endoscope using a 30 MHz center frequency array. Based on this simulation, if, in future, the laser pulse width can be reduced to an optimal duration while maintaining laser fluence, photoacoustic signal strength for a 30 MHz array could be increased by a 26 dB relative to the signal amplitude reported in this thesis.

3.4 Single Element Transducer Experiment and Results

Instead of starting by imaging this hair target with the 64-element phased array transducer, we decided to first use a single-element transducer in an attempt to see if we could achieve a photoacoustic image at all and use this much simpler case to trouble shoot the issues we might have with alignment and focusing of the laser light on the target.

Several single element transducers were tested in order to find the best available transducer to use to test our photoacoustic signal. We selected an 8-element annular array transducer (DS-001: Annular Array 28MHZ-8EL, Daxonics Ultrasound, NS) with a center element which is a 22 MHz unfocused single element transducer with a radius of 0.62 mm which is indicated in figure 3.11. We decided to use only the center element because it is an unfocused array with a lower center frequency compared to the other transducers and this lower center

frequency was closest to the center frequency of the photoacoustic signal.

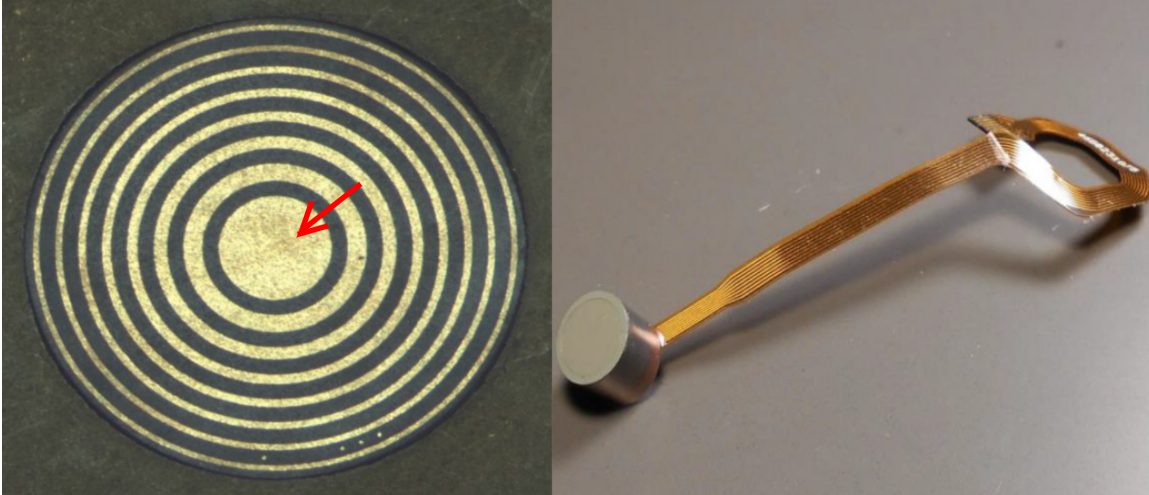


Figure 3.11: The 22 MHz 8-element annular array with the element we used indicated (left) and the full annular array transducer assembled (right).

We used a high-frequency pulser/receiver (10ERS5 Daxonics Ultrasound, NS) with the transmit pulse on the receiver shut off by disconnecting the trigger signal for transmit. The laser then illuminated the hair so that the photoacoustic signal in figure 3.12 was measured. However, in order to clearly see the photoacoustic signal we needed to average this data over 512 frames which can be seen in figure 3.12. This averaged signal has a peak voltage of approximately 3.3 mV and an RMS noise floor of 0.42 mV giving a signal-to-noise ratio (SNR) of 7.8. Without averaging, the SNR of this signal is 0.35 which tells us that averaging of the photoacoustic signal of this magnitude will be required in order to achieve a reasonable SNR. The SNR of the averaged signal of 7.8 was consistent with the dependence on SNR of $1/\sqrt{N}$ where N is the number of averages.

In order to measure the lateral resolution of both the ultrasound and photoacoustic signal, the transducer was moved across the hair in increments of 0.02 mm and both signals were measured at each location. The peak signal was then calculated in each case and plotted versus the position with respect to the center of the hair which can be seen in figures 3.13 and 3.14 along with simulated data. These plots are called the lateral point spread function (PSF) and shows the cross-sectional image of a point target measured by the ultrasound transducer. It is a common practice in imaging to measure the full width at half maximum of these distributions to give the lateral resolution of both ultrasound and photoacoustic images. The lateral resolution represents the width of a point target in an image created by

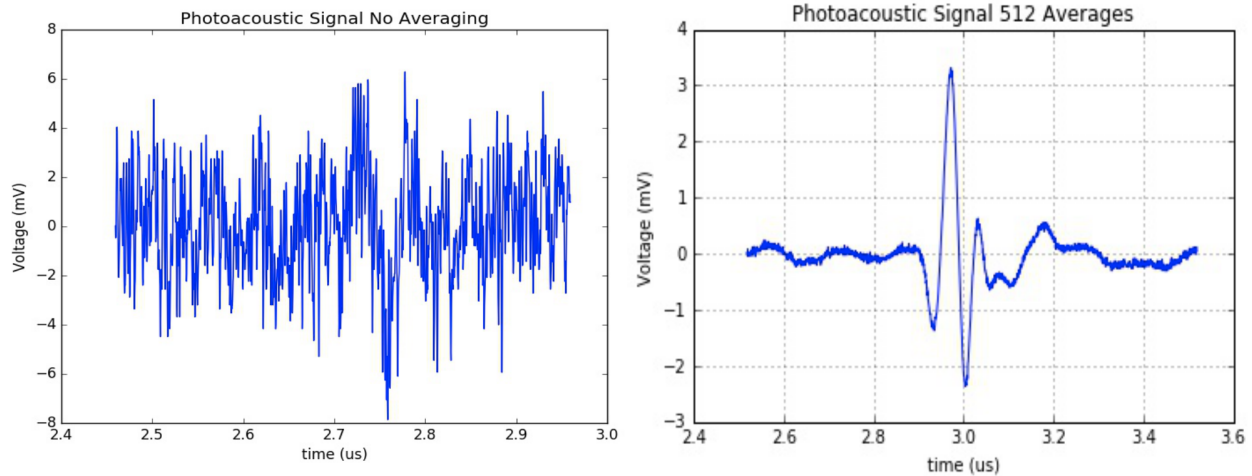


Figure 3.12: Raw oscilloscope results from the single-element ultrasound transducer (left) and oscilloscope results from the single-element ultrasound transducer averaged 512 times (right).

either our ultrasound or photoacoustic imaging system. For ultrasound imaging with this probe we find that the lateral resolution is 0.30 mm and for photoacoustic imaging we find a lateral resolution of 0.74 mm after applying a bandpass filter with a FWHM bandwidth of 2 MHz and a center frequency of 13 MHz to the photoacoustic signal. The filter removed low frequency content believed to be due to lateral modes in the annular array transducer. This gives a photoacoustic resolution that is 2.47 times the resolution of ultrasound. In figure 3.13 we see reduced side lobes in the experimental data and we believe this is due to a combination of the presence of a backing layer and an effective apodization effect due to the element being part of a larger, kerfless array rather than an actual single element. While we can explain this difference in side lobes, the difference of 2 dB would not matter for imaging since measurement error would account for a larger difference.

For ultrasound, the lateral resolution is determined by the beam width of the ultrasound probe which is dependent on the aperture width of the transducer. This can be seen in figure 3.15 which shows the beam pattern at a given distance away from the transducer face and the dependence of this beam pattern on the transducer diameter. The lateral resolution is often calculated as the -3 dB beamwidth at any given depth from the transducer and so we can see that the lateral resolution will increase as we move axially from the focal zone at the near field/far field transition. We can decrease the beamwidth of the ultrasound transducer by focusing the sound using either an acoustic lens or by delaying element pulses

of a multi-element transducer.

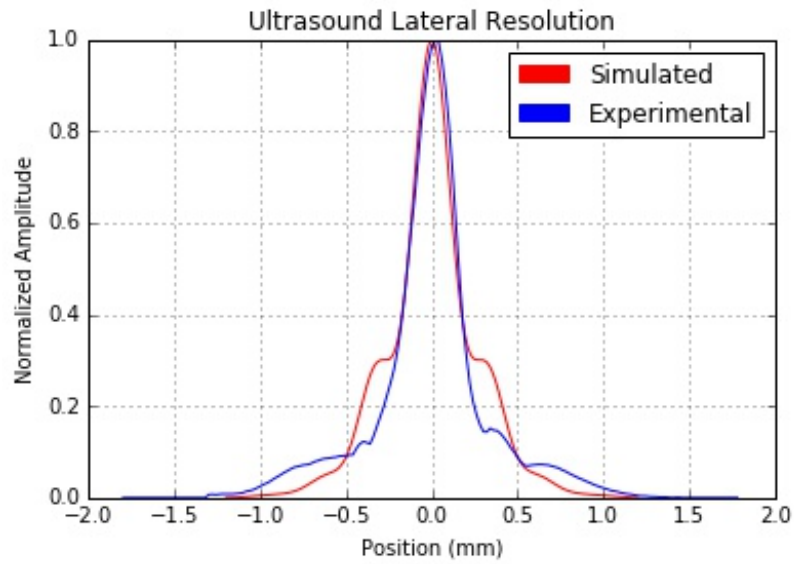


Figure 3.13: Plot of simulated and experimental results of the lateral point spread function for Ultrasound imaging of the hair target with the single element transducer.

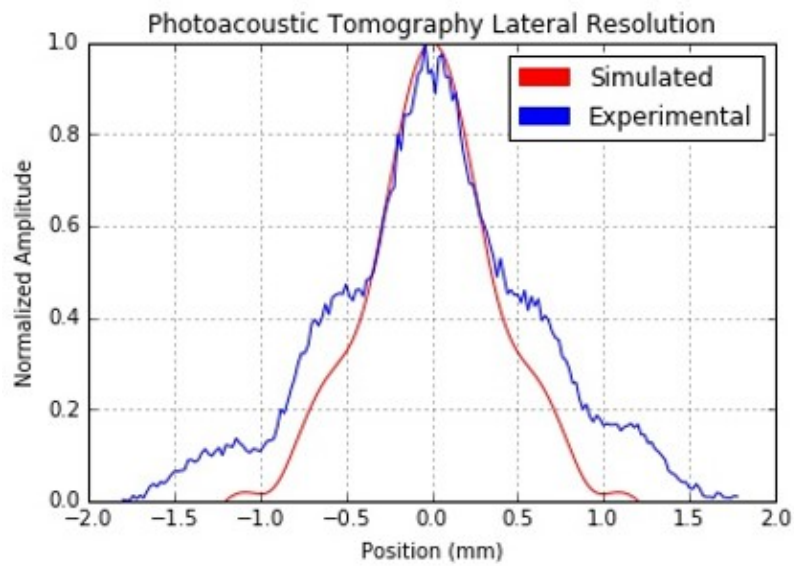


Figure 3.14: Plot of simulated and filtered experimental results of the lateral point spread function for Photoacoustic imaging of the hair target with the single element transducer.

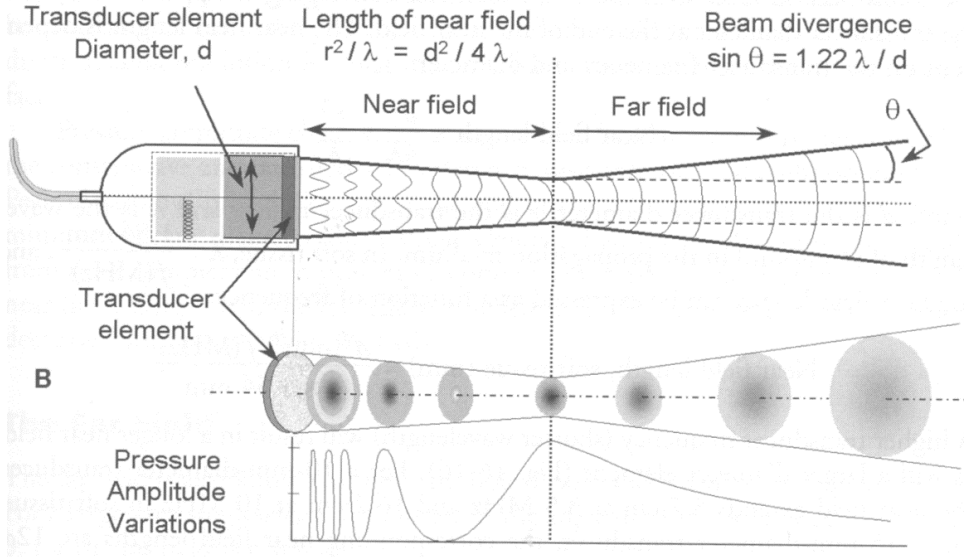


Figure 3.15: Diagram of the beam width at various distances from the transducer face [3].

In photoacoustic tomography, the lateral resolution is also dependent on the beamwidth of the ultrasound probe but the difference between the two will come from the fact that the ultrasound transducer focuses on transmit and also on receive and so has a two-way focus where the effective two-way transmit-receive aperture is the convolution of the transducer aperture with itself which gives reduced -3 dB beamwidth. Photoacoustic imaging uses the pressure wave created by the photoacoustic effect and so has no transmit pulse and can only focus on receive. This one-way focus means that we should expect the photoacoustic lateral resolution to be approximately two times the width of the ultrasound lateral resolution. Essentially, if the 'natural' focus were a true focus, the two-way intensity at the focus would be the square of the one-way focus and would have a FWHM of approximately one half of the one-way focus which agrees with our results.

We can simulate the near field for our transducer by using a Fresnel-Kirchhoff diffraction integral described by Gillen and Guha [10]. In this paper, they formulate the following equation in order to calculate this field:

$$\vec{E}(P_1) = \frac{kz_1}{i2\pi} \iint \vec{E}_{z=0} \frac{e^{ik\rho}}{\rho^2} dx_0 dy_0 \quad (3.2)$$

Where $\rho = \sqrt{(x_1 - x_0)^2 + (y_1 - y_0)^2 + z_1^2}$, x_1 , y_1 , and z_1 , are the x, y, and z coordinates of the field point P_1 and x_0 and y_0 are the x and y coordinates of the aperture at $z = 0$.

$\vec{E}_{z=0}$ is the field at the aperture, and k is the wave number. This equation adds spherical waves that have been weighted by the aperture and is a solution to the homogeneous wave equation. This approximates the aperture as an infinite number of point sources at x_0 and y_0 and calculates the diffraction pattern at each point P_1 created by such an aperture.

This approach was used to simulate both the ultrasound and photoacoustic point spread functions for our single element transducer and this simulated data was seen along side our experimental results in figures 3.13 and 3.14. We can see in these figures that the simulated results fit the ultrasound data quite well, with the simulated lateral resolution being 0.29 mm and our experimental lateral resolution being 0.30 mm. The simulated photoacoustic results show that the lateral resolution should have been 0.76 mm and the experimental results gave 0.74 mm after filtering using a 12 MHz to 14 MHz bandpass filter to remove lateral modes that artificially degraded the lateral resolution including a large 4 MHz component we believe to be caused by a lateral mode of the kerfless array. We believe the effect of these lateral modes appear in the photoacoustic PSF but not the ultrasound PSF because the bandwidth of the photoacoustic signal is significantly larger than the bandwidth of the ultrasound signal on transmit. The sensitivity of the photoacoustic signal to the lateral modes is specific to this kerfless, annular transducer and is not a problem with photoacoustic signals generally. When the lateral mode is filtered out, the measured resolution matches the theoretical. We should also expect that when we move to the 64-element phased ultrasound array, these additional lower frequency contributions would not contribute to the signal since it is unique to the kerfless array.

The final piece of data we wanted to bring from this single element experiment was the axial resolution in the case of photoacoustic tomography. Axial resolution depends on the pulse width of the photoacoustic signal and is mathematically described as half the axial pulse length. Therefore, a pulse with a broad bandwidth will have a short pulse length and consequently a high axial resolution. The pulse width is determined by the number of cycles multiplied by the wavelength. We can see from the photoacoustic emission spectrum of the hair in figure 3.9 that the number of cycles in the photoacoustic signal is one. The pulse length of the photoacoustic signal was measured to be 115 μm which means that the axial resolution is 57.5 μm . The pulse width of the ultrasound pulse echo was measured to be 416 μm and therefore has an axial resolution of 208 μm . The photoacoustic signal therefore showed an increase of axial resolution of 1.8 times. The axial resolution is greatly limited by

the 12-14 MHz bandpass filter applied to ultrasound and photoacoustic signals as compared to the axial resolution achieved when the signals are unfiltered.

Through this single element experiment we found that the photoacoustic signal has an SNR of 0.35 with no averaging and energy per pulse of $500 \mu\text{J}$, a lateral resolution of 0.74 mm with filtering and an axial resolution of $57.5 \mu\text{m}$. This low lateral resolution can be explained by the fact that the ultrasound transducer is not focused. This has allowed us to draw several conclusions and get an intuitive sense of how to get photoacoustic tomography working with the 64-element array. We now know that we need to average the photoacoustic signal to be above the noise floor, and that we should expect 2.5 times less lateral resolution than ultrasound. Based on a theoretical model, the center frequency of the photoacoustic emission spectrum of the hair is around 7 MHz but with a -20 dB bandwidth of 80 MHz which means that while pairing our laser with a 7 MHz-center frequency transducer would be optimal, the laser would produce measurable photoacoustic signals for transducer with >50 MHz center frequency. In the ideal case we would therefore want to work with a transducer with a center frequency as close to 7 MHz as possible in order to maximize the amount of our signal in the bandwidth of the ultrasound transducer.

3.5 40 MHz 64-Element Phased Array Ultrasound Transducer Experiment

With the knowledge obtained from the single element transducer experiments, we were now ready to use the more complicated 64-element phased array ultrasound transducer system to obtain a photoacoustic image. With a 64-element array, we now have to take the received signals from each of the 64 channels and beamform this data to produce an image of the photoacoustic target. Having multiple elements allows us to focus the transducer everywhere in the plane perpendicular to the transducer face and not just at the geometric focus we have with a single element transducer. In order to achieve an image with the 64-element system, we made changes to the ultrasound system host software to implement averaging in the system and accommodate the differences in timing with collecting a photoacoustic signal which takes half the time to reach the transducer due to the sound only travelling from the target to the transducer, we need to beamform the channel data obtained from the ultrasound transducer, and we need to improve the resulting images as best as possible. Once we produce these 2D images with the 64-element array and perform improvements by filtering and adaptive beamforming, we will have excellent groundwork to be able to move

on to producing 3D photoacoustic images with the 128-element crossed-electrode array. The 2D imaging experiments also help us further trouble shoot any issues we might have in the final 3D imaging process and give us an idea of the steps required to produce and process these images.

3.5.1 Ultrasound System Host Software Update for Photoacoustics

Because of the low SNR measured in the previous set of experiments, we modified the ultrasound acquisition software to enable averaging over arbitrarily long time, ensuring that a detectable photoacoustic signal could be obtained.

The other change that needed to be made to the ultrasound system host software is to alter the timing at which the photoacoustic signal is received due to the fact that there is no longer a transmit pulse being sent. Previously there was a delay between transmit and receive in order to account for the time it takes for sound to travel to a target and back. With photoacoustics, the pulse of light sent from the laser to the target travels at the speed of light and so happens almost instantaneously compared to the speed of sound travelling through the medium. This resulted in the receive delay initially being too long to pick up the photoacoustic signal and so after reducing that delay time we were able to get a result. These changes were performed by Chris Samson [28]. The maximum repetition rate that the laser can pulse at is 1 kHz but the channel data software cannot acquire data that quickly and so instead it took approximately 300 seconds to acquire images from 1000 pulses. This significantly limited the rate at which images could be captured.

3.5.2 Image Processing

After making the necessary changes to the ultrasound system host software, we were able to set up the side illumination experiment in figure 3.2 and record the raw data seen in figure 3.16. There were eight channels that do not have pulse echo data and this is due to some elements of the ultrasound probe being dead in this transducer.

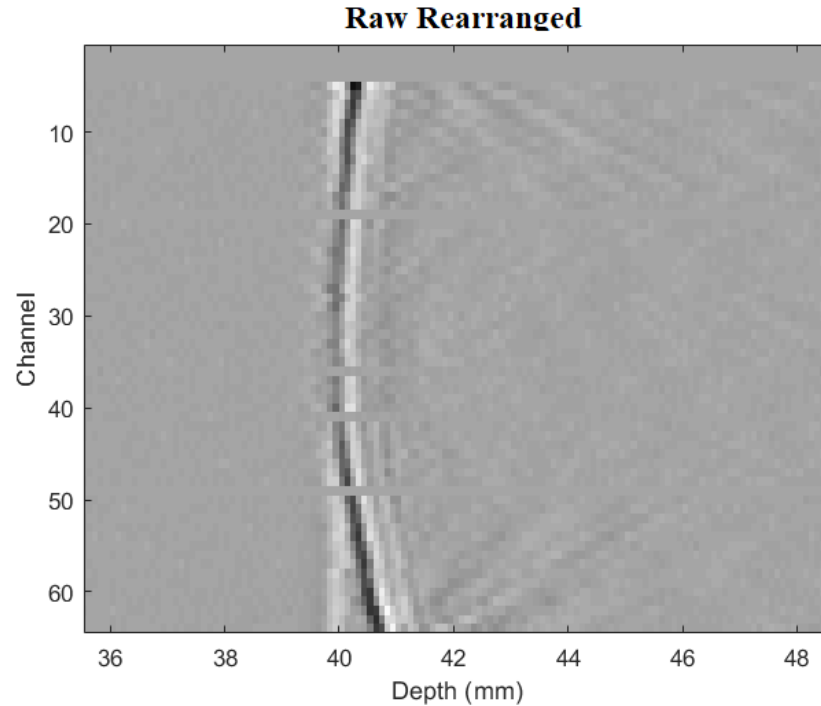


Figure 3.16: Raw PAT channel data of the 64-element phased array transducer with the 808 nm diode bar laser focused on a hair target in water.

We then processed this data in order to produce an image of the hair target. In order to perform this we designed a program that followed the steps in figure 3.17:

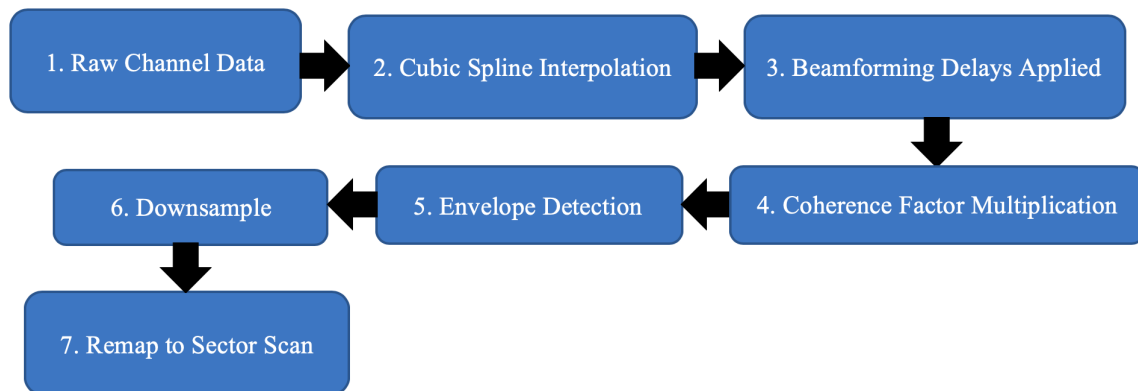


Figure 3.17: A flowchart detailing the steps of processing the raw channel data into a beam-formed image.

Importing the raw channel data (step 1) produced 64 columns with 1024 axial data points in the time domain. In step 2, a Cubic Spline Interpolation was used to increase the number

of data points to 10240 in the time domain in order to provide us with more precision when applying the time delays. Even though it is a slower interpolation method than a finite impulse response or matched filter, cubic spline interpolation was chosen due to the fact that it would not cause a time shift in our data and doing beamforming in post did not necessitate a faster method. In step 3, we implemented a function to apply the time delays between a given element in the array and the closest element to the target point according to equation 3.3.

$$\Delta t(n, x, y) = \frac{\sqrt{(y - (n - 1)d)^2 + x^2}}{c} - t_{min} \quad (3.3)$$

To understand how this equation is formed, we can look at the diagram in figure 3.18. The first term in this equation calculates the time it takes for the sound to travel from the chosen focal point to a given element of the transducer, n . Here, d , is the element pitch which is $38 \mu\text{m}$ for the 64-element transducer, c is the speed of sound in water which is 1498 m/s , and h is the standoff distance which is the distance between the transducer face and the location where the first time domain data points are recorded, 1.5 mm . The points x and y represent the location of the focal point and so subtracting $(n - 1)d$ from y gives the vertical component of the distance between the given element n and the focus. The time t_{min} is an arbitrary start time to adjust offset. Using this equation, we step through 30° to either side of the transducer at 10240 focal points along the radius, r , where $x = r \cos \theta$ and $y = r \sin \theta$. At each focal point we apply the delays and add the resulting signals together using the delay-and-sum method. To reduce side lobes we implemented adaptive beamforming by multiplying the delays by a coherence factor (Step 4), see appendix A.

In step 5, we then take the resulting array and perform envelope detection using a Hilbert transform by creating the analytic signal of the pulse-echoes. The analytic signal is a complex signal whose real component is the original signal and whose imaginary component is the Hilbert transform of the original signal. The envelope of a signal is given by the magnitude of the analytical signal as in equation 3.4, where $x(t)$ is the original signal and $\hat{x}(t)$ is the Hilbert transform.

$$e(t) = \sqrt{x(t)^2 + \hat{x}(t)^2} \quad (3.4)$$

In step 6, we downsample our data back to 1024 time domain points since we no longer needed to manipulate the signal any further. We then remap our data from a rectangular

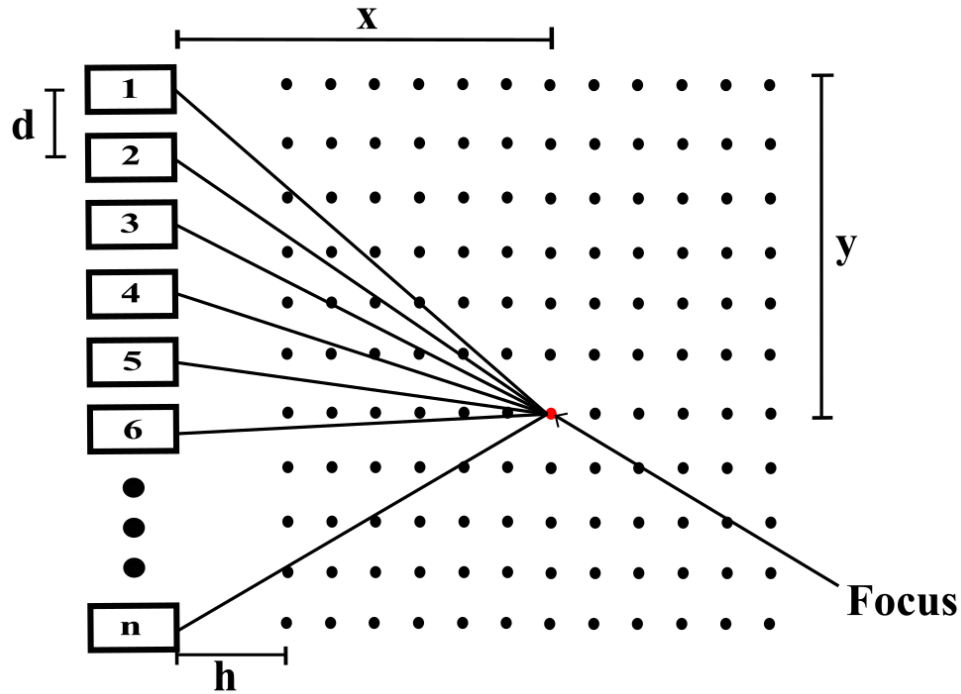


Figure 3.18: A diagram showing how the delays are applied to the channel data [2]. Where n is a given element of a transducer, d , is the element pitch ($38 \mu\text{m}$), x and y represent the coordinates of the focus, and h is the standoff distance.

array into an image with the sector shape called a sector scan in which the phased array collected the data (step 7). We scaled the intensity to a dB intensity scale to display the image and got the final image of the hair target in figure 3.19.

3.5.3 Images of Hair Target with 40 MHz Transducer

We were able to achieve a photoacoustic image of the hair target which can be seen in figure 3.19 b). The -3 dB lateral resolution of this photoacoustic image was measured to be 0.256 mm and when we compare this to the lateral resolution of the 40 MHz ultrasound which is 0.08 mm (3.19 a)), we see that we have an increase in lateral resolution of 3.2 times the ultrasound resolution width. Here, the use of the -3dB beamwidth is appropriate because resolution of PAT is determined by the ultrasound on one way receive only.

We can also see in this image that there are significant side lobes coming off of the main hair target image which are characteristic in photoacoustic images [30]. These side lobe artifacts greatly reduce the visibility of the spot created by the hair in this image and so

step 4 in the image processing program included multiplying delays by a coherence factor which weighs incoherent portions of the image (such as the sidelobes) less strongly than coherent parts (such as the main lobe) to achieve figure 3.19 c).

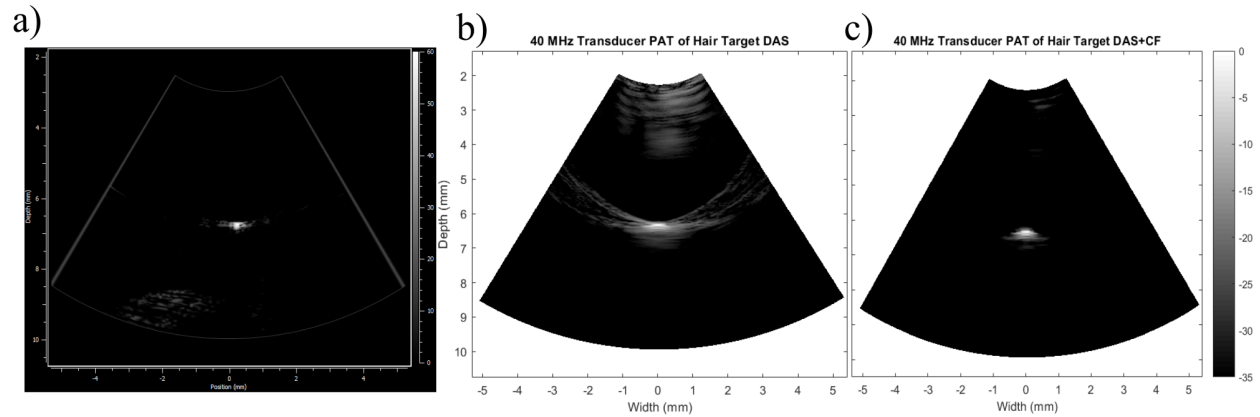


Figure 3.19: Images of a hair target in water using a) ultrasound displayed with a dynamic range of -60 dB b) photoacoustic imaging with delay and sum beamforming applied and a -35 dB dynamic range plotted on a gray scale and c) photoacoustic imaging with coherence factor and delay and sum beamforming applied and a -35 dB dynamic range plotted on a gray scale .

If we look at the lateral point spread function for the photoacoustic images reconstructed using both delay and sum and delay and sum with coherence factor beamforming, we can see that the side lobes have been decreased by 15 to 20 dB by adding the coherence factor weighting. This strongly agrees with the improvements seen by Park et. al. in the reduction of their side lobes. We can also look at the -3 dB beamwidth for these point spread functions to find that we get an increase in the lateral resolution from 0.256 mm to 0.165 mm by using a coherence factor weighting. Comparing this to the ultrasound lateral resolution, we see that this new lateral resolution is 2.06 times the lateral resolution of ultrasound.

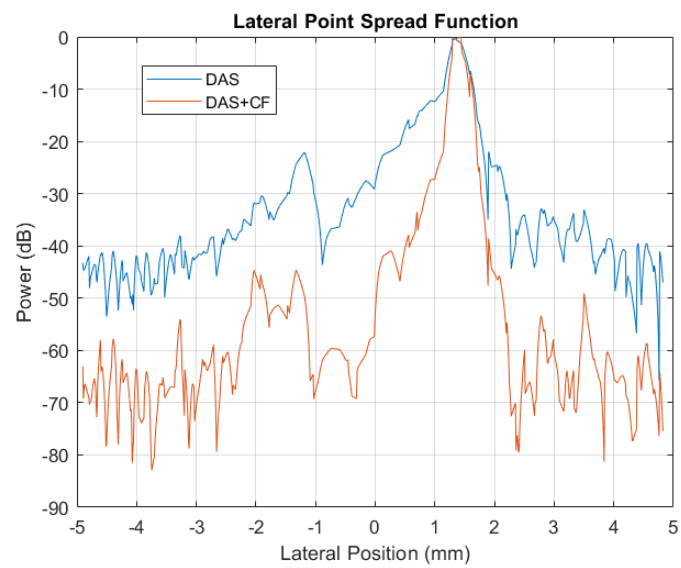


Figure 3.20: A plot of the lateral point spread function for both an image created using delay and sum (DAS) beamforming and an image created using delay and sum beamforming with a coherence factor applied (DAS+CF).

Chapter 4

Tissue-mimicking Phantom

Images in the previous experiments were taken with a single hair target in water. Since water has a low absorption around 10^{-1} to 10^{-2} cm^{-1} at 808 nm compared to 10^2 cm^{-1} for melanin, the photoacoustic signal has a much higher contrast than it would in a tissue with other absorbers such as lipids. Therefore, in order to verify that our photoacoustic endoscopes have met the requirements for imaging in tissue we must create a tissue-mimicking phantom to get a better idea of the contrast in tissue. Other experiments have shown good contrast in tissue phantoms such as in figure 4.1 where they used slices of chicken breast to observe the performance of diode laser based photoacoustic tomography [30].

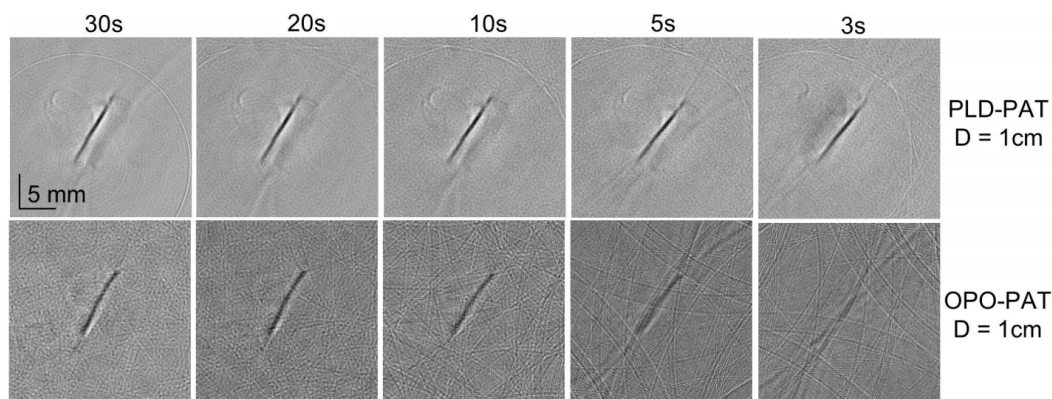


Figure 4.1: Reconstructed images of horse-hair phantom using 5 MHz transducer: PAT images acquired using a pulsed laser diode (PLD-PAT)(top) and a Nd:YAG laser with an optical parametric oscillator (OPO-PAT)(bottom) at 1cm depth. All images have the same scale bar. [30] © 2015 Optical Society of America.

4.1 Tissue Properties and Materials

A standard procedure for creating a tissue-mimicking phantom is to use a gelatin-based medium with additives introduced to alter the optical and acoustic properties [5, 6]. We aim to mimic the acoustic and optical properties of human brain tissue in order to accurately assess the effectiveness of the photoacoustic images obtained using our photoacoustic

endoscope. The key acoustic and optical properties we wish to reproduce in this tissue phantom are the ultrasound backscattering coefficient and the reduced scattering coefficient, respectively.

The scattering of sound in tissue occurs due to a difference in the acoustic impedance of the scattering particles in the medium and the acoustic impedance of the medium itself. Acoustic impedance is the product of the density and speed of sound in the material which means that as the sound waves travel through the medium, inconsistencies in the density causes reflections of the sound waves to be sent back to the ultrasound transducer as in image 4.2. These backscattered waves sum with the reflection from the imaging target and the total wave is collected by the ultrasound transducer. These backscattering events add constructively and destructively in the final image to create what is called speckle, noise in the image consisting of bright and dark spots. The ultrasound backscattering coefficient, is commonly used to quantify these scattering properties in tissue and is defined as the differential scattering cross section per unit volume and can be influenced by the size, shape, and density of the scattering particles [13].

The amount of light that will be able to reach our target will be governed by the attenuation via scattering and absorption as the photons travel through the tissue. This causes a reduction in the peak intensity of the illumination as well as an increase in the beam radius as light travels deeper into the tissue which can be seen in figure 4.3. Optical absorption in tissue is determined by the absorption coefficient, μ_a , which changes based on the tissue being imaged. If we look at various biochemical molecules found in the body and their absorption coefficients at 808nm in figure 3.4, we can see that the main absorber is blood and so we mainly focus on mimicking the scattering behaviour of light in tissue because the effects of scattering on the attenuation of light reaching our imaging target will vastly dominate over the effects of absorption. The intensity of the light that will ultimately reach the imaging target is described by the Beer-Lambert Law, $I(z) = I_0 e^{-[\mu_a + \mu_s]z}$, in which the initial intensity, I_0 , will exponentially decay at distance z in the tissue based on the absorption coefficient, μ_a , and the scattering coefficient, μ_s .

The scattering of light in tissue occurs when photons collide with particles in the tissue with a different index of refraction than the surrounding medium and their direction of travel is altered from their original trajectory. We can see this in figure 4.4, which are slices of the illumination pattern at 2 mm increments, where each photon is scattered as it hits

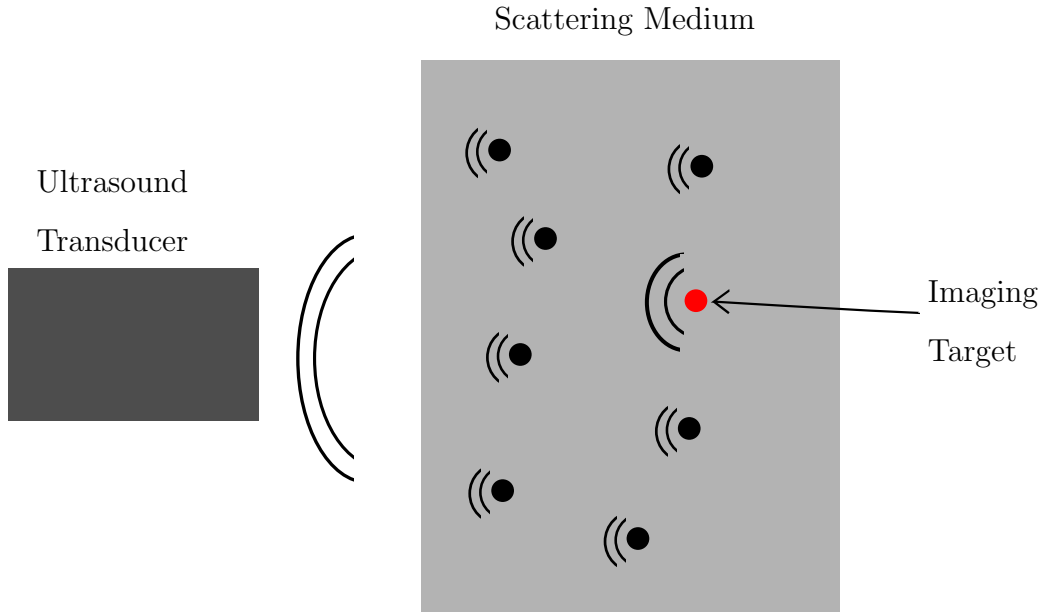


Figure 4.2: The backscattering of ultrasound in a scattering medium.

various particles while it travels through the medium. This results in a much wider light beam at the depth of the imaging target and so fewer photons and a lower intensity. The amount of scattering that occurs in a medium is often described by the scattering coefficient, μ_s (cm^{-1}), which is defined as the product of the effective scattering cross-section of the scattering particle, σ_s (cm^2), and the number of scatterers per volume, ρ_s ($1/\text{cm}^3$). There is also a factor used in combination with this coefficient called the anisotropy factor, g , which describes the average direction in which particles scatter relative to the incident direction, given by the equation $g = \langle \cos(\theta) \rangle$, where $g = 0$ scattering 90° to the incident direction, $g = 1$ scattering forward in the same direction, and $g = -1$ scattering directly backward. Tissue typically has a value of $g \sim 0.9$. These two factors are used to calculate the reduced scattering coefficient, $\mu'_s = \mu_s(1 - g)$, which describes the distance that light travels in tissue before its direction is completely uncorrelated to its incident direction. Including the anisotropy factor allows us to account for the fact that scattering events in biological tissue usually result in the photons scattering in the forward direction and typically do not deviate as much from the incident direction. To make sense of this physically, we can use the scattering coefficient, μ_s ,

to calculate the mean free path, $\frac{1}{\mu_s}$, which describes the average distance between scattering events, and we can use the reduced scattering coefficient, μ'_s , to calculate the transport mean free path, $\frac{1}{\mu'_s}$, which describes the average distance over which the direction of the photons is random compared to the incident beam.

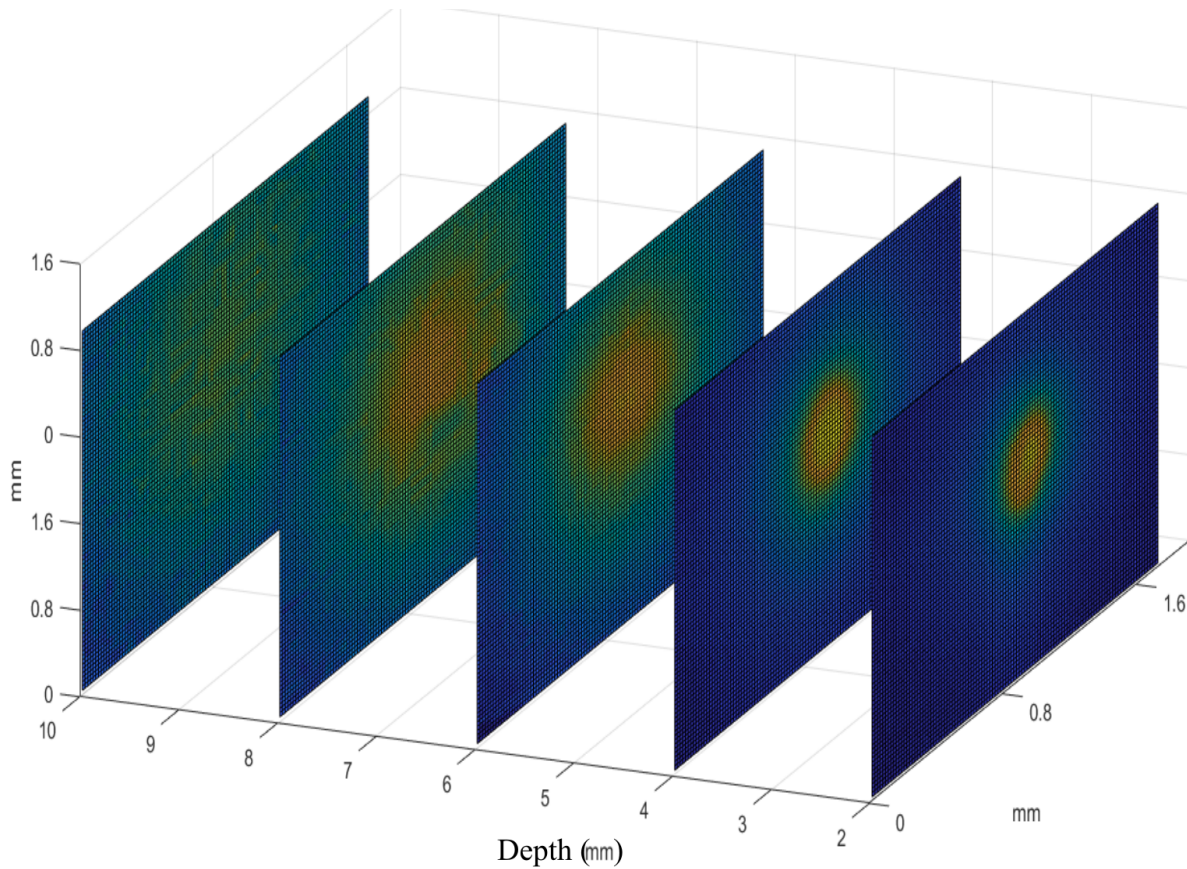


Figure 4.3: Image of the scattering of light through a tissue phantom every 2mm in depth.

While trying to make a phantom to mimic tissue, we aim to make the ultrasound backscattering coefficient and reduced scattering coefficient as close to the values for brain as possible. The ultrasound backscattering coefficient for human brain is $0.48 \text{ cm}^{-1} \text{ Sr}^{-1}$ at a center frequency of 30 MHz [21] and the reduced optical scattering coefficient is 10 cm^{-1} for human brain tissue [14]. In tissue mimicking phantoms, silicon dioxide particles (SiO_2) are often used to control desired ultrasound backscatter strength and intralipid solutions are often used to create a desired optical scattering coefficient [6, 16]. By varying the concentrations of SiO_2 and intralipid we can control both properties independently because silicon dioxide

is a good backscatterer but has a similar index of refraction to gelatin and so will not significantly contribute to the optical scattering, while intralipid solution is a good optical scatterer but has a similar acoustic impedance to water and so will not significantly contribute to the backscattering [5].

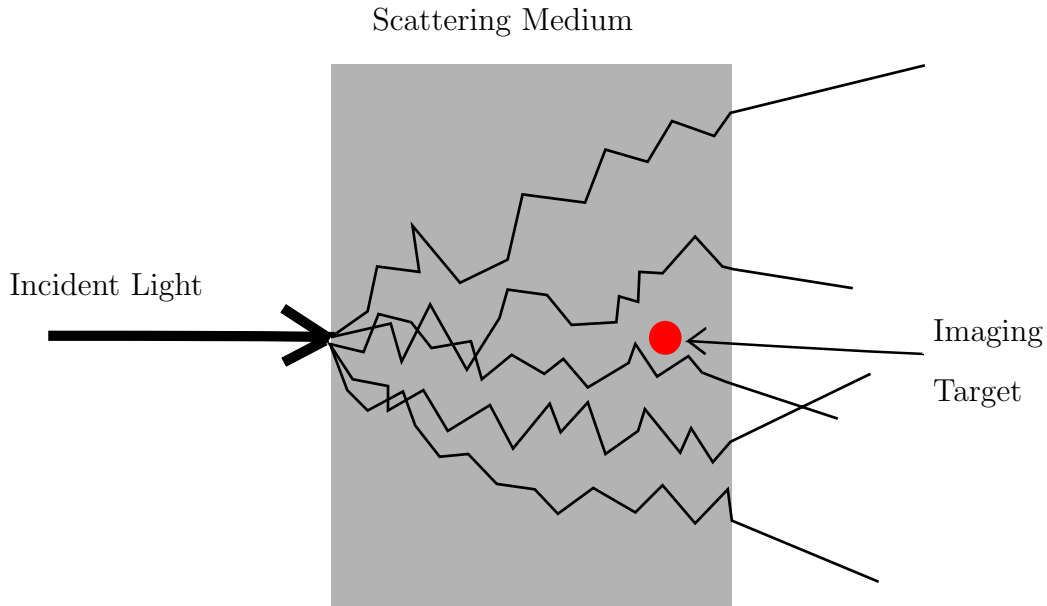


Figure 4.4: The scattering of light in a scattering medium.

Following several papers that used silica or intralipid [5, 9] we decided to use a type-A, 300-gel strength gelatin powder made from acid-cured porcine skin (G2500, Sigma-Aldrich Corp., St. Louis, MO) combined with deionized water to produce a gelatin medium in which to add our acoustic and optical scatterers. Following the procedures of these experiments, 2% (mass/volume) silicon dioxide powder (MIN-U-SIL-40, U.S. Silica Co., Mill Creek, OK) with 40 μm particles was added to achieve a backscattering coefficient of $\sim 0.59 \text{ cm}^{-1} \text{ Sr}^{-1}$ at a center frequency of 30 MHz [5] and 5% (volume/volume) of 20% Intralipid emulsion (I141, Sigma-Aldrich Corp., St. Louis, MO) was added to achieve a reduced scattering coefficient of $\sim 10 \text{ cm}^{-1}$ [16]. The concentration of silica was found by extrapolating the results of figure 4.5 and calculations using $\eta(f) = Af^n$ where regression gave the constants $A =$

$4.63 \times 10^{-2} \text{ cm}^{-1} \text{ sr}^{-1} \text{ MHz}^{-1}$, $n = 0.7496$, and $\eta(f)$ is the frequency-dependent backscattering coefficient in $\text{cm}^{-1} \text{ sr}^{-1}$.

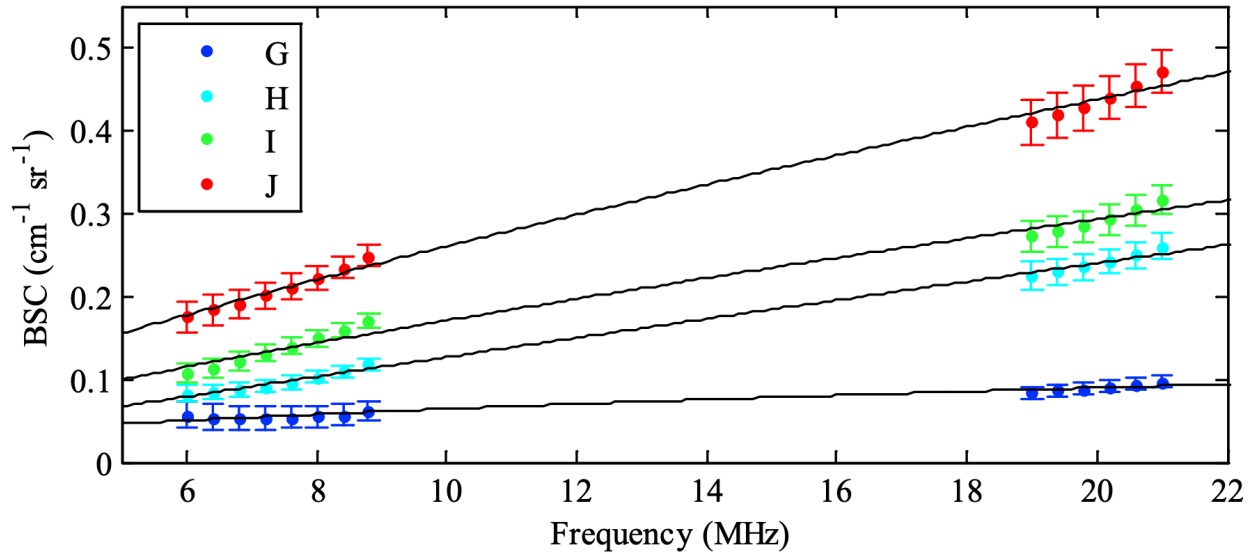
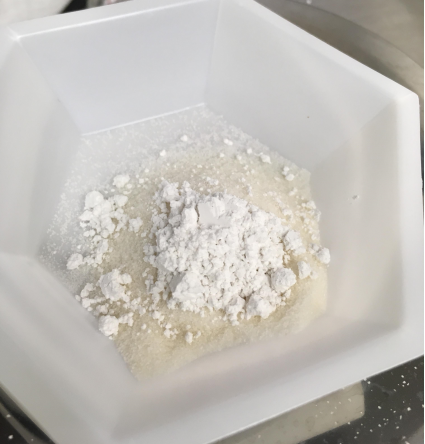
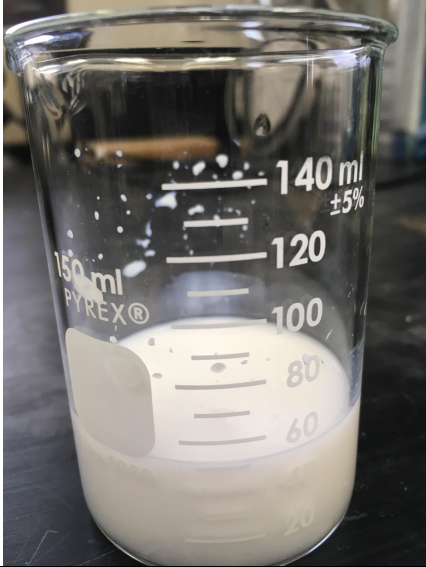



Figure 4.5: The dependence of the ultrasound backscatter coefficient (BSC) with increasing silica concentration for phantoms G, H, I, J with silica concentration of 0.1, 0.5, 1.0, and 2.0% mass/volume respectively. Error bars were calculated from 2500 positions on 3 samples [5] © 2011 Optical Society of America.

4.2 Phantom Fabrication Procedure

Fabrication Step	Image of Fabrication Step
<ol style="list-style-type: none"> Combine 8% (mass/volume) gelatin powder with 2% (mass/volume) silica powder. Mix until uniform. 	

Fabrication Step	Image of Fabrication Step
<p>2. Combine deionized water with 5% (volume/volume) of 20% Intralipid emulsion and mix until uniform. Heat the mixture to 30°C.</p>	
<p>3. Slowly combine the gelatin/silica powder with heated solution while stirring vigorously. Continue to heat the mixture to 37°C over 10 minutes. For longevity of the phantom, stir in 0.1% (volume/volume) 37% Formaldehyde Concentration (252549, Sigma-Aldrich Corp., St. Louis, MO) after the powder mixture has been added.</p>	

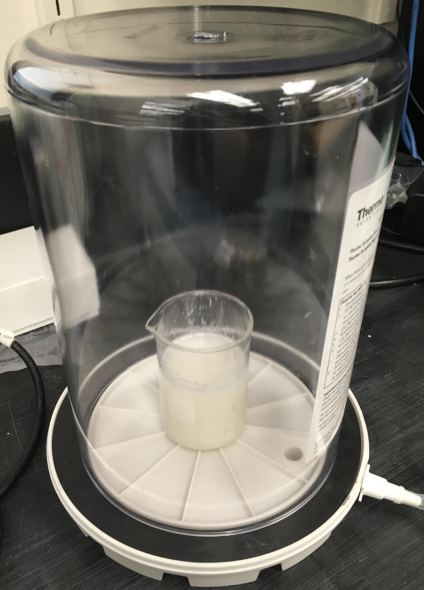
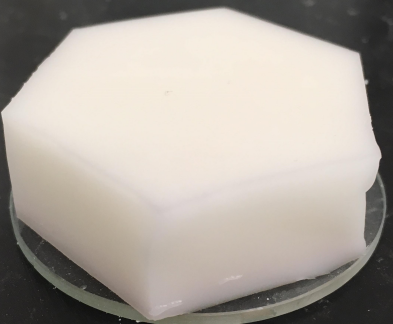
Fabrication Step	Image of Fabrication Step
<p>4. Place the phantom solution in a vacuum at 21 kPA for 10 minutes in order to remove any air bubbles introduced in the process. Transfer the solution to phantom mold using a syringe in order to minimize air reintroduction.</p>	
<p>5. Allow the solution to come to room temperature and then cool to 4°C for 24 hours to allow phantom to set and form cross-links.</p>	

Table 4.1: Phantom Fabrication Procedure

A mould was created which allowed for hairs to be attached on each staircase step so that once the tissue phantom is poured in, hair targets would be placed diagonally across the image window in vertical and horizontal steps on 2mm.

The hairs were attached by first soaking them in water so that they would expand fully and would not sag after absorbing water from the liquid phantom after it is poured in. The soaked hairs were pulled tight and attached by using uv curing epoxy. Finally, the matching top piece was attached to this half and uv curing epoxy was used again to bond them together as well as attach a glass slide to the front to create a smooth surface on both sides to reduce surface scattering in the final tissue phantom.

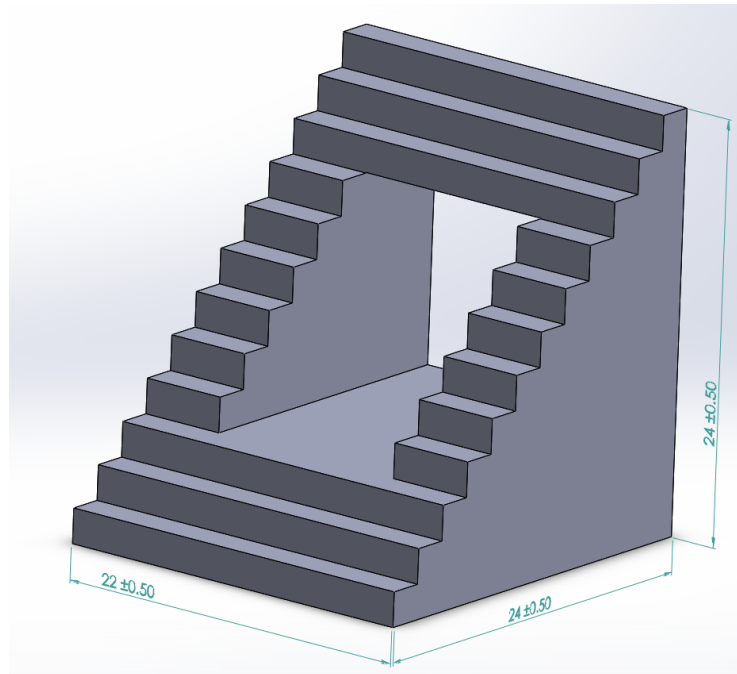


Figure 4.6: Model of the staircase mold for mounting hair targets.

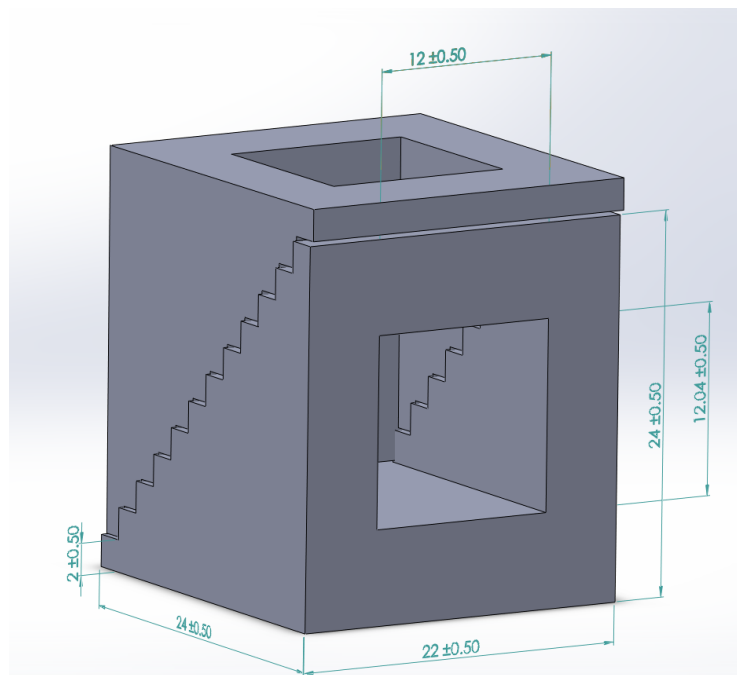


Figure 4.7: Model of the assembled staircase mold for mounting hair targets.

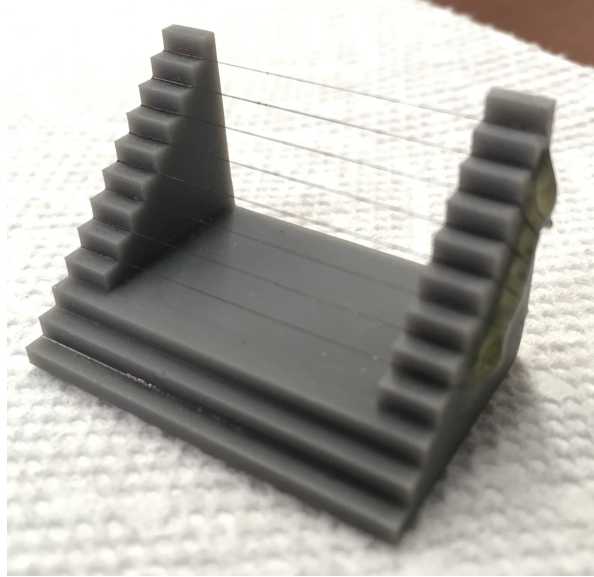


Figure 4.8: Pre-soaked hairs are epoxied to the staircase mould.

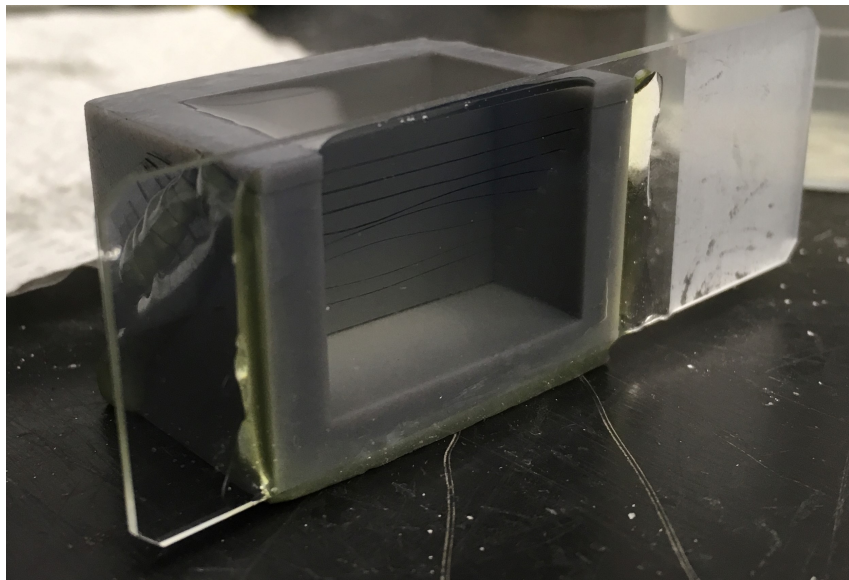


Figure 4.9: Top half of mould is attached as well as a glass slide using UV curing epoxy.

Finally, the phantom was prepared as instructed above and poured into the mould to create a tissue phantom imaging target with embedded hair targets. After it was allowed to sit and cure overnight, the glass slide was removed and the phantom was stored in deionized water so that it would not dry out.

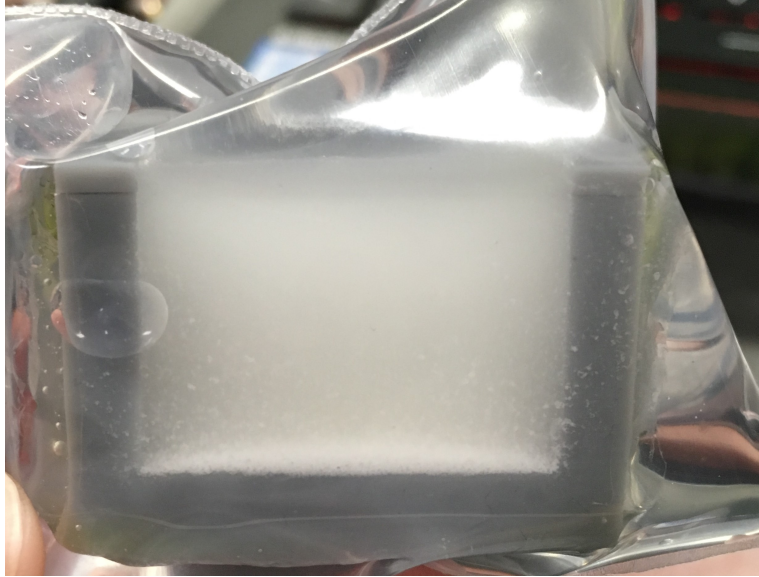


Figure 4.10: Phantom in the mold.

4.3 Verification of Phantom Properties

4.3.1 Backscattering of Ultrasound

In order to verify the ultrasound backscattering coefficient of the tissue phantom is close to the back scattering coefficient of brain, ultrasound images were captured of the phantom using a 50 MHz ultrasound transducer (VisualSonics Vevo[®] 2100 Linear Array Ultrasound System) with 65 dB dynamic range that had previously been used to capture images of a rat brain. This image of a rat brain is a sagittal view with grey and white matter at the top and structures such as the corpus callosum and diencephalon below. Clinically, we are focused on imaging the surface of the brain and so which to image primarily grey and white matter and so the region above the corpus callosum is where we wish to mimic in our tissue phantom. Comparing the images captured of the tissue phantom to the images of the rat brain, the pixel intensity can be used to compare the speckle pattern of the image created due to backscattering in each case. If the pixel intensity of the two images are similar at the same depth, this would suggest that the backscattering coefficient of brain tissue and the tissue phantom are also similar.

The first step was to create a tissue phantom that did not include silica in order to determine the effect of the intralipid emulsion on the backscattering coefficient and ensure

that changing the intralipid concentration would not change the backscattering coefficient as we predicted. Looking at the pixels in the red squares indicated in image 4.11, we can calculate the root mean square (RMS) amplitude of the data, $V_{RMS} = \sqrt{P}$, by first calculating the pixel signal power, $P = \frac{1}{N} \sum_{i=0}^N [v_i]^2$, in which v_i are the amplitudes of the pixels in each respective region and N is the total number of pixels in each region. Doing the same calculations for the regions in the rat brain image in figure 4.12, and then taking the average of these RMS values we find that the intralipid phantom as an average pixel intensity RMS value of 49.4 and the rat brain image has an average RMS value of 89.0. If we look at the individual RMS values from the regions of both of these images in figure 4.16, we see that the range of RMS values for intralipid (47 - 52) is far outside of the range of RMS values for the rat brain (84 - 96) and is also significantly smaller than the other silica samples and so we can say that the intralipid ultrasound backscattering is very small compared to the backscattering we see in brain tissue and so the silica particles will be what determines the overall backscattering of this tissue phantom.

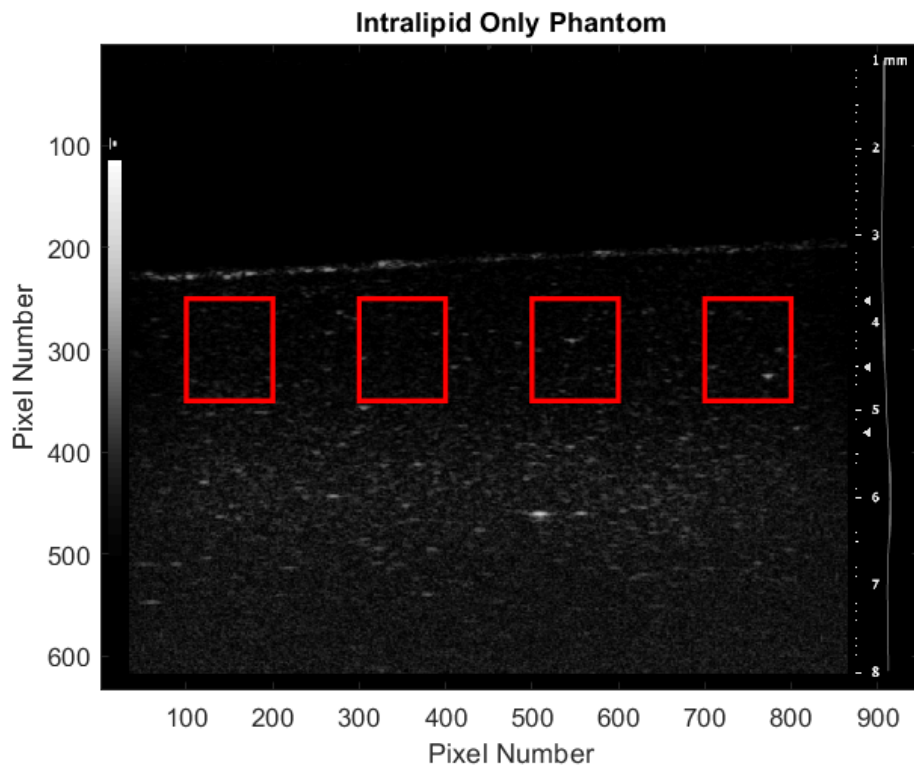


Figure 4.11: 50 MHz Ultrasound image of the tissue phantom with only gelatin and intralipid. The red regions depict the areas used to calculate RMS amplitudes.

Three different phantoms were then created to look at the difference in backscattering coefficients for tissue phantoms with 0.5%, 1%, and 2% (mass/volume) of silica as well as 5% (volume/volume) intralipid. If we again calculate the pixel intensity RMS amplitudes in the red squares in figures 4.13, 4.14, and 4.15, we get average RMS values of 87.5, 88.0, and 92.3 for the 0.5%, 1%, and 2% silica phantoms respectively. Comparing these values to the average RMS value for the rat brain tissue, 89.0, and also looking at the range of RMS values for each sample in figure 4.16, we see that, while the 1% silica solution is closest to the average RMS value of rat brain, all three solutions are within the range of RMS values in the rat brain image and so in all three solutions would be a good phantom in comparison to brain, we select the 2% silica solution so we know that the photoacoustic image will be effective even in brain that is a strong acoustic backscatterer. Since the RMS value for the 2% silica phantom is within the range of RMS values for the rat brain we find the tissue phantom to be a satisfactory replacement for the acoustic scattering effects of rat brain.

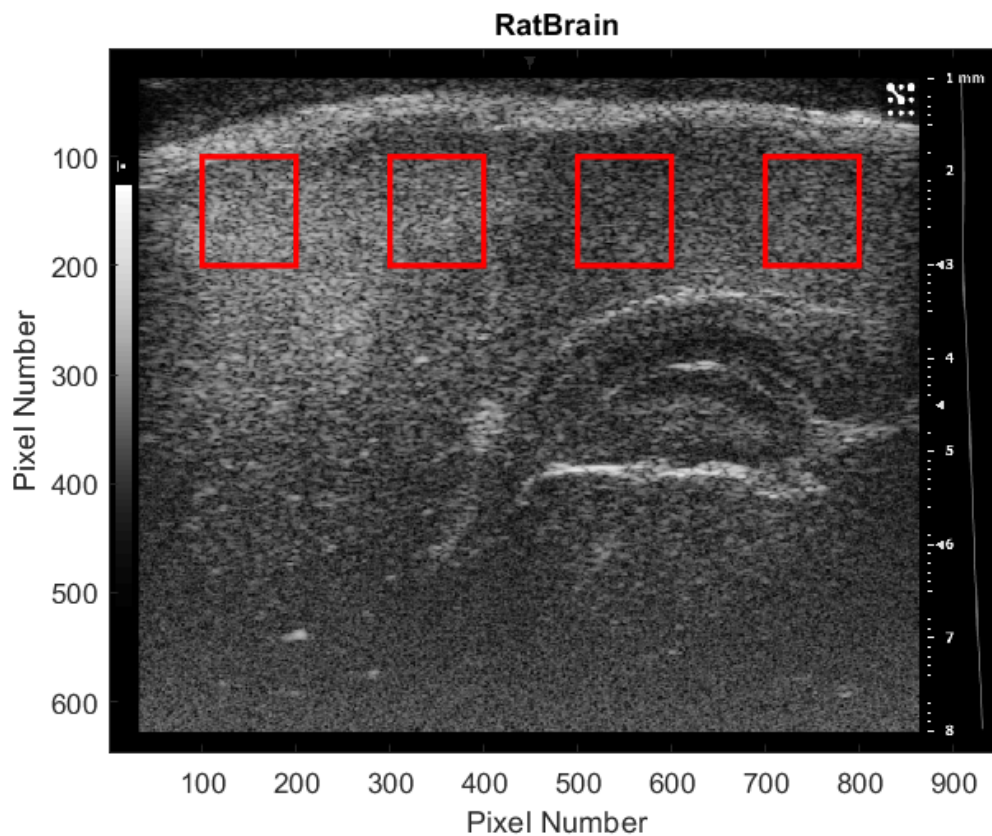


Figure 4.12: 50 MHz Ultrasound image of a rat brain. The red regions depict the areas used to calculate RMS amplitudes.

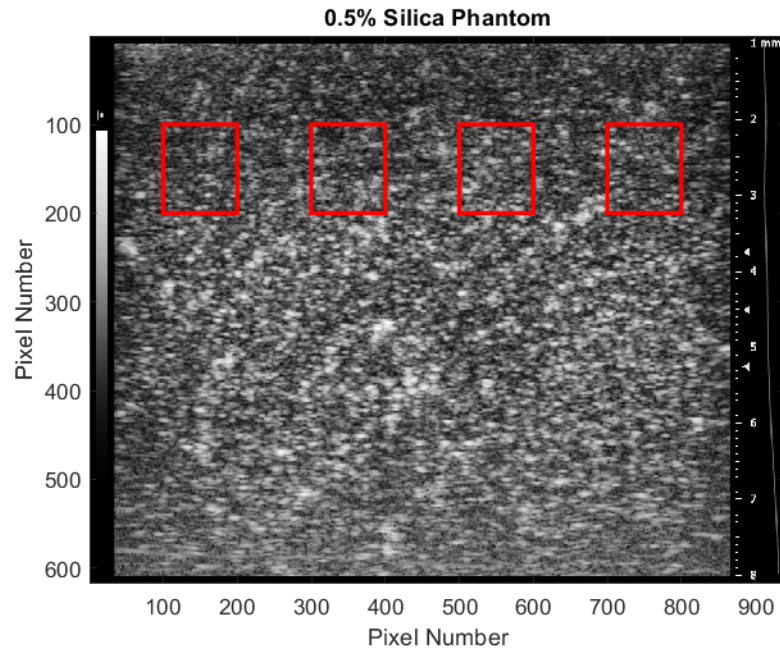


Figure 4.13: 50 MHz Ultrasound image of the tissue phantom with gelatin, intralipid, and 0.5% silica. The red regions depict the areas used to calculate RMS amplitudes.

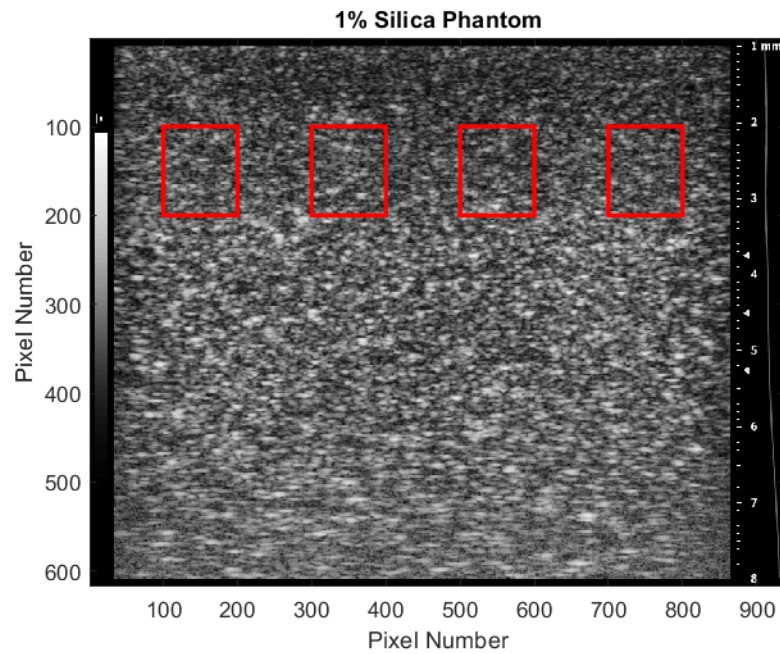


Figure 4.14: 50 MHz Ultrasound image of the tissue phantom with gelatin, intralipid, and 1% silica. The red regions depict the areas used to calculate RMS amplitudes.

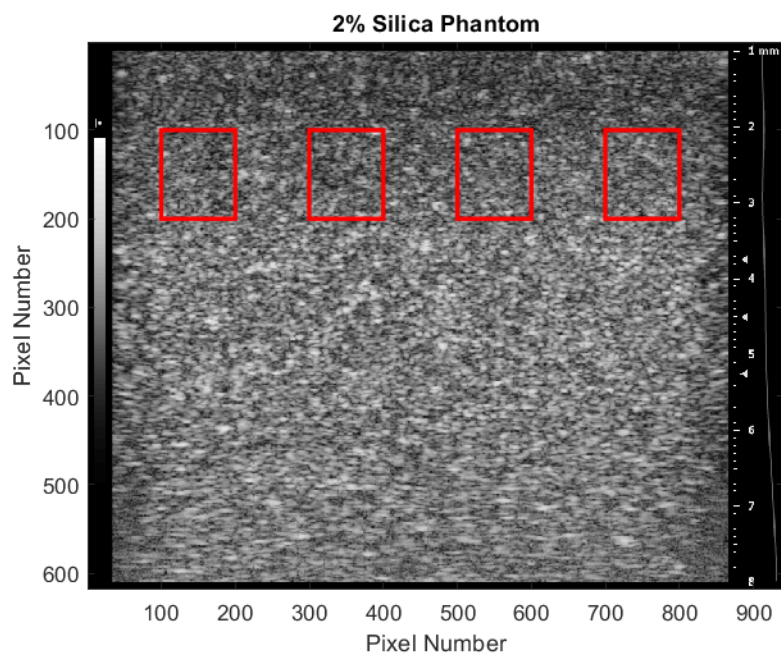


Figure 4.15: 50 MHz Ultrasound image of the tissue phantom with gelatin, intralipid, and 2% silica. The red regions depict the areas used to calculate RMS amplitudes.

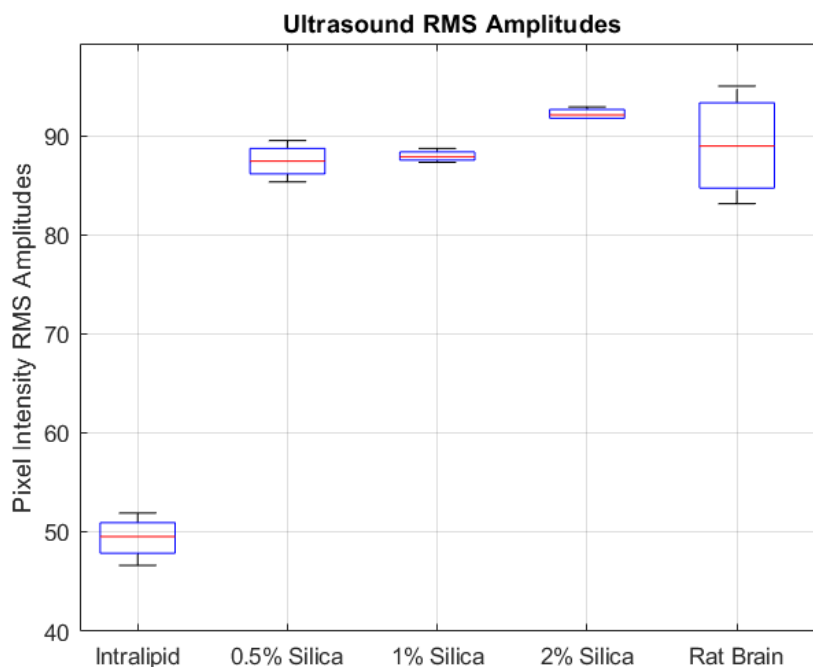


Figure 4.16: A box plot representation of the RMS amplitudes of each region in the ultrasound images including the average of the RMS amplitudes for each sample.

This plot shows that the RMS pixel intensities of the silica phantom are comparable to rat brain but this does not show that they are comparable to human brain which may scatter differently from rat brain. However, in the literature evaluation, human brain was found to have an ultrasound backscattering coefficient of $0.48 \text{ cm}^{-1} \text{ Sr}^{-1}$ at a center frequency of 30 MHz [21]. It was also calculated that 2% (mass/volume) silicon dioxide powder with $40 \mu\text{m}$ particles would produce a backscattering coefficient of $\eta(f) = \sim 0.59 \text{ cm}^{-1} \text{ Sr}^{-1}$ at a center frequency of 30 MHz [5]. This result was found using figure 4.5 and calculations using $\eta(f) = Af^n$ where regression gave the constants $A = 4.63 \times 10^{-2} \text{ cm}^{-1}\text{sr}^{-1} \text{ MHz}^{-1}$, and $n = 0.7496$. This shows that the backscattering coefficient is higher than the literature value of human brain and so we would expect our imaging device to perform better in brain than in a tissue phantom containing 2% (mass/volume) silica.

4.3.2 Estimate of Scattering Coefficient

In order to determine if the tissue phantom has an optical scattering coefficient comparable to that of brain, we set up an experiment following the methods of Lai, Xu, and Wang [16], to measure the diffuse reflectance pattern of both the phantom that only included intralipid, as well as the phantom that included both 2% silica and intralipid. By determining the scattering coefficient in the case of both phantoms, we can determine whether or not the addition of silica particles will affect the overall scattering coefficient of the medium and if this will need to be taken into consideration when determining the concentration of intralipid included in the tissue phantom.

The experiment we replicated from Lai, Xu, and Wang, used what is called oblique reflectometry which assumes that the optical absorption coefficient is much less than the reduced scattering coefficient. This method uses the fact that as photons travel through the scattering medium they will be scattered many times and with each scattering event their direction will change and eventually their direction will be completely randomized with respect to the incident beam direction. At this point, photons will travel back out of the medium and the pattern that these randomized photons create as they leave is called the diffuse reflectance. This phenomenon can be seen in figure 4.17. Using the center of the diffuse reflectance pattern and the center of the incident beam they find the distance between these points, Δx , which can then be used to calculate the reduced scattering coefficient due to the fact that the distance these photons travel in the medium before their direction is

randomized is the transport mean free path, $\frac{1}{\mu'_s}$. Lai, Wu, and Wang, use the relationship between Δx and μ'_s , equation 4.1, formulated by [31] and [18].

$$\Delta x = \frac{\sin \alpha_i}{n_{sample}(0.35\mu_a + \mu'_s)} \quad (4.1)$$

In this equation, n_{sample} is the index of refraction of the sample medium, μ_a is the optical absorption, and α_i is the angle of incidence of the incoming beam of photons. Lai, Xu, and Wang use a spectrophotometer to find $\mu_a = 0.12 \text{ cm}^{-1}$ for gelatin gel and they assume that the absorption coefficient for intralipid is negligible. We also find that the index of refraction of our sample medium, a mixture of intralipid, silica, and gelatin, is similar to the index of refraction of just gelatin, $n_{sample} \approx 1.5$ [33].

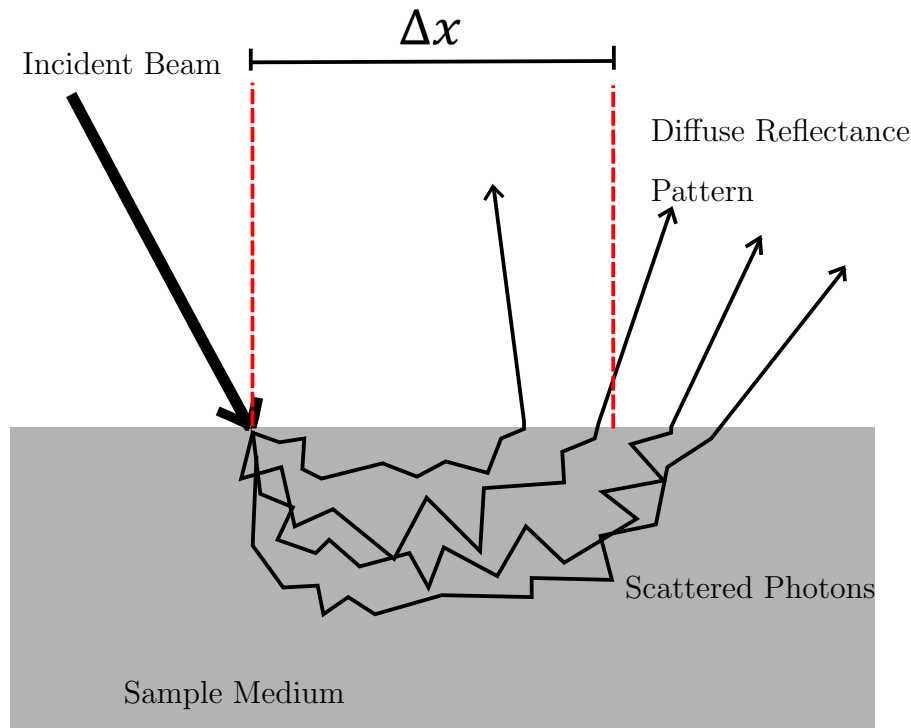


Figure 4.17: Diagram of the scattering of photons in the sample medium and the resulting diffuse reflectance pattern.

Using this assumption, we can rearrange equation 4.1 to get an equation for μ'_s :

$$\mu'_s = \frac{\sin \alpha_i}{n_{water} \Delta x} - 0.35\mu_a \quad (4.2)$$

The experiment that Lai, Wu, and Wang perform involves an incident laser beam at an angle of $\alpha_i = 37.9$ degrees to their phantom sample with a CCD camera above the phantom

to image the diffuse reflectance pattern. However, in order for this relationship to work, the incident beam on the sample must be collimated light and so we set up a series of lenses and pin hole irises to produce this beam from our diode laser. A diagram of our setup for this experiment can be seen in figure 4.18 where a pinhole iris and a 60mm spherical lens have been added to our focusing optics that we used to focus the diode laser down to a point. Another pinhole is then added to occlude a large portion of the beam so that the incident ray is narrow and we can better see the distinction between the reflection of the incident beam and the diffuse reflection pattern.

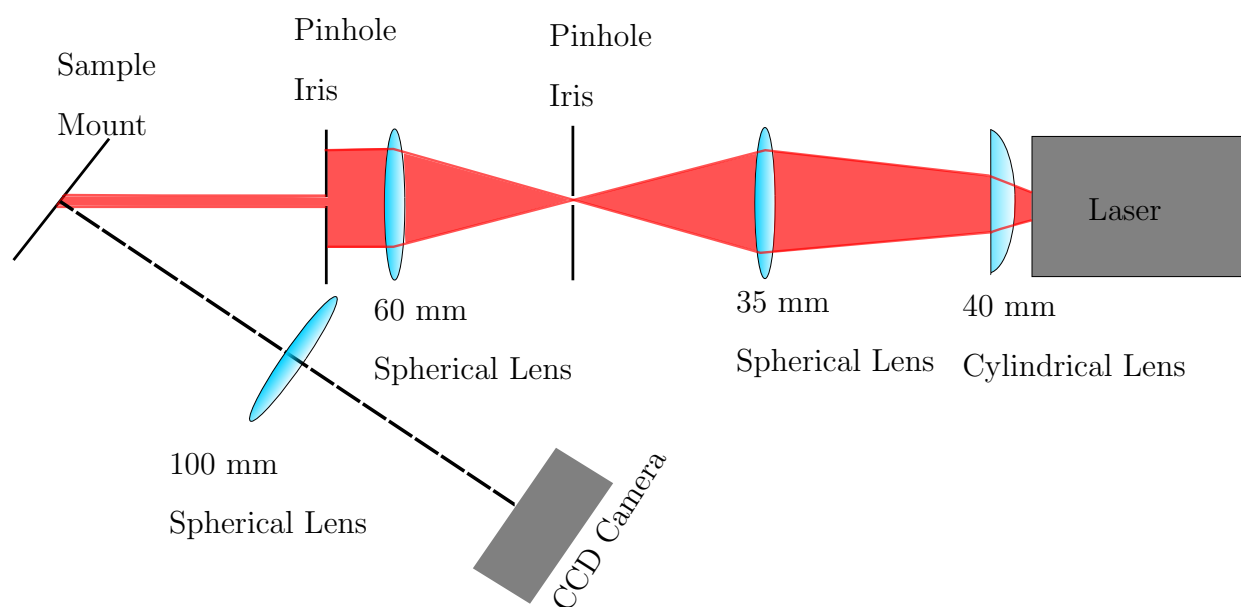


Figure 4.18: Diagram of the diffuse reflectance experiment to determine the reduced scattering coefficient.

The sample was then mounted at 37.9 degrees to the incident beam and another 100 mm spherical lens was used to focus the light coming from the surface of the phantom sample onto the CCD of our camera. The resulting image of the diffuse reflectance pattern from sample with just 5% (volume/volume) intralipid and no silica can be seen in figure 4.19. In this image we can see a large circle of light with a smaller brighter circle to the right of this circle. The large circle is the diffuse reflectance pattern and the small circle is incident light that has been reflected directly from the surface of the phantom. If we take a cross-section of this plot such that we get a profile of both distributions, seen in figure 4.20. Fitting Gaussian

distributions to this curve for each peak we can find the center of each of the circles, and finding the difference of these two centers we calculate Δx for the intralipid only phantom to be 0.0546 ± 0.014 cm. Using equation 4.2, we can therefore find that $\mu'_s = 8.43 \pm 3$ cm^{-1} for a phantom made with only intralipid and gelatin. Switching out the sample for the phantom with both 2% (mass/volume) silica and 5% (volume/volume) intralipid we got the resulting image in figure 4.21.

The reflection from the incident beam is slightly higher in this image due to slight imperfections in the surface of the phantom but you can still see the smaller circle to the top right of the diffusion pattern. Again, taking a cross-section of this image and fitting gaussian curves to each profile we can measure $\Delta x = 0.0555 \pm 0.014$ cm and find that $\mu'_s = 8.29 \pm 3$ cm^{-1} .

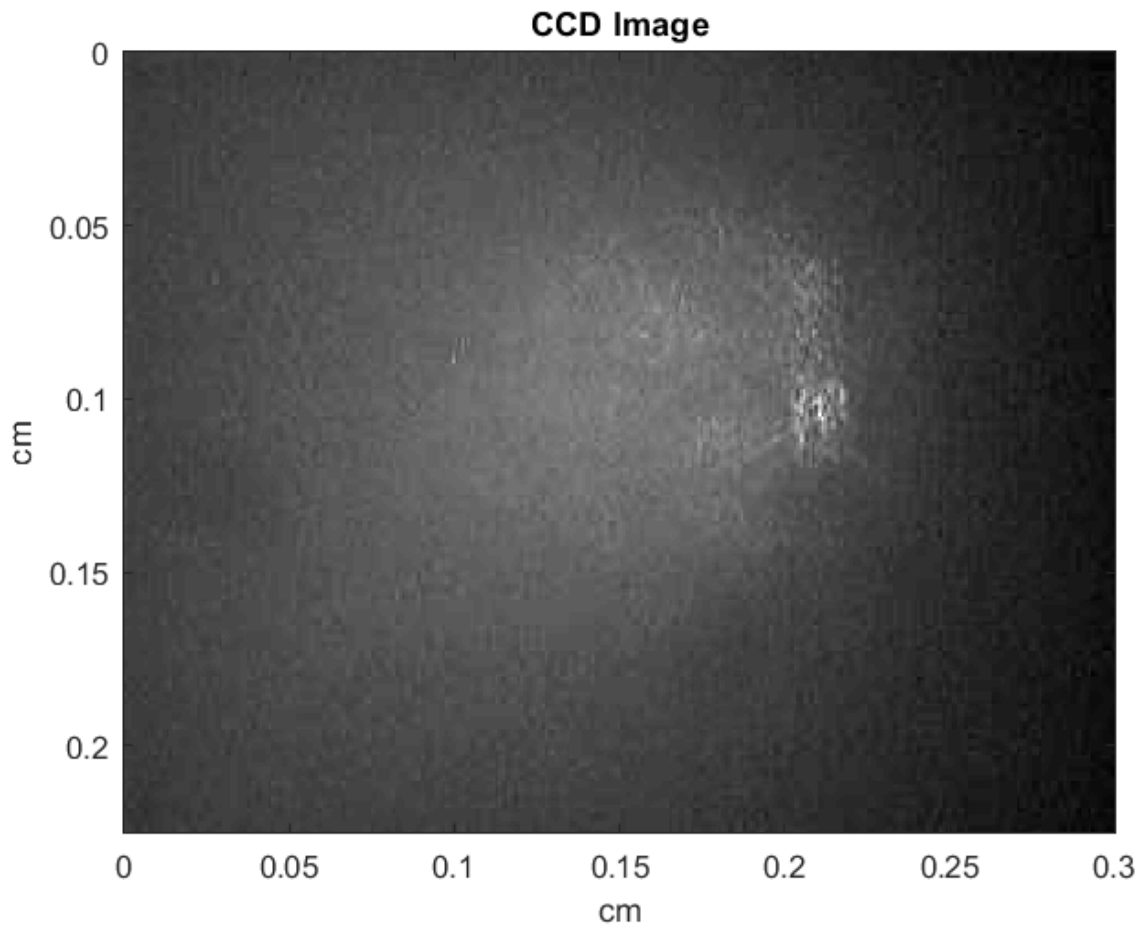


Figure 4.19: Results of the diffuse reflectance experiment to determine the reduced scattering coefficient of the phantom with intralipid and no silica.

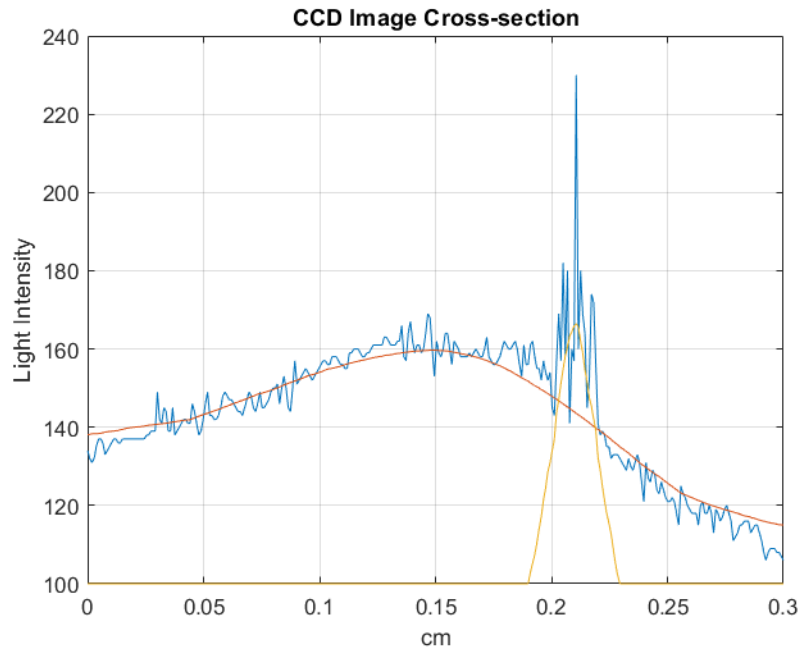


Figure 4.20: Cross-section of the results of the diffuse reflectance experiment to determine the reduced scattering coefficient of the phantom with intralipid and no silica.

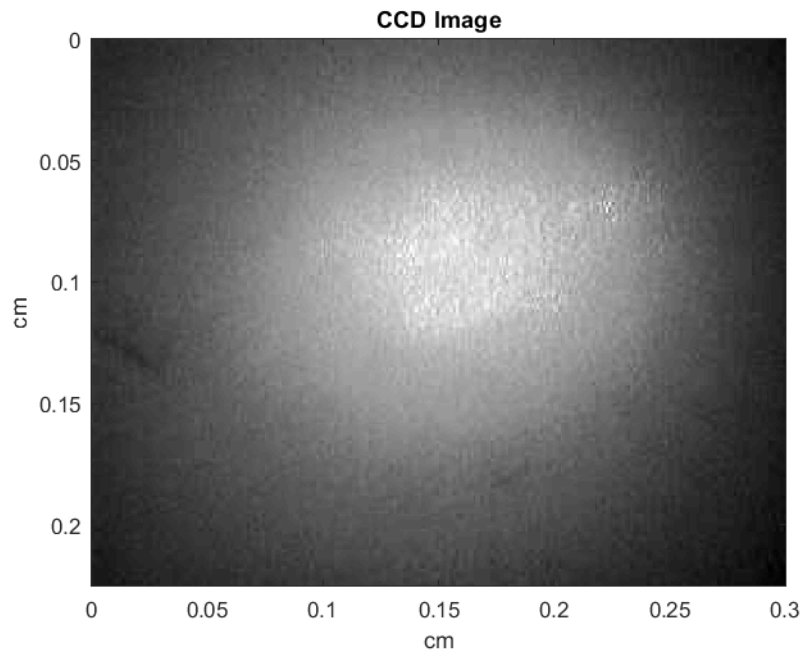


Figure 4.21: Results of the diffuse reflectance experiment to determine the reduced scattering coefficient of the phantom with intralipid and silica.

Our goal was to create a phantom with a reduced scattering coefficient of 10 cm^{-1} and if

we compare this to the range of values for each phantom, we see that both phantoms were consistent with a reduced scattering coefficient of 10 cm^{-1} . This tells us not only that we have the correct proportion of intralipid in our tissue phantom but also that the addition of the silica particles have little to negligible effect on the reduced scattering coefficient of the medium. Therefore, for the purpose of photoacoustic images we find the tissue phantom to be a satisfactory replacement for brain tissue given the literature.

Chapter 5

Handheld 3D Photoacoustic Imaging

Now that we have a tissue phantom that we can use to test our photoacoustic images in more realistic imaging targets, we must now integrate the photoacoustic system into the existing ultrasound endoscope. We can do this using fiber optic cables to direct the light from the diode bar laser to the tip of the endoscope and have the target illuminated co-linearly with the ultrasound transducer instead of illuminating targets from the side as in the images obtained in chapter 3. In order to do this we must first choose appropriate fiber optic cables and the number that will be used, design a series of lenses to couple the bundled fiber optic cables, and finally fabricate the bundle and attach the cables to the ultrasound transducer.

5.1 Fiber Optic Cables and Materials

Optical fibers are glass or plastic optical waveguides with circular cross-section which use the principle of total internal reflection to direct light along the fiber, allowing light to propagate wherever we wish.

Total internal reflection is a phenomenon in which light is reflected at the interface of two media with different indices of refraction when the incident light at a shallow angle relative to the surface interface. Snell's Law, tells us that when light in a medium with refractive index n_1 and an incident angle of θ_1 relative to the surface normal reaches a surface interface of a medium with an index of refraction n_2 the resulting refracted light has an angle θ_2 according to the following equation:

$$n_1 \cdot \sin \theta_1 = n_2 \cdot \sin \theta_2 \quad (5.1)$$

When $n_1 < n_2$ the light bends toward the normal with $\theta_1 > \theta_2$, but when $n_1 > n_2$, the light bends away from the normal with $\theta_1 > \theta_2$ with a maximum θ_2 of 90° . The incident angle, θ_1 , that causes $\theta_2 = 90^\circ$ is called the critical angle, θ_c , which can be found using the following equation for each interface.

$$\theta_c = \sin^{-1} \left(\frac{n_2}{n_1} \right) \quad (5.2)$$

If the angle of incidence is greater than the critical angle we get total internal reflection in which the light is reflected at the same angle as the incident angle according to the law of reflection. We therefore see that if $\theta_1 > \theta_c$ we get total internal reflection, if $\theta_1 < \theta_c$ we get refraction according to Snell's law, and if $\theta_1 = \theta_c$ the light travels along the surface of the interface.

In fiber optic cables, rays travel down the cables by successive total internal reflections along the length of the cable as in figure 5.1. Here, the two media with different refractive indices are known as the core and the cladding with the core having the higher refractive index n_1 such that the light is confined in the core. In order for the incident light entering the fibers to undergo total internal reflection, the beams must enter at angle in the acceptance zone where the angles are all greater than the critical angle with respect to the normal. Incident light with a smaller angle than this will pass through the cladding into the coating where light is absorbed to stop light from getting to adjacent fibers. This means that depending on the angle of the incident light from the laser, there may be some loss of light when coupling which we aim to minimize. The light collection ability of a fiber is often described by the numerical aperture of the fiber optic cables, NA, which is given by $NA = \sqrt{n_{core}^2 - n_{cladding}^2}$ where the acceptance angle can be calculated by $\theta_a \approx \sin^{-1}(NA)$.

There are three main types of fiber optic cables used, single-mode glass, multi-mode glass, and plastic optical fiber. When choosing the fiber to use for our endoscope, we mainly considered the glass fibers due to the fact that we wanted to achieve a high ratio of core area to cladding area in order to couple a large fraction of the incident light, and the available plastic fibers had low ratios compared to the glass fibers. Also, some fabrication steps had initially involved heating epoxies and there was risk of melting during those as well. We therefore considered single-mode and multi-mode glass fibers for our purposes. Single-mode fibers allow a single ray to propagate through and have a core radius that is less than the wavelength of the light source used for them. This is not an ideal fiber for our laser due to the large amount of divergence of our laser beam and also the rectangular shape of the image. It would be impossible to couple light from a multi-mode source like our laser into a single-mode fiber and we would not get more than a fraction of a percent coupling efficiency.

Multi-mode fibers allow for wider acceptance angles so much more light would get from the laser to the endoscope tip.

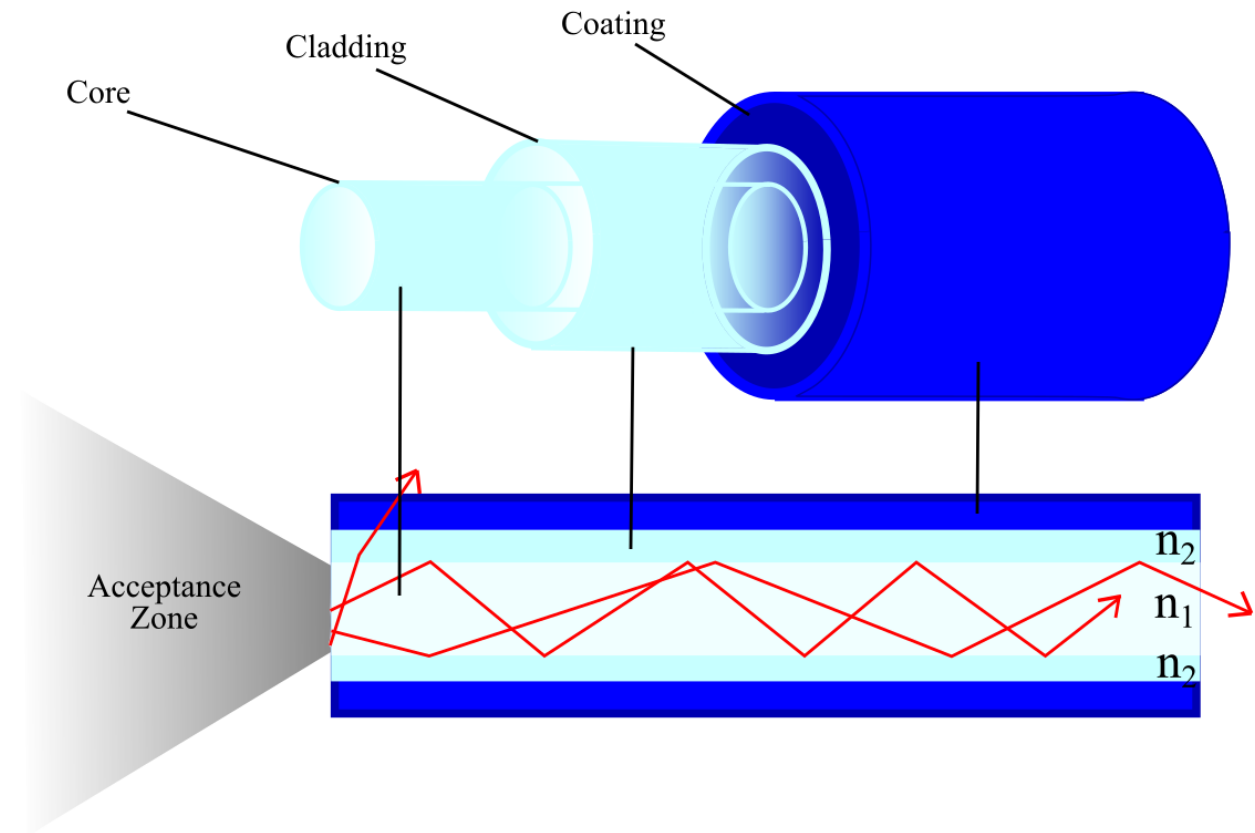


Figure 5.1: Fiber optic cable layers and light propagation via total internal reflection.

Incidental losses come from imperfect coupling due to poor alignment and poor cleavage of fiber ends which cause light to be lost due to not meeting the total internal reflection requirements. Incidental losses can also occur due to too much bending in the fibers which causes the light to hit bent sections at small angles to the normal and so total internal reflection is lost and light leaks out the of the fiber.

The fiber we chose to use is a glass multimode fiber with 200 μm diameter silica core with a 225 μm hard polymer cladding (FP200URT, Thorlabs, Inc. Newton, NJ, USA). Since in this class of fiber, the core is made of stiff glass, there is an important design tradeoff between core diameter and flexibility. A larger ratio of core to cladding diameter is beneficial to coupling efficiency but makes the illumination source stiffer. After experimenting with several fibers, we found that the 200/225 fiber offered acceptable flexibility along with high

coupling efficiency. These fibers have a numerical aperture of 0.50, transmit wavelengths in the range of 300 - 1200 nm, have an operating temperature of -40 to 150°C, maximum attenuation of 12dB/km at a wavelength of 810nm, and a bend radius of 8mm. The numerical aperture gives the acceptance angle $\theta_a = \sin^{-1}(0.5) = 30^\circ$, meaning light entering the fiber must be at an angle of less than 30° to be accepted. With the endoscope tip being 3mm by 3mm, mathematically, 13 fibers should be able to fit on each side, however, practically, it was challenging to fit these on the endoscope in preliminary tests so 9 were used on the front and back and 6 were used on each side due to the difficulty of arranging them on the sides. This preliminary work involved creating an initial prototype of the endoscope probe with attached fiber optic cables to provide illumination at the tip of the probe without interfering with the overall operation of the endoscope. A blank 3D printed model of the endoscope without functional ultrasound components was used for this initial design where a UV epoxy was found to be the best epoxy to use due to the ~ 1 min curing time eliminating the need for clamping the fibers down during curing. A total of 30 fibers were bundled together and an illumination pattern in which there was solid illumination which can be seen in figure 5.3.

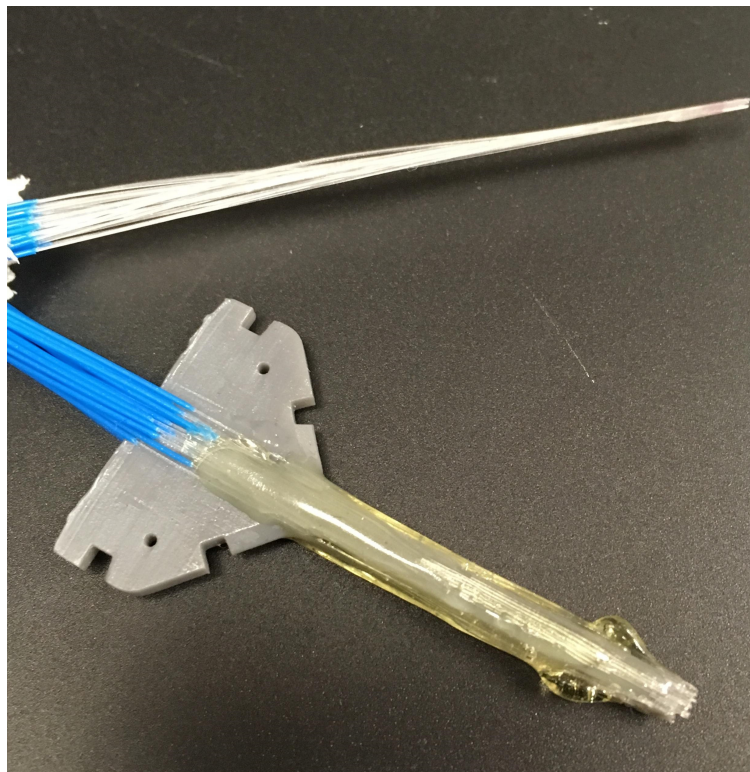


Figure 5.2: Photoacoustic fiber optic cables fixed to the ultrasound transducer plastic support using UV epoxy.



Figure 5.3: Illumination pattern at 12mm away from the endoscope tip.

In order to decide on the stacking of the 30 fibers at the bundled end, we could decide between 1x30, 2x15, 3x10, and 5x6 arrangements. We decided to bundle them 3 by 10 as in the image below, figure 5.4, due to this being the closest to the rectangular shape of the laser emission area and would minimize lens corrections to focus it into the correct shape to couple. Given the limited space of integrating with the endoscope we wish to minimize the optical path length. A staggered geometry would have been ideal over this stacked geometry to minimize dead space but due to it being difficult to control the staggered or stacked geometry during fabrication, we assume the worst case scenario of the stacked geometry occurred.

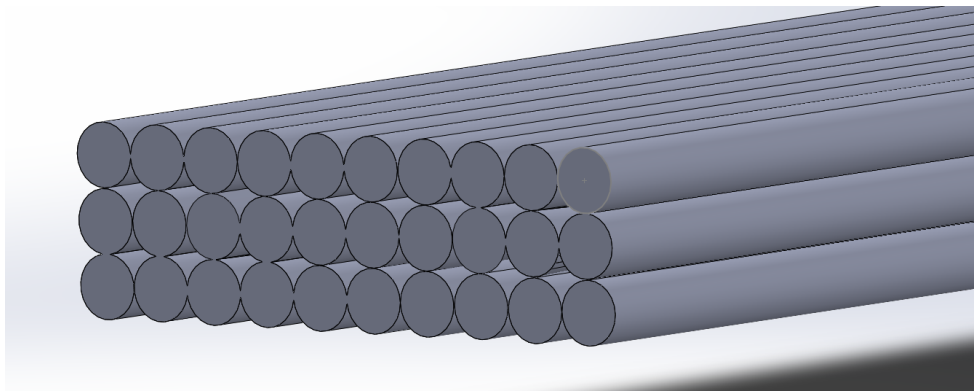


Figure 5.4: A model of the ideal fiber bundle for coupling to the diode laser.

With the fiber bundle determined, a lens system was then designed to focus and conform the laser light to best couple with the fiber bundle and minimize the loss of light delivered

to the endoscope tip.

5.2 Optical Coupling

The 808nm diode laser produces a rectangular image which can be seen in figure 5.5 below. In order to provide light to the endoscope via optical fibers, a compact system for coupling the laser to the optical fibers must be designed that minimizes the incidental losses due to coupling. This coupling system must also reduce any sort of strain or bending on the optical fibers past their maximum bend radius of 8mm so that light loss or fiber breaking does not occur. Finally, the system should capture as much light as possible from the laser image and transmit this light effectively to the fibers with minimal loss. Simply directing the laser on the fiber bundle would result in the loss of nearly all light due to the fact that the light output from the laser has initial dimensions of 2.3mm by 5mm with an area of 11.5 mm^2 and the fiber bundle has dimensions by 0.675mm by 2.25mm with an area of 1.5 mm^2 . This order of magnitude difference in area would cause 87% of the light to be lost if we coupled the fiber bundle straight from the laser and this even ignores the fact that there is a significant banding of the illumination pattern that can be seen in the near field image as in figure 5.5 which would result in further losses. Apart from that, the astigmatism would mean that the light could only be in focus for one of the two directions at the plane of the fiber ends. Therefore, a coupling system that consists of a lensing system which would focus the light and give the same dimensions as the fiber bundle as well as correct the astigmatism was necessary in order direct more light on the fiber bundle.

The divergence of the laser beam along the horizontal, slow axis, was 6.04° and along the vertical, slow axis, was 0.83° as in figure 5.6. This divergence also means that as we move further from the laser the gaps in the illumination we see in figure 5.5 will go away as the beams defocus out and add together. We needed to first use a convex cylindrical lens to reduce the divergence in the horizontal direction and also correct the astigmatism by moving the horizontal focus to the same location as the vertical focus. In doing this we can also chose a lens that will produce the dimensions we need in the focused image ($\sim 0.675 \text{ mm}$ by 2.25 mm).

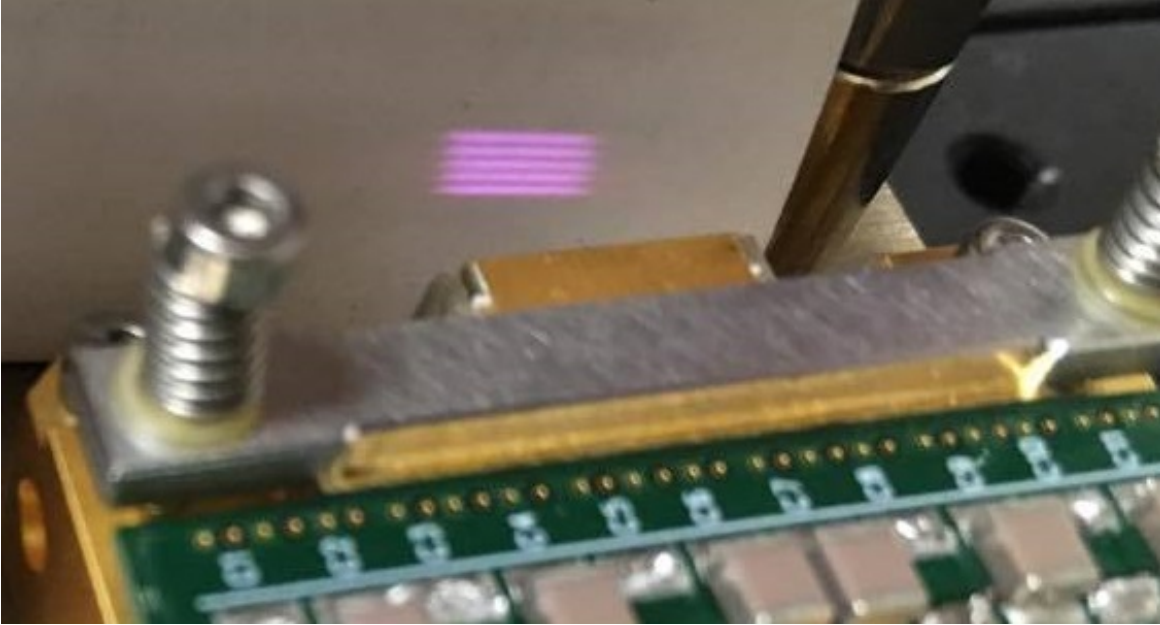


Figure 5.5: Image of the diode laser light in the near field.

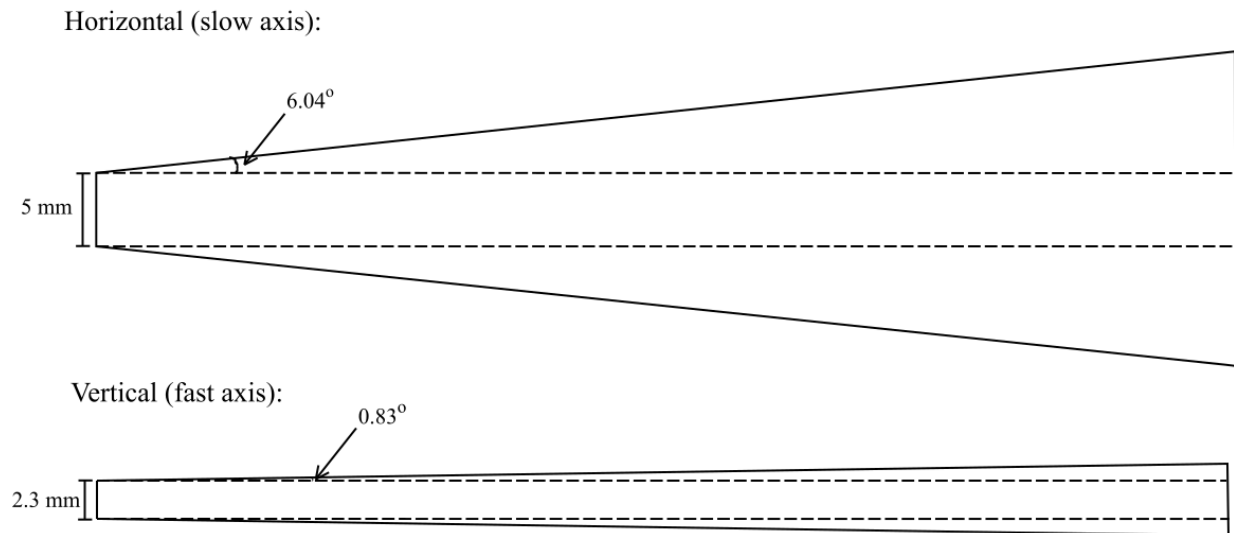


Figure 5.6: Divergence of the laser in the horizontal direction (slow axis) at an angle of 6.04° and the divergence in the vertical direction (fast axis) at an angle of 0.83° .

The collimating lens was a 40 mm cylindrical lens (Thorlabs LJ1125L-B Plano-Convex Cylindrical Lens, Antireflection Coating: 650-1050 nm) placed 17 mm from the front of the laser which mimics an effective point source at the focal point 40 mm from the lens. This corrects the astigmatism by moving the focus in the horizontal direction to the same spot

as the focus in the vertical direction which also reduces the 6° divergence in the horizontal direction. We could collimate the vertical divergence as well by placing another cylindrical lens oriented 90° to the first, however, with such a small divergence this extra lens would only increase the optical path length and not make a large improvement in the final focused image. Next, a 35 mm spherical lens (Thorlabs AC254-035-C-ML Achromatic Doublet Antireflection Coating: 1050-1700 nm) was placed such that both beams were in focus creating our final focused image at 35mm from the spherical lens.

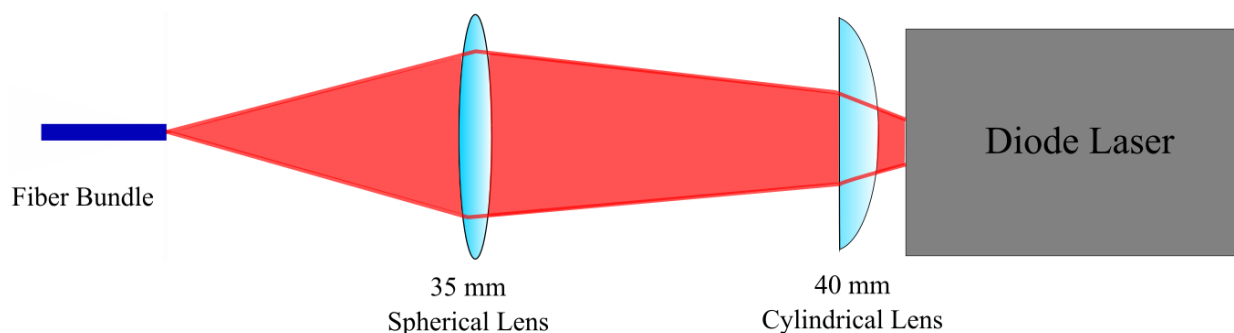


Figure 5.7: Diagram of the coupling optics for coupling the diode laser to the fiber bundle.

The resulting focus was then imaged using a CCD camera giving the image in figure 5.8. The dimensions of this focused image was 0.5mm by 2.0 mm which was a bit smaller than the 0.675 mm by 2.25 mm we wanted but this had a much stronger agreement than the initial laser illumination would have been. If we look at the red circles overlayed on figure 5.8, these represent the cross-section of the fiber bundle and how it would align with the focused beam. We placed this coupling system beside the ultrasound machine as a separate unit where the fiber bundle would join the ultrasound cable after coupling as in figure 5.9.

Measurements of coupling efficiency were taken with the fiber bundle with the supplied laser power reduced to 40 V from 200 V to protect the optical power meter. The optical power at the focus was found to be 28.2 mW and the optical power at the fiber distal end was 9.6 mW giving 34% coupling efficiency. The illumination pattern at the end of the endoscope was found to have a solid illumination pattern for 15 mm past the endoscope tip in air. An image of this is seen in figure 5.3.

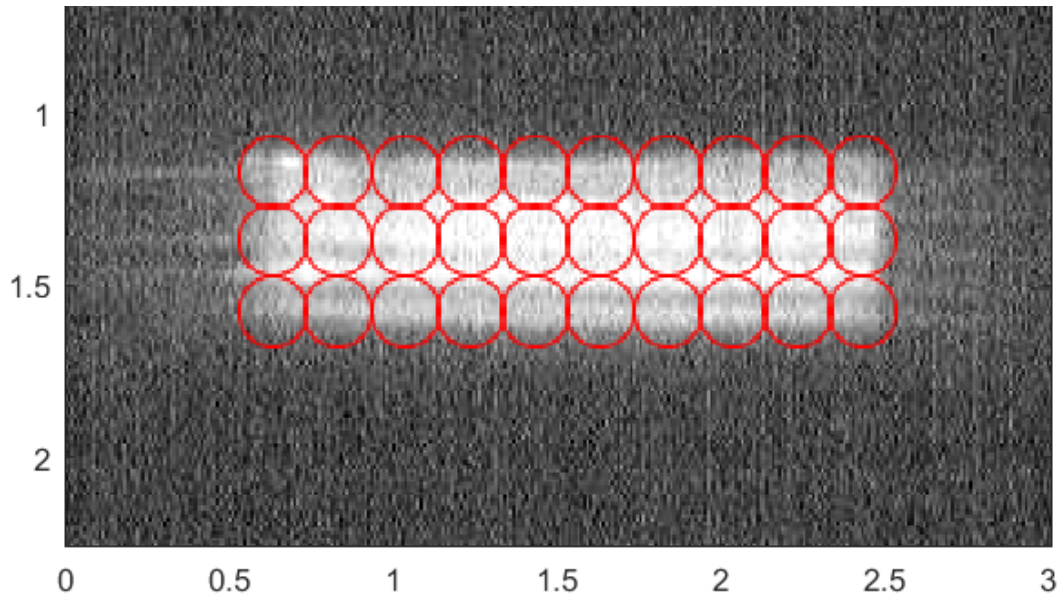


Figure 5.8: The laser image at the focus. The red circles overlaid on the image represent the fiber bundle fiber bundle cross-section.

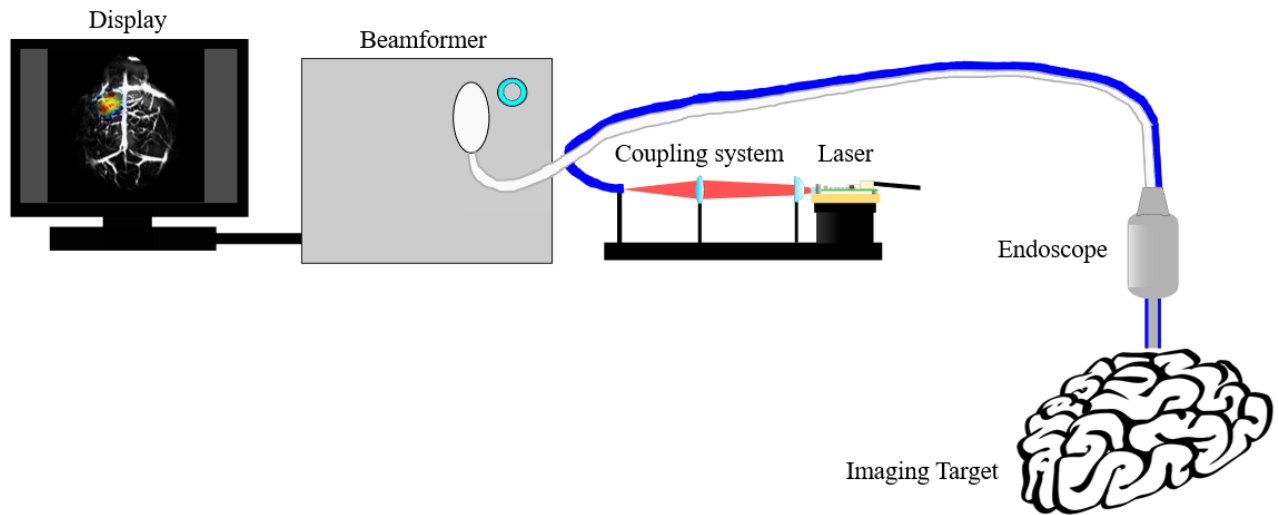


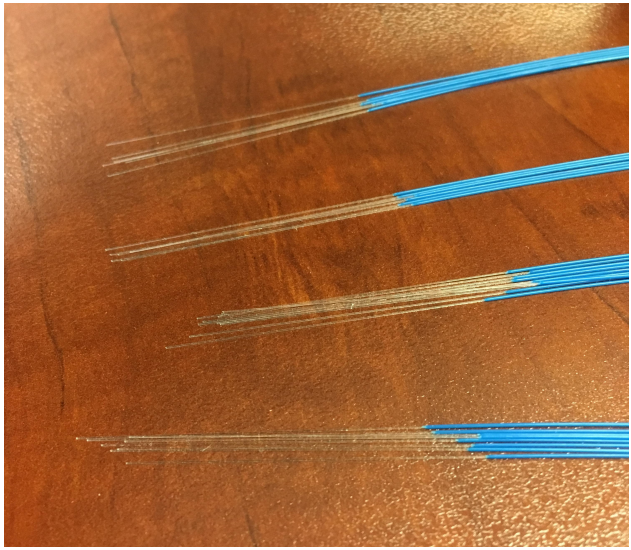
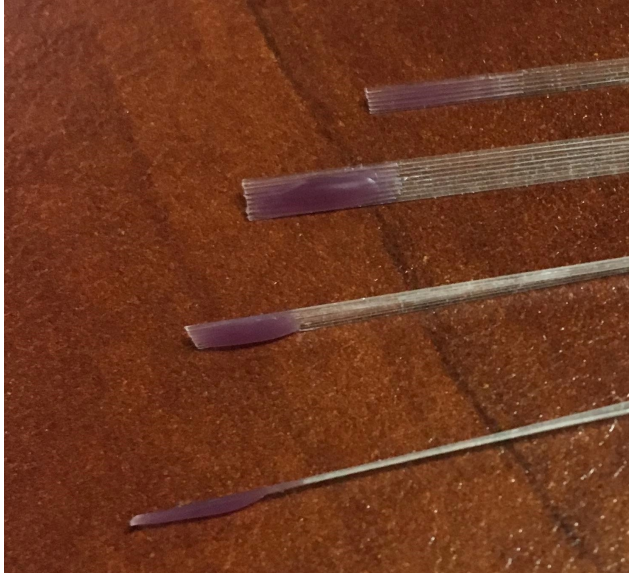
Figure 5.9: Diagram of the system setup including the coupling system and laser.

5.3 Fabrication Process for Fibers

With light coupled into the distal end of the fiber bundle, the proximal end could deliver that light to the sample. In this section we describe a set of manufacturing techniques for

fabricating four bundles with 6 or 9 fibers each and attaching them to the four sides of an endoscopic ultrasound transducer [1].

5.3.1 Fabrication of Transducer End

Fabrication Step	Image of Fabrication Step
<p>1. Thirty, 1.5 m long fibers were cut and the ends of the 30 fibers were stripped up to 60 mm using a fiber stripping tool (T12S21, Thorlabs, Inc. Newton, NJ, USA). After stripping the ends, the fibers were cleaved using an Optical Fiber Cleaver With A Single Fiber Adapter For 250 μm To 900 μm Fibers (TC-80 Fiber Optics For Sale Co., Pleasanton, CA, USA).</p>	
<p>2. The fibers were then arranged in two groups of 6 and two groups of 9 fibers. These were flattened as best using the flat edge of a razor blade and fixed together using hot wax heated to 60°C placed on one side of the fiber group and held in place until the wax cooled temporarily holding them together.</p>	



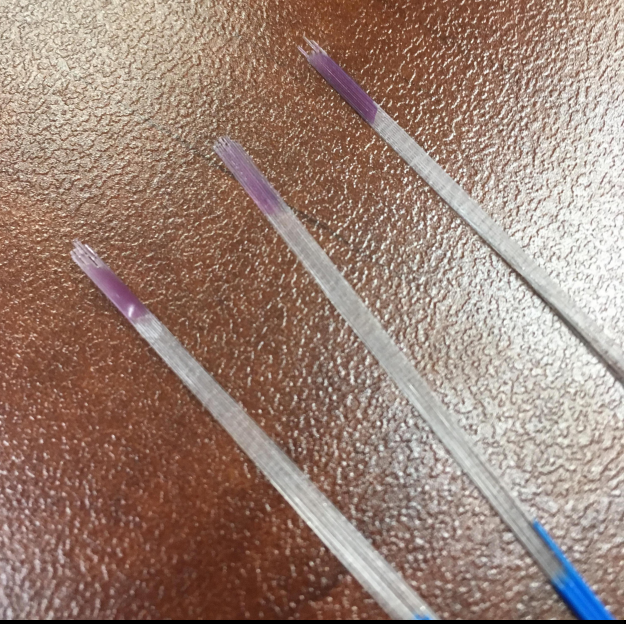
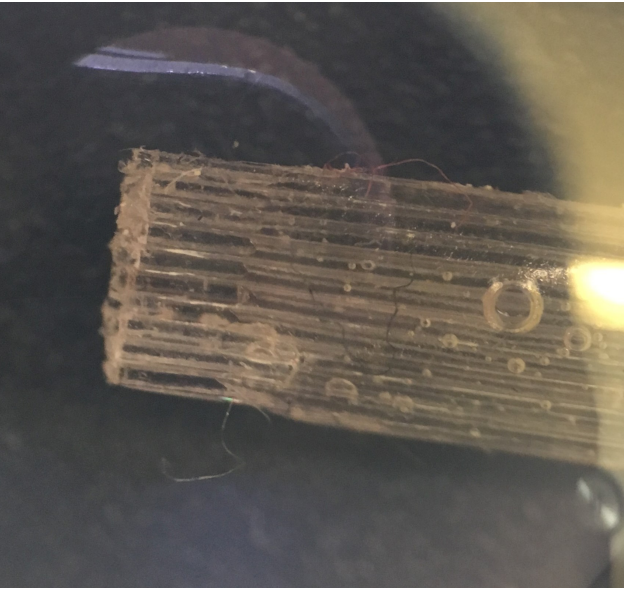

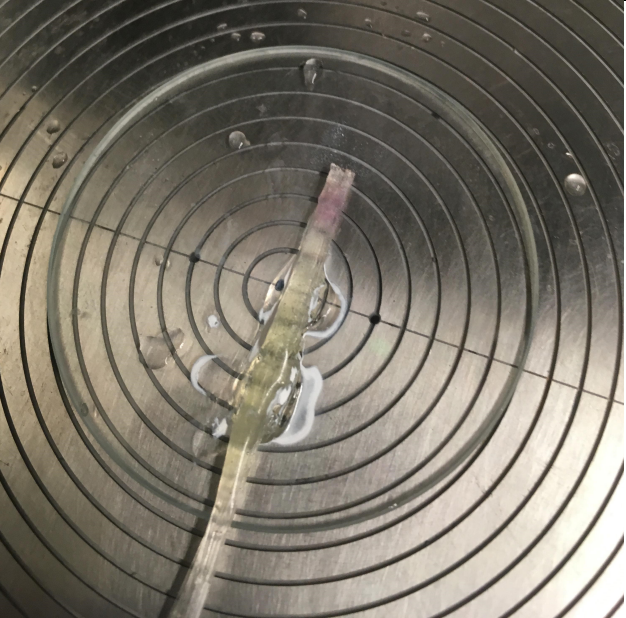
Fabrication Step	Image of Fabrication Step
<p>3. The fibers were then epoxied with the UV curing epoxy, Optical Adhesive for Bonding Glass to Plastic, 1 oz.(NOA68, Thorlabs, Inc. Newton, NJ, USA) which was cured using the LED UV Curing System (LED-200, Thorlabs, Inc. Newton, NJ, USA). These ends were now ready to be attached to the endoscope tip after the fiber bundle end if fabricated.</p>	

Table 5.1: Transducer End Fiber Fabrication Procedure

5.3.2 Fabrication of Fiber Bundle End

Fabrication Step	Image of Fabrication Step
<p>1. The distal ends of the fibers were again stripped to 60 mm using the same Thorlabs fiber stripper.</p>	

Fabrication Step	Image of Fabrication Step
<p>2. The fibers were then fixed into groups of 10 using wax on one side with the first group of fibers waxed on the opposite side as the other two groups to facilitate epoxying. Again, care was taken to completely flatten the fibers into a single line using the flat side of a razor blade.</p>	
<p>3. The first and second layers were epoxyed together using the UV curing epoxy and the UV light source while their wax sides were oriented outward so that they can bond as close together as possible. The wax was removed using acetone and more epoxy was applied to the outside to provide strength so that the fibers did not separate. The side that will bond to the last layer was left clean of epoxy and wax. The strands are really easy to separate at this stage so they were treated delicately until the final layer was epoxyed on.</p>	

Fabrication Step	Image of Fabrication Step
<p>4. The third layer of fibers was epoxied to the other two layers with the sides clear of epoxy and wax on the inside. The UV epoxy was then applied and cured using the UV light source and the remaining wax removed. A final thin layer was then applied to the entire outside surface to add strength during the cleaving process.</p>	
<p>5. The Bundle was then fixed to a glass slide, again using the UV curing epoxy at a few points along the fiber bundle until it was securely held in place. The glass slide will allow us to hold the bundle in place on the vacuum table of the dicing saw used to cleave the fibers but still allow the bundle to be removed afterwards.</p>	


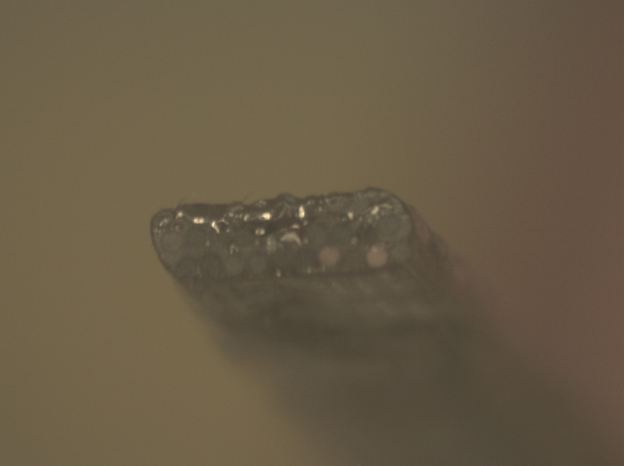
Fabrication Step	Image of Fabrication Step
<p>6. Using the Fully Automatic Dicing Saw (DAD3220, DISCO Hi-TEC America, Inc., San Jose, CA, USA), the glass slide was vacuumed to the movable vacuum plate with the fibers carefully wrapped around the plate and taped in place so that none of the moving parts would snag them and they were below the path of the saw. The fiber bundle was then cut across the tip so that the end was cleanly cleaved giving a good surface for coupling light.</p>	 <p>The image shows a large, circular, metallic vacuum plate mounted on a machine. A fiber bundle, consisting of many individual fibers, is wrapped around the plate in a spiral pattern. The fibers are held in place by small pieces of tape. The plate is positioned on a workbench, and the surrounding area is filled with various mechanical parts and tools, indicating a laboratory or manufacturing setting.</p>
<p>7. Finally, the bundle was removed from the glass slide by gently peeling the epoxy off of the slide with a razor blade by slow sliding the razor under the epoxy. The fibers should just pop off the slide and the complete fiber optic cables are ready to be attached to an endoscope.</p>	 <p>The image is a close-up shot of a fiber bundle being removed from a glass slide. The fibers are dark and appear to be breaking away from the slide. The background is a plain, light-colored surface, possibly a workbench or a cleanroom floor.</p>

Table 5.2: Fiber Bundle Fabrication Procedure

5.4 Fabrication of the Photoacoustic Endoscopic 40MHz 2D Array and 30MHz 3D Array Transducers

This approach was used to attach photoacoustic illumination fibers to two different ultrasound endoscopes, the 40MHz 2D ultrasound transducer and the 30MHz 3D ultrasound transducer. In this section we present the results of imaging with these two photoacoustic endoscopes, using the photoacoustic phantoms described in Chapter 4.

We decided to temporarily fix the fibers to the transducers using wax so that the fibers can easily be removed later and the probes can continue to be used. The results of this can be seen in figures 5.10 and 5.11 for the 2D and 3D probes respectively. During the fabrication process 6 fibers were broken in the 2D probe and 2 fibers were broken in the 3D probe.

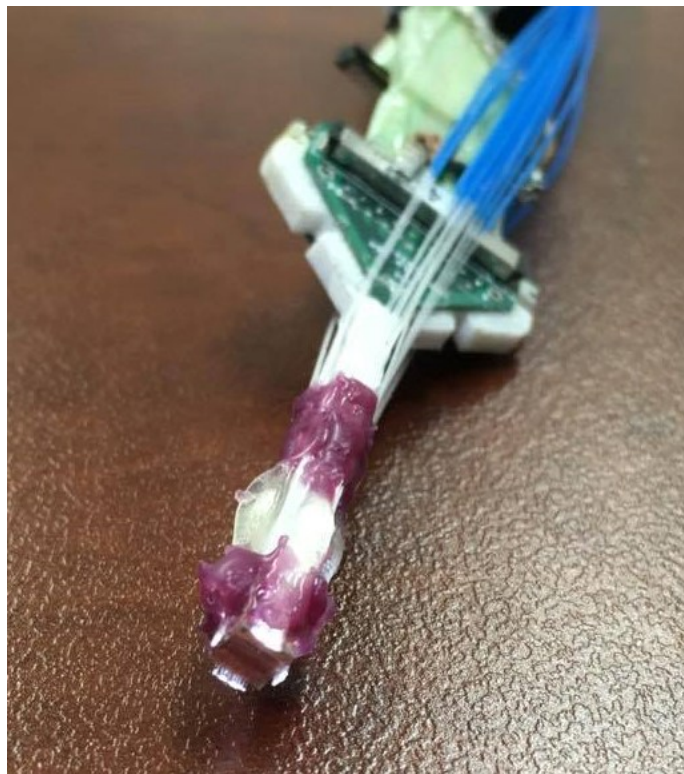


Figure 5.10: Photoacoustic fiber optic cables temporarily fixed to the 40 MHz 2D phased array ultrasound transducer using wax.



Figure 5.11: Photoacoustic fiber optic cables temporarily fixed to the 30 MHz 3D phased array ultrasound transducer using wax.

5.4.1 2D Ultrasound and Photoacoustic Imaging with Tissue Mimicking Phantom

Using the 2D 40 MHz photoacoustic probe whose fabrication was outlined in the previous section, an ultrasound image and a photoacoustic image were taken of the tissue mimicking phantom described in chapter 4. The system was set up as in figure 5.12 with the probe aimed at the tissue phantom hair target and ultrasound gel (EcoGel™ 200) as the sound conduction medium between the probe and the tissue phantom. The laser was setup to pulse at 1 kHz with a pulse width of 1 μ s as in the side illumination experiment in chapter 3.

First, an ultrasound image was taken of the hair target tissue phantom using the ultrasound systems existing software and firmware. The results of this acquisition can be seen in figure 5.13 below where two hair targets are visible as indicated by the red arrows. Since the hairs in the tissue phantom are spaced 2 mm apart both vertically and horizontally we should see three hair targets in the image but the third hair is difficult to see (the faint signal is indicated by the red circle) due to the speckle pattern in the ultrasound image which is

caused by the ultrasound backscattering of sound.

After the ultrasound image was captured, the system was reconfigured using the photoacoustic version of the firmware and software and a photoacoustic image was averaged and captured which can be seen in figure 5.14. In order for the photoacoustic image to appear above the noise floor, it was necessary to average for 10,000 averages which is 10 times more than were necessary for the side illumination experiments. Since the resulting signals were just above the noise floor we can also see in this image some electrical noise from the system appearing down the center of the image as well. Apart from the noise inherent to the system in this image we can see that there is no noise from ultrasound backscattering which was present in the ultrasound images. Another change that was made was that the beamformed enveloped data was multiplied by $e^{0.006x}$ in order to increase the gain for the deeper hair targets so that the third target could be visible while minimizing the increase in the noise in the region. Overall, this process required 50 minutes to acquire 10,000 averages and the post processing of images was labour intensive. The photoacoustic image has an increased contrast of 42.3 dB compared to the ultrasound contrast of 22.8dB for the hair at approximately 3.5 mm depth.

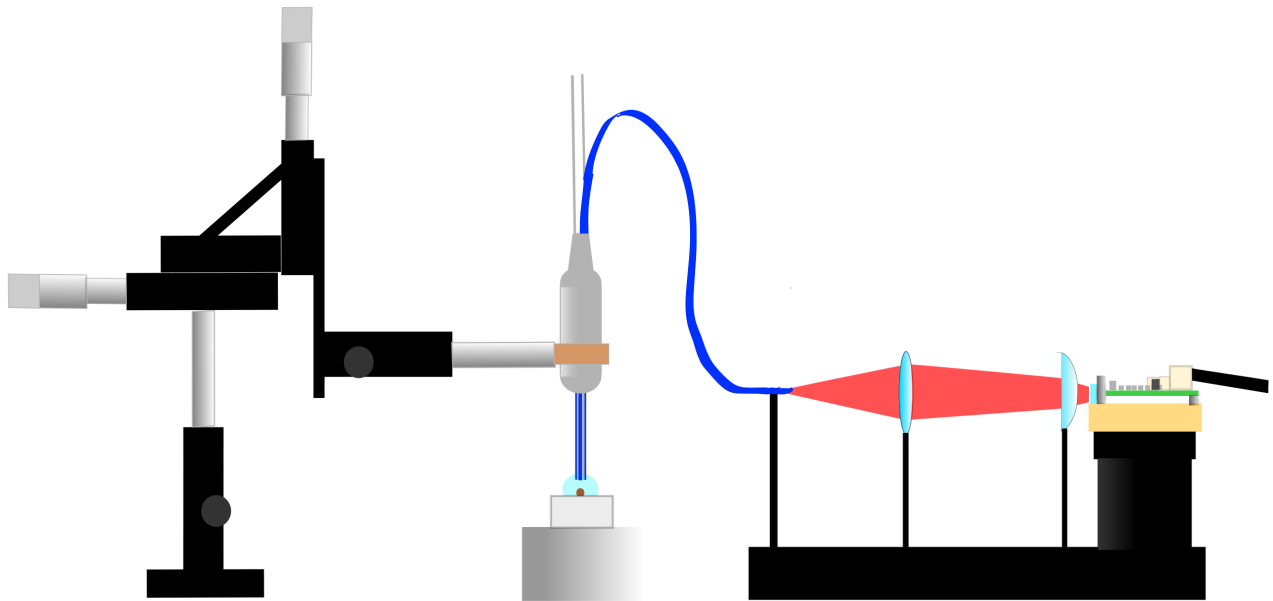


Figure 5.12: Setup of the fabricated photoacoustic probe with a tissue phantom hair target and coupled fiber optics..

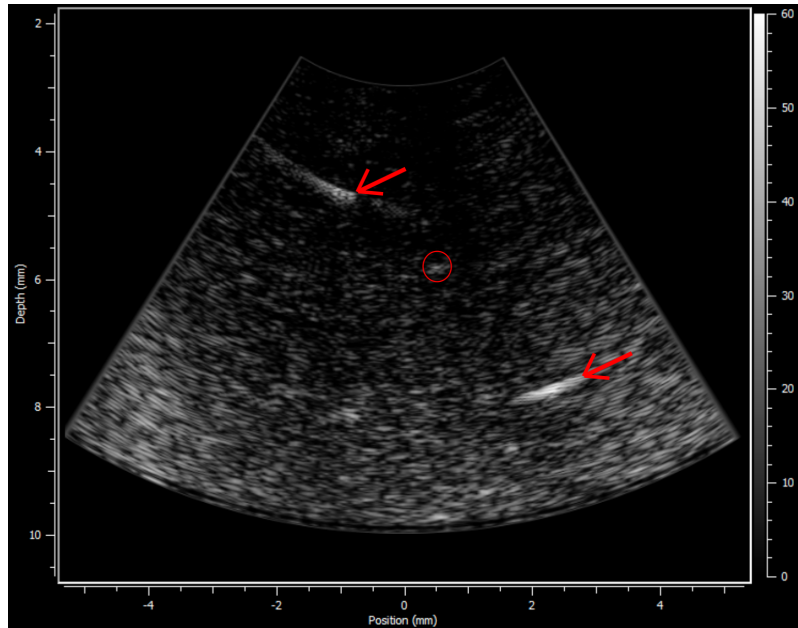


Figure 5.13: Ultrasound imaging results for hair targets in the tissue phantom using the 40 MHz 2D Endoscope. This image should ideally have 3 circular images from each of the hair targets located at the red markers.

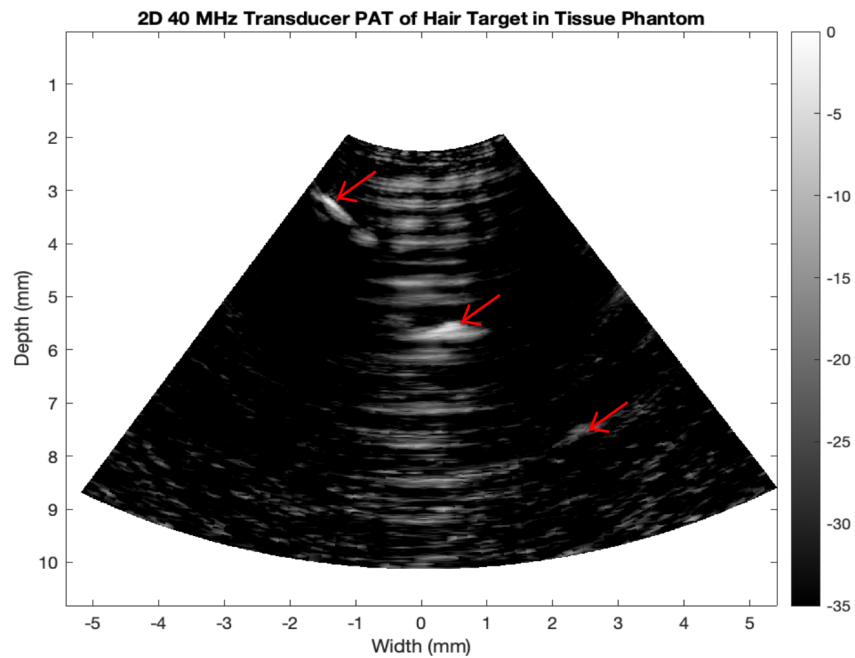


Figure 5.14: Photoacoustic imaging results for hair targets in the tissue phantom using the 40 MHz 2D Endoscope. This image should ideally have 3 circular images from each of the hair targets which can be seen at the red markers.

5.5 Photoacoustic 3D Imaging

5.5.1 3D Photoacoustic Imaging with Side illumination

After acquiring images of the tissue mimicking phantom with the 2D photoacoustic probe, we began to adapt the 3D ultrasound firmware in a similar way as the 2D ultrasound firmware and used the same acquisition software as with the 2D experiments. The delay between the laser trigger and when the system records the received sound was increased from $2 \mu\text{s}$ to $3 \mu\text{s}$ in order to avoid capturing some of the large noise from the switching of the bias boards the 3D ultrasound system uses to encode both the sent and received pulses.

We began by repeating the side illumination experiment from chapter 3 but instead used the 3D ultrasound probe to receive the photoacoustic signal. The imaging target was a single hair mounted in a tank of water with the focused laser light directly incident on the hair target as in the previous side illumination experiment in figure 3.7. The beamformed results of this can be seen in figure 5.15 below. The same beamforming code was used for both probes with small changes to account for the timing differences applied. The signal beamformed was unfocused in the elevation direction.

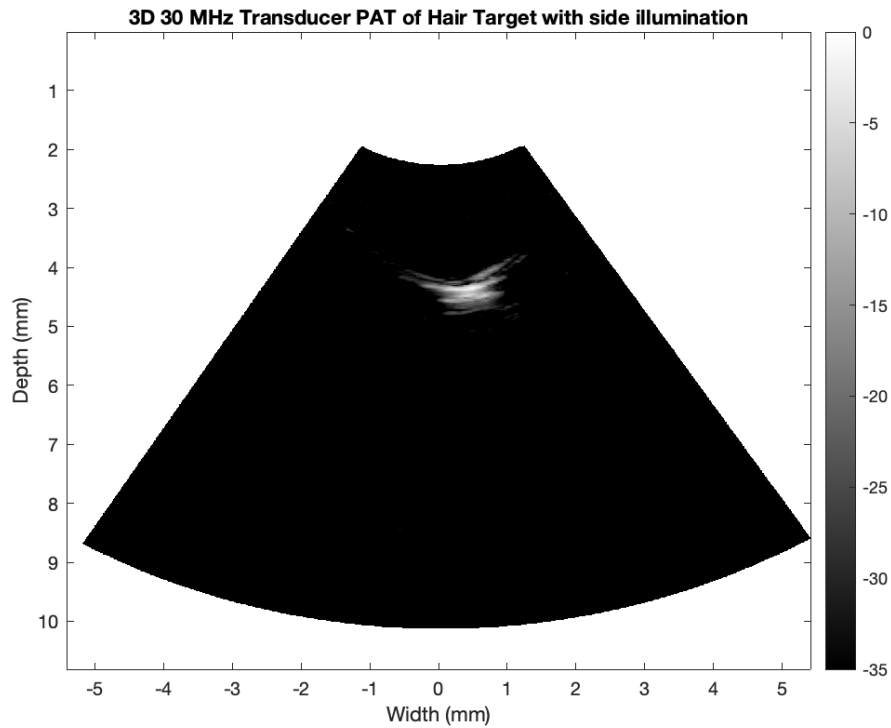


Figure 5.15: 3D Photoacoustic image of the hair target with the diode bar laser illuminating from the side.

A very large noise was present in the raw data which initially obscured the photoacoustic image from being visible and in order to remove this noise caused by the bias board switching, the first 250 data points were cropped out and replaced with background noise data from the end of the data acquisition where there was no signal. This noise was not consistent between acquisitions, nor was it consistent between different bias configurations and so could not be cancelled out by subtraction with a frame in which no light was incident on the hair target.

5.5.2 3D Photoacoustic Imaging with coupled fiber optics

After successfully imaging with side illumination, the 3D photoacoustic probe was constructed as described in sections 5.3 and 5.4 and the same experiment as in figure 5.12. The firmware and software remained the same as in the side illumination experiment and 10,000 averages were taken to acquire a 3D photoacoustic image with the endoscope as with the 2D endoscopic experiment. However, we were not able to produce an image with visible photoacoustic signals. These results can be seen in figure 5.16 in which we only see noise from the system. Again, the bias switching noise was present in the raw data but even after removing this large noise no image of hair targets could be seen.

We suspected that this may be due to the attenuation of the receive signal from the hair target to the transducer face and so we made a hair target which only contained gelatin and intralipid. This would allow us to match the scattering properties light in tissue and allow light to reach the hair target but would have no attenuation due to acoustic backscattering on route to the transducer. The fabrication of this phantom followed the fabrication steps from section 4.2 but would skip adding the 2% (mass/volume) silica powder to the gelatin powder in step 1. Using this intralipid and gelatin hair target, the same experiment was performed and the image in figure 5.17 was obtained. 10,000 averages were required to produce this image but there are three clear hair targets in the image as expected. The contrast of this image was found to be 44.2 dB which is similar to the contrast with the 2D photoacoustic endoscope images with a contrast of 42.3 dB.

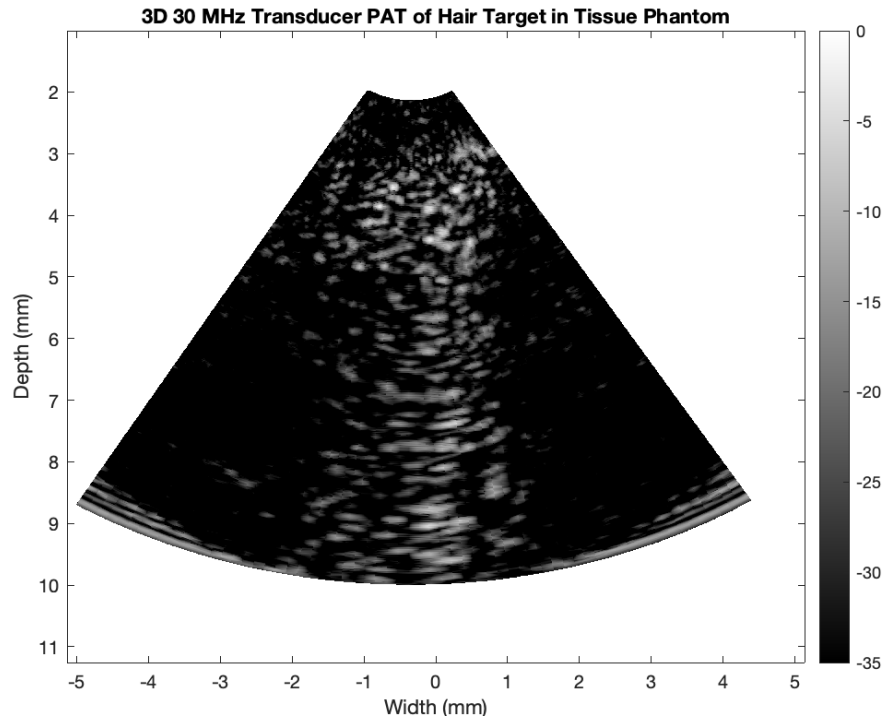


Figure 5.16: 3D Photoacoustic image of the hair target in tissue mimicking phantom using the final endoscope.

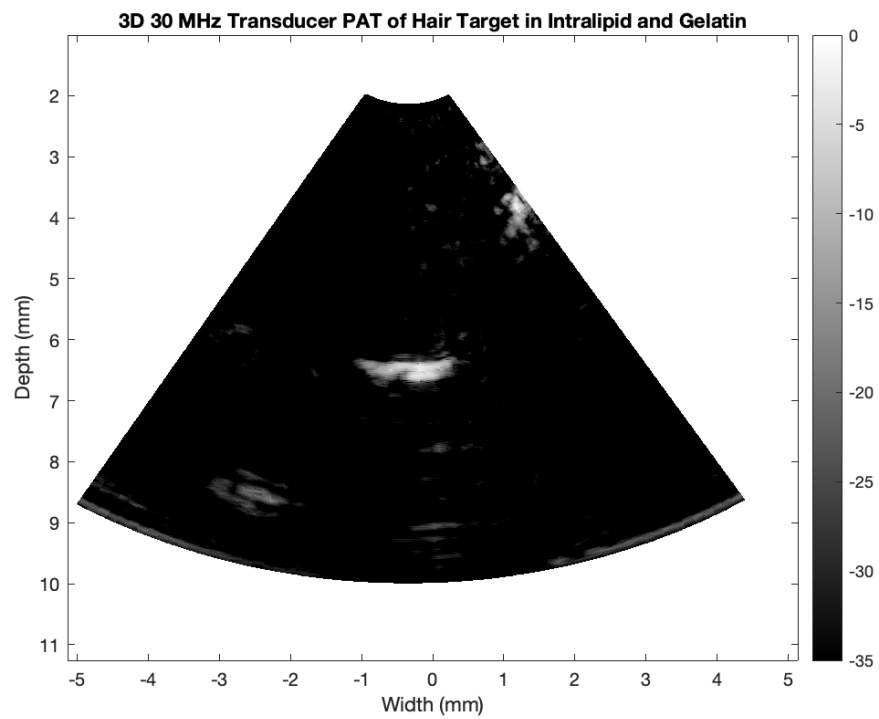


Figure 5.17: 3D Photoacoustic image of the hair target in Intralipid and Gelatin phantom using the final endoscope.

If we compare the channel data between the tissue mimicking phantom and the intralipid and gelatin medium, we can see in figure 5.18 that the amplitude of the photoacoustic signal from the phantom containing only intralipid and gelatin is above the level of the background speckle produced by the photoacoustic signal. The gray regions indicate the regions in the signal in which we should see photoacoustic peaks from each hair target. However, in this image the photoacoustic signal for the tissue phantom with silica is not visible due to being too low to detect above the level of speckle.

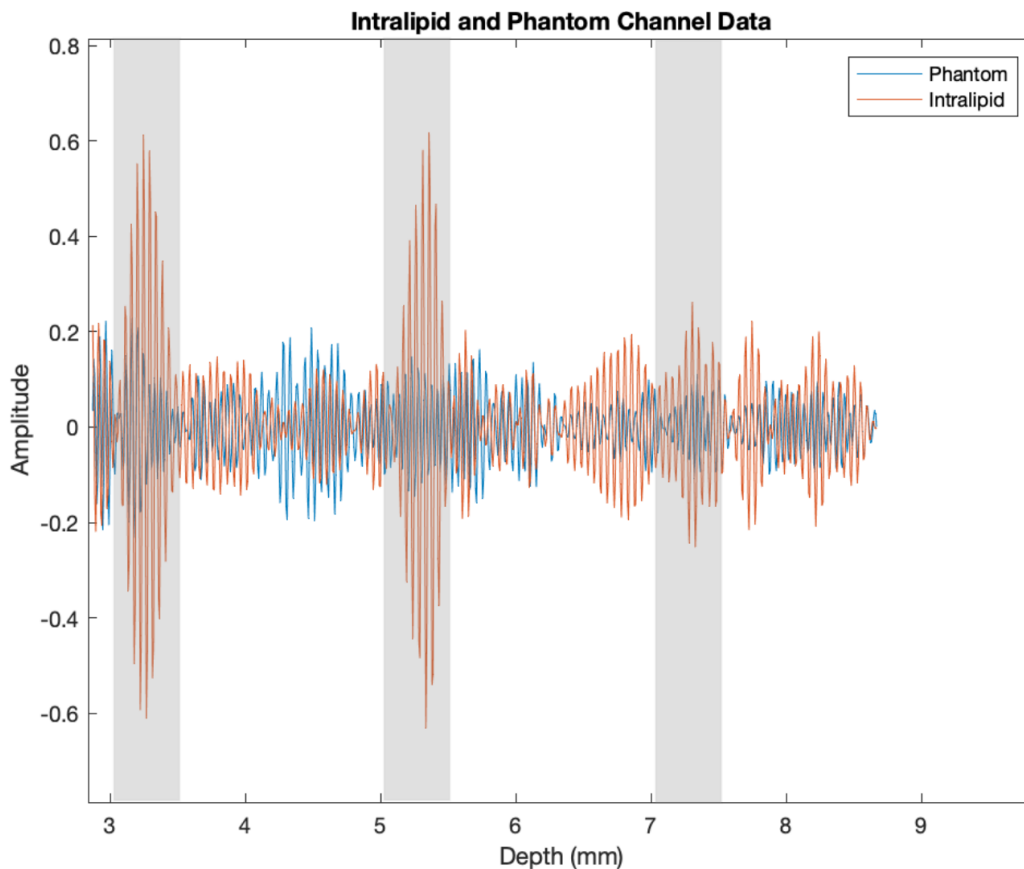


Figure 5.18: Amplitude of channel 42 for the tissue phantom and the intralipid and gelatin phantom versus depth (mm).

The attenuation of ultrasound due to backscattering in the tissue phantom with silica and intralipid was found to be 1.2 dB/mm. Since the photoacoustic signal is only attenuation with backscattering one-way, the attenuation of the photoacoustic signal would be half of this at 0.6 dB/mm. If we calculate the reduction in power at the depth of each hair due to this attenuation, we find that the signal is reduced by 1.8 times, 2.1 times, and 2.8

times, at 3.3 mm, 5.3 mm, and 7.3 mm respectively. This means that in order to bring the photoacoustic signal in the silica phantom above the noise we would need to increase the signal by approximately 2-3 times. This could be done by increasing the fluence which we could do by increasing the power of the laser, increasing the coupling efficiency, or using multiple lasers. Increasing the intensity of light reaching the photoacoustic target by 2-3 times should increase the signal enough to be visible in the silica and intralipid tissue phantom as well.

Chapter 6

Conclusion

The goal of this project was to demonstrate photoacoustic imaging in a high-frequency endoscopic ultrasound array meeting the dimensional requirements of minimally-invasive “keyhole” surgery. Collecting the photoacoustic signal for the transducers was done with a beamformer already designed and implemented for these transducers by altering their firmware and software to accommodate delay changes and averaging. Fiber optic cables were fixed to the arrays and a coupling system was designed to emit the laser light out of the tip of each endoscope. Finally, a tissue mimicking phantom was created to validate the photoacoustic endoscope’s imaging capabilities in the human brain. This project would aim to create 2D and 3D photoacoustic endoscopes designed for burr hole endoscopic brain surgery.

With the preliminary experiment using a single element transducer and a single hair target, we were able to obtain a very clear photoacoustic signal using 512 averages with an SNR of 7.8. This experiment showed that it was physically possible to produce a signal using our selected target and laser. These preliminary experiments also required that we focus the laser light on the hair target and produce enough fluence to observe a signal in the raw data because the signal was near the noise floor. Using this raw data we were able to determine the amount of averaging that would be needed to observe a photoacoustic signal when we implemented photoacoustic tomography into the existing ultrasound system in our lab.

Having a focused laser on the hair target and an idea of the amount of averaging required, we made changes to the firmware in order to trigger the laser and delay the data collection to capture the photoacoustic signal. Changes were made to the software so that we could average as long as we needed. With these changes a similar side illumination experiment was set up and image with the 40 MHz 64-element phased array transducer to produce 2D photoacoustic images with 1000 averages which took 5mins to acquire due to the technical limitations of the system. These images were optimized by reducing the side lobes of the resulting image with adaptive beamforming and summing weighted coherence factors. With

these changes we observed a lateral resolution of 0.165 mm which was 2.06 times the lateral resolution of the ultrasound signal.

Both of these experiments involved imaging a single hair mounted in water. The melanin in the hair has an absorption coefficient that is close to the absorption coefficient of blood for our purposes, however, the water does not accurately model how light and sound would scatter in brain tissue. In order to determine how our endoscope would perform in a realistic situation, a tissue mimicking phantom was created which had a photon reduced scattering coefficient close to 10 cm^{-1} and an ultrasound back scattering coefficient close to the backscattering of rat brain tissue. This was accomplished by using a mixture of 8% (mass/volume) of gelatin powder, 2% (mass/volume) of silica powder, deionized water, and 5% (volume/volume) of 20% intralipid emulsion. Following a specific heating and mixing procedure, the tissue mimicking phantom was then poured into a custom designed 3D printed mold which would hold hairs suspended in the phantom 2 mm apart both vertically and horizontally.

The tissue mimicking phantom was then tested to confirm that the ultrasound backscattering and the light scattering properties were, in fact, similar to the literature values of the brain. First, ultrasound images were taken of tissue phantoms with 0.5%, 1%, and 2% (mass/volume) of silica powder using a 50 MHz ultrasound transducer that had previously been used to image a rat brain. In sections of these images the root mean square (RMS) amplitudes were calculated and plotted along with the results from the image of the rat brain. These values were compared and all three were found to be consistent with the ultrasound backscattering in the rat brain. We therefore decided to use the largest percentage of 2% (mass/volume) silica. The reduced scattering coefficient was then measured by performing an experiment in which laser light was collimated and sent through a pinpoint aperture onto the surface of a phantom with only intralipid and a phantom with 2% silica and intralipid. By measuring distance between the center diffuse reflectance pattern and the incident beam, we calculated the reduced scattering coefficient to be $8.34 \pm 3 \text{ cm}^{-1}$ for the phantom with only intralipid and $8.29 \pm 3 \text{ cm}^{-1}$ for the phantom with intralipid and silica. These were both within range of the literature value of 10 cm^{-1} for brain tissue. Obtaining photoacoustic images with this tissue mimicking phantom which had similar photoacoustic properties to human brain tissue gives us a good idea of how these endoscopes would behave in real brain tissue thus verifying their use for this purpose.

With a tissue phantom to verify that the endoscopes would meet technical requirements for imaging in brain, the fiber optic cable bundle and laser coupling system was then designed to bring the laser light to the tip of the endoscope. Multimode glass fiber optic cables with a 200 μm diameter core and a 225 μm cladding were chosen and had a numerical aperture of 0.50. Thirty fibers were used so that 6 would be placed on each of the sides and 9 on both the front and back of the endoscope tip. These 30 fibers were arranged in a 3x10 configuration at the fiber bundle end so that they were close to the rectangular shape of the laser light outputted by the diode bar laser. A coupling system was designed to minimize the loss of light when incident on the 3x10 fiber bundle end. A 40 mm cylindrical lens was used to correct the astigmatism of the diode laser and a 35 mm spherical lens was used to focus the light down to a dimension of 0.5 mm by 2.0 mm. When incident on the 0.675 mm by 2.25 mm fiber bundle 17-34.0% was measured to be transmitted to the end of the fibers depending on the bundle used and the alignment. The fiber bundle fabricated for the 2D array had 17% coupling efficiency, and the fiber bundle for the 3D array had a coupling efficiency of 34%. This is due to the fact that more fibers were broken in the 2D array bundle and the fiber bundle end was less tightly packed. The fiber bundle was fabricated using wax and UV curing epoxy and the end was cleaved using a dicing saw so that the bundle interface had a flat surface. The transducer tip ends of the fibers were also assembled into flat groups of 6 and 9 and attached to the end of the endoscope using wax so that it could be removed.

This process proved to be challenging and the fibers were easily broken with 6 being broken on the bundle for the 2D endoscope and 2 being broken on the 3D endoscope. This process could potentially be improved in the future to allow for more precision and less broken fibers perhaps by creating 3D printed guides that could have attached right to the transducer tip. Since fabricated fiber bundles varied in coupling efficiency from 17 to 34%, improvements in this process could improve coupling efficiency and consistency in our fabricated endoscopes.

With the 2D 40 MHz and 3D 30MHz endoscopes fabricated with fiber optics, images of the tissue mimicking phantom were taken to verify their performance in tissue. First, an ultrasound image of the tissue mimicking phantom was taken using the 2D 40 MHz transducer to show the ability of the existing system to image three hair targets. The ultrasound backscattering in the image provided a lot of speckle that could make it difficult to visualize the hairs against the background scatter and gave a contrast of 22.8 dB. The

system was reconfigured to image with the photoacoustic firmware and software and the resulting photoacoustic image showed greatly improved contrast (42.3 dB) between the hair targets and the surrounding media due to the absence of signal from the parts of the phantom that did not contain hair. This improved contrast meets the goal of achieving photoacoustic images with a higher contrast than the ultrasound images due to the signal only coming from optical absorbers in the PAT images. This image also shows that there is a hair target at 8 mm in depth in the imaging window and indeed by increasing the gain on deeper images we are able to image up to the edge of the 10 mm imaging window of the ultrasound system.

Similarly, images were taken with the 3D 30 MHz endoscope starting with repeating the side illumination experiment that was performed with the 2D 40 MHz transducer. Photoacoustic images were created using the 3D endoscope and side illumination and the results were similar to the results obtained in the 2D endoscope experiments but the lateral resolution is lower at 30 MHz and the bias switching may have an effect on the image. Images were then taken with the 3D 30 MHz endoscope with attached fiber optics with hair in the tissue mimicking phantom. 10,000 averages were taken but no photoacoustic images were produced that could show the hair targets and the image was simply of filtered background noise. A new phantom with only intralipid and no silica was created to greatly reduce the attenuation due to backscattering of the photoacoustic signal and results were similar to the results obtained with the 2D endoscope but with a higher signal and a reduced amount of noise in the image. This gave a slightly higher contrast of 44.2 dB which also met the established contrast goal. With an ultrasound backscattering attenuation of 1.2 dB/mm, the photoacoustic signal would have an attenuation of 0.6 dB/mm meaning the signal in the phantom without silica would be 2-3 times the signal in the phantom with silica. In order for a photoacoustic image to be seen with this probe either a reduction in noise from the ultrasound system needs to occur including lowering the noise floor or the fluence needs to be increased by triggering the laser more frequently and acquiring more frequently. If we increased the photoacoustic signal in the silica and intralipid phantom by 3 times, we could achieve a photoacoustic signal in the silica-containing phantom as well.

Another issue is that in order to achieve these photoacoustic images 10,000 acquisitions needed to be averaged and this took approximately 50 minutes with the probe needing to be held still for that whole time. In order for the endoscope to be viable for surgery this acquisition time is far too long (1/3000 Hz) and it would need to be close to 1 Hz to be of

use. This long acquisition time was the same for images with the 2D 40 MHz and 3D 30 MHz endoscope in the tissue phantom and so the system would need to be significantly faster. The main bottle neck for this imaging length is the time it takes for the beamformer to acquire each acquisition which is slower than the laser can pulse. The beamformer could be programmed for real time imaging but was not at the time of these experiments. If these changes were made, the approach of this project is entirely compatible with real-time processing at 1000 pulses per second if the system could acquire this quickly. If 10,000 averages are needed to see an acceptable image and the fastest the laser can operate is 1000 Hz then if we could make this the bottle neck instead of the beamformer acquisition time then the best we could image at is 0.1 Hz which may be usable in surgery. For the single hair target which required 1000 averages the best we could do is 1 Hz which would be better. The shortest we could make the acquisition time theoretically is the time it would take for the sound to travel 10 mm in the medium which would be $6.76 \mu\text{s}$ which would be 148 kHz. Work is currently being done in our lab to improve the speed of the system and so if this is implemented these rates could potentially be reached. Another consideration is that we could use a more powerful laser or multiple lasers. If we increased optical power to still be within Maximum Permissible Exposure limits, we could increase laser output by approximately 2x before we hit the limit, increasing SNR by 6 dB [20]. With an increased optical output of only $\sqrt{10}$ x (3.16x), we could reduce the number of averages from 10,000 to 1000 making it possible to image at 1 FPS, making this system close to real-time and a viable imaging device for surgery. Alternatively, using another laser with a center frequency more closely matched to the 30 MHz center frequency could increase the signal by 26 dB relative to the signal amplitude obtained with the 7 MHz center frequency laser. Decreasing laser pulse duration with another laser or decreasing the transducer center frequency are possibly the easiest options for improving this performance. While we could achieve this 1 FPS frame rate, an issue that would arise if this system were used as a handheld device would be the introduction of motion artifacts. The necessity to average 1000 to 10,000 times would pose a significant issue and create motion artifacts, blurring the image we would capture. To help this, we could use an ultrasound probe more closely matched to our laser center frequency of 7 MHz which could increase the signal by 26 dB and could produce the same signal as with 400 averages in just one acquisition. Meaning we would need just 25 acquisitions to produce the same images as 10,000 acquisitions and could help reduce motion artifacts due to averaging.

This project shows it is possible to couple $>30\%$ of the light from a bar diode laser to the endoscope tip using glass multimode fiber optic cables and that this delivery system does not unacceptably grow the aperture of the endoscope. We also showed that the amount of light delivered is within 3 times the magnitude necessary to image a tissue mimicking phantom at 1 FPS which would meet the goal of being fast enough to be surgically useful (1 FPS). While improvements to SNR via increased laser output would allow us to image a tissue mimicking phantom, we have increased the contrast from 22.8 dB to 44.2 dB (surpassing the 22 dB contrast goal) and have not introduced any additional artefacts by performing photoacoustic tomography in this way. These observations allow us to conclude that with reasonable improvements in laser power, better alignment of the photoacoustic emission spectrum with the frequency response of the transducer, and/or improvements in beamformer noise, we could get this scheme to produce photoacoustic images in brain tissue at 1 FPS or better, with 44 dB or higher contrast, at up to 10 mm in depth.

To answer the question of whether photoacoustic imaging can be incorporated into a high frequency endoscopic phased array suitable for use in minimally invasive brain surgery, we have shown that it is possible to achieve acceptable images while staying within the form factor necessary for burr-hole surgery that has been established. However, further work needs to be done to improve SNR, acquire data in real-time at the rate of laser pulsing, and to ensure that the endoscope meets biocompatibility requirements necessary to be used on patients. To be biocompatible, the materials used must be shown to not produce a toxic or immune response when exposed to the body and the materials that have been added which would contact the body are glass fiber optic cables and the UV curing epoxy. While the silica based fiber optic cables should not pose a biocompatibility issue, the unknown composition of the UV curing epoxy would need to be tested to ensure it is safe for use internally in the brain. This additional work should include the ability for the device to be sterilized. With these changes, a complete photoacoustic endoscope could be fabricated for use in minimally invasive brain surgery.

Appendix A

Image Improvement Through Adaptive Beamforming

In ultrasound imaging, it is common practice to use a apodization function, such as a gaussian, across the elements to suppress the signal from elements on the edge of an array. This weighting of elements helps to reduce side lobes which cause artifacts in an image. However, this is not as effective in photoacoustic tomography due to the one-way nature of the signal. In order to improve photoacoustic signals, we looked to a method which uses adaptive beamforming techniques [22]. In this paper, they use four methods to beamform their photoacoustic data, a delay and sum method (DAS), a sum with the aperture weighted using a minimum variance method (MV), a sum weighted with coherence factors (CF), and a sum weighted with both the minimum variance and coherence factors. In the results that they obtained in figure A.1, we can see that the biggest improvement in image quality comes from implementing delay and sum beamforming weighted with coherence factors.

In order to implement this beamforming method, they consider for an ultrasound array of M elements, that the matrix $X(t) = [x_1(t) \cdots x_M(t)]$ gives the delayed data for each element at a given focus. Summing across this delayed data gives the delay and sum beamforming data for a given focus which is given by equation A.1.

$$b_{DAS}(t) = \sum_{m=0}^{M-1} x_m(t) \quad (\text{A.1})$$

This was the beamforming method used to obtain our original image in figure 3.19. In order to find the coherence factor at a given focus, Park et. al. use equation A.2 where the numerator gives the energy of the coherent sum and the denominator gives the sum of the incoherent energies of the delayed signals [17].

$$CF(t) = \frac{\left| \sum_{m=0}^{M-1} x_m(t) \right|^2}{M \sum_{m=0}^{M-1} |x_m(t)|^2} \quad (\text{A.2})$$

This means that the coherence factor ranges from 0 to 1 and signals that are incoherent

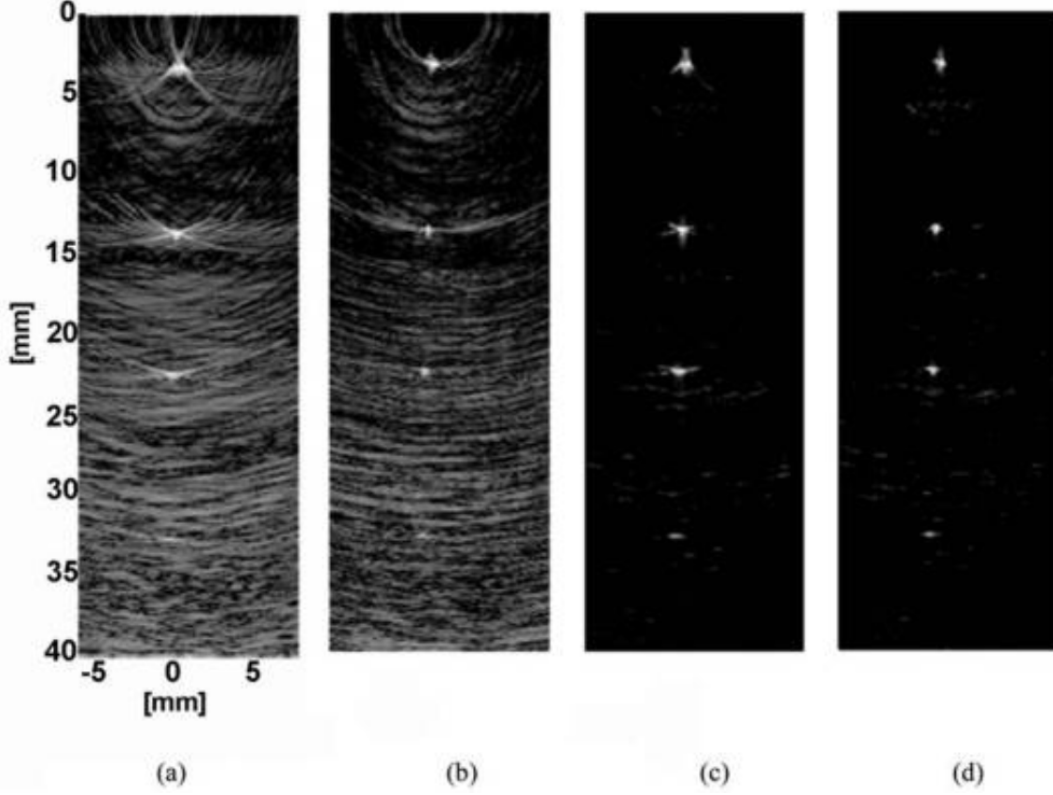


Figure A.1: Reconstructed photoacoustic images(35 dB log gray scale dynamic range, 14 mm laterally by 40 mm axially) of a phantom with four point targets using (a) DAS, (b) DAS+MV, (c) DAS+CF, and (d) DAS+CF+MV [22].

from one another are scaled by a low value due to the fact that they will destructively interfere and create a small numerator value. Scaling these incoherent signals reduces the effect of these incoherences on the image quality by minimizing signals that have these focusing errors and reducing the side lobes. Since noise is generally incoherent, this will also help to improve the SNR of our signal. To apply these weighting factors we simply multiply each factor by the delay and sum beamforming in equation A.1 as in equation A.3

$$b_{DAS+CF}(t) = CF(t) \sum_{m=0}^{M-1} x_m(t). \quad (\text{A.3})$$

Applying this coherence factor delay and sum beamforming technique to our photoacoustic results, we improve our photoacoustic images. We can see in these images that the side lobes have been dramatically reduced and the cross-sectional image of the hair more closely resembles a point target.

Appendix B

Copyright Agreement Letters

B.1 Figure 1.1

10/23/2020

RightsLink Printable License

SPRINGER NATURE LICENSE TERMS AND CONDITIONS

Oct 23, 2020

This Agreement between Dalhousie University -- Taylor Landry ("You") and Springer Nature ("Springer Nature") consists of your license details and the terms and conditions provided by Springer Nature and Copyright Clearance Center.

License Number	4935040599797
License date	Oct 23, 2020
Licensed Content Publisher	Springer Nature
Licensed Content Publication	Nature Methods
Licensed Content Title	High-speed label-free functional photoacoustic microscopy of mouse brain in action
Licensed Content Author	Junjie Yao et al
Licensed Content Date	Mar 30, 2015
Type of Use	Thesis/Dissertation
Requestor type	academic/university or research institute
Format	electronic
Portion	figures/tables/illustrations
Number of figures/tables/illustrations	1

<https://s100.copyright.com/AppDispatchServlet>

1/6

B.2 Figure 1.2

10/23/2020

RightsLink Printable License

AIP PUBLISHING LICENSE
TERMS AND CONDITIONS


Oct 23, 2020

This Agreement between Dalhousie University -- Taylor Landry ("You") and AIP Publishing ("AIP Publishing") consists of your license details and the terms and conditions provided by AIP Publishing and Copyright Clearance Center.

License Number	4935030486076
License date	Oct 23, 2020
Licensed Content Publisher	Acoustical Society of America
Licensed Content Publication	The Journal of the Acoustical Society of America
Licensed Content Title	Photoacoustic waves generated by absorption of laser radiation in optically thin cylinders
Licensed Content Author	M. I. Khan, T. Sun, G. J. Diebold
Licensed Content Date	Aug 1, 1993
Licensed Content Volume	94
Licensed Content Issue	2
Type of Use	Thesis/Dissertation
Requestor type	University or Educational Institution

B.3 Figure 1.4

10/23/2020 Rightslink® by Copyright Clearance Center



RightsLink®

Home
?
Email Support
Taylor Landry ▾



Requesting permission to reuse content from an IEEE publication

High power diode laser arrays

Author: J.G. Endriz

Publication: Quantum Electronics, IEEE Journal of

Publisher: IEEE

Date: April 1992

Copyright © 1992, IEEE

Thesis / Dissertation Reuse

The IEEE does not require individuals working on a thesis to obtain a formal reuse license, however, you may print out this statement to be used as a permission grant:

Requirements to be followed when using any portion (e.g., figure, graph, table, or textual material) of an IEEE copyrighted paper in a thesis:

- 1) In the case of textual material (e.g., using short quotes or referring to the work within these papers) users must give full credit to the original source (author, paper, publication) followed by the IEEE copyright line © 2011 IEEE.
- 2) In the case of illustrations or tabular material, we require that the copyright line © [Year of original publication] IEEE appear prominently with each reprinted figure and/or table.
- 3) If a substantial portion of the original paper is to be used, and if you are not the senior author, also obtain the senior author's approval.

Requirements to be followed when using an entire IEEE copyrighted paper in a thesis:

- 1) The following IEEE copyright/ credit notice should be placed prominently in the references: © [year of original publication] IEEE. Reprinted, with permission, from [author names, paper title, IEEE publication title, and month/year of publication]
- 2) Only the accepted version of an IEEE copyrighted paper can be used when posting the paper or your thesis on-line.
- 3) In placing the thesis on the author's university website, please display the following message in a prominent place on the website: In reference to IEEE copyrighted material which is used with permission in this thesis, the IEEE does not endorse any of [university/educational entity's name goes here]'s products or services. Internal or personal use of this material is permitted. If interested in reprinting/republishing IEEE copyrighted material for advertising or promotional purposes or for creating new collective works for resale or redistribution, please go to http://www.ieee.org/publications_standards/publications/rights/rights_link.html to learn how to obtain a License from RightsLink.

If applicable, University Microfilms and/or ProQuest Library, or the Archives of Canada may supply single copies of the dissertation.

BACK
CLOSE WINDOW

© 2020 Copyright - All Rights Reserved | [Copyright Clearance Center, Inc.](#) | [Privacy statement](#) | [Terms and Conditions](#)
Comments? We would like to hear from you. E-mail us at customer@copyright.com

B.4 Figure 3.4

10/23/2020

RightsLink Printable License

JOHN WILEY AND SONS LICENSE
TERMS AND CONDITIONS

Oct 23, 2020

This Agreement between Dalhousie University -- Taylor Landry ("You") and John Wiley and Sons ("John Wiley and Sons") consists of your license details and the terms and conditions provided by John Wiley and Sons and Copyright Clearance Center.

License Number	4935031359403
License date	Oct 23, 2020
Licensed Content Publisher	John Wiley and Sons
Licensed Content Publication	Laser & Photonics Reviews
Licensed Content Title	Photoacoustic microscopy
Licensed Content Author	Lihong V. Wang, Junjie Yao
Licensed Content Date	Jan 31, 2013
Licensed Content Volume	7
Licensed Content Issue	5
Licensed Content Pages	21
Type of use	Dissertation/Thesis

B.5 Figure 3.15

10/23/2020

RightsLink Printable License

JOHN WILEY AND SONS LICENSE
TERMS AND CONDITIONS

Oct 23, 2020

This Agreement between Dalhousie University -- Taylor Landry ("You") and John Wiley and Sons ("John Wiley and Sons") consists of your license details and the terms and conditions provided by John Wiley and Sons and Copyright Clearance Center.

License Number 4935040276532

License date Oct 23, 2020

Licensed Content
Publisher John Wiley and SonsLicensed Content
Publication Medical Physics

Licensed Content Title The Essential Physics of Medical Imaging

Licensed Content
Author Edward J. Goldschmidt, John M. Boone, Edwin M. Leidholdt, et al

Licensed Content Date Jul 2, 2003

Licensed Content
Volume 30

Licensed Content Issue 7

Licensed Content
Pages 1

Type of use Dissertation/Thesis

B.6 Figure 4.1 - Open Access License

10/23/2020

OSA | Author Resource Center: Copyright Transfer and Licensing Information



(<https://www.osapublishing.org>)



[« Back to Author Resource Home \(/author/author.cfm\)](#)

Author Resource Center

Copyright Transfer and Licensing Information

[Copyright Transfer](#) | [Open Access Licenses](#) | [Author and End-User Reuse Policy](#)
 (/submit/review/copyright_permissions.cfm#posting)

Copyright Transfer

OSA asks all authors of articles for its journals, magazines, and books to sign a Transfer of Copyright. In doing so, an author transfers ownership of his or her article or book to OSA. Ownership of copyright gives OSA the right to publish the article and to defend against improper use (or even theft) of the article. It also permits OSA to mount the article online or to use the article in other forms, such as when a journal article becomes part of a content collection or another derivative product.

OSA needs copyright for an article because, as publisher, the society is in the best position to defend the article legally. In addition, transfer of copyright assures OSA that the work in question is entirely the author's own. Once again, the purpose of transfer of copyright is not to prevent the author from reuse of his or her own work, as long as this doesn't involve republication in a competing journal or other competing resource.

If you send a manuscript to one of OSA's peer-reviewed journals, you will be given the opportunity during submission to agree to our electronic transfer of copyright, or our open access publishing agreement. You should print and send a hard copy of the below forms only if you are unwilling or unable to use the online option.

- [OSA Copyright Transfer Agreement \(PDF\) \(/submit/forms/copyxfer.pdf\)](#)
- [OSA Copyright Transfer and Open Access Publishing Agreement \(PDF\) \(/submit/review/pdf/OSACopyTransferOAAgrmnt\(2017-09-05\).pdf\)](#)
- [Photonics Research Copyright Transfer Agreement \(PDF\) \(/submit/review/pr-copyright-transfer.pdf\)](#)

Open Access Licenses

B.7 Figure 4.5 - Open Access License

10/23/2020

OSA | Author Resource Center: Copyright Transfer and Licensing Information



(<https://www.osapublishing.org>)



[« Back to Author Resource Home \(/author/author.cfm\)](/author/author.cfm)

Author Resource Center

Copyright Transfer and Licensing Information

[Copyright Transfer](#) | [Open Access Licenses](#) | [Author and End-User Reuse Policy](#)
 (/submit/review/copyright_permissions.cfm#posting)

Copyright Transfer

OSA asks all authors of articles for its journals, magazines, and books to sign a Transfer of Copyright. In doing so, an author transfers ownership of his or her article or book to OSA. Ownership of copyright gives OSA the right to publish the article and to defend against improper use (or even theft) of the article. It also permits OSA to mount the article online or to use the article in other forms, such as when a journal article becomes part of a content collection or another derivative product.

OSA needs copyright for an article because, as publisher, the society is in the best position to defend the article legally. In addition, transfer of copyright assures OSA that the work in question is entirely the author's own. Once again, the purpose of transfer of copyright is not to prevent the author from reuse of his or her own work, as long as this doesn't involve republication in a competing journal or other competing resource.

If you send a manuscript to one of OSA's peer-reviewed journals, you will be given the opportunity during submission to agree to our electronic transfer of copyright, or our open access publishing agreement. You should print and send a hard copy of the below forms only if you are unwilling or unable to use the online option.

- [OSA Copyright Transfer Agreement \(PDF\) \(/submit/forms/copyxfer.pdf\)](/submit/forms/copyxfer.pdf)
- [OSA Copyright Transfer and Open Access Publishing Agreement \(PDF\) \(/submit/review/pdf/OSACopyTransferOAAgrmnt\(2017-09-05\).pdf\)](/submit/review/pdf/OSACopyTransferOAAgrmnt(2017-09-05).pdf)
- [Photonics Research Copyright Transfer Agreement \(PDF\) \(/submit/review/pr-copyright-transfer.pdf\)](/submit/review/pr-copyright-transfer.pdf)

Open Access Licenses

Bibliography

- [1] Andre Bezanson, Rob Adamson, and Jeremy A Brown. Fabrication and performance of a miniaturized 64-element high-frequency endoscopic phased array. *IEEE transactions on ultrasonics, ferroelectrics, and frequency control*, 61(1):33–43, 2014.
- [2] Jeremy Brown. Principles of medical imaging - class notes.
- [3] JT Bushberg, JA Seibert, EM Leidholdt, JM Boone, and Mahadevappa Mahesh. The essential physics of medical imaging. *Medical physics*, 40(7):077301, 2013.
- [4] Ryan KW Chee, Peiyu Zhang, Mohammad Maadi, and Roger J Zemp. Multifrequency interlaced cmuts for photoacoustic imaging. *IEEE transactions on ultrasonics, ferroelectrics, and frequency control*, 64(2):391–401, 2016.
- [5] Jason R Cook, Richard R Bouchard, and Stanislav Y Emelianov. Tissue-mimicking phantoms for photoacoustic and ultrasonic imaging. *Biomedical optics express*, 2(11):3193–3206, 2011.
- [6] Martin O Culjat, David Goldenberg, Priyamvada Tewari, and Rahul S Singh. A review of tissue substitutes for ultrasound imaging. *Ultrasound in medicine & biology*, 36(6):861–873, 2010.
- [7] Khalid Daoudi, PJ Van Den Berg, O Rabot, A Kohl, S Tisserand, P Brands, and Wiendelt Steenbergen. Handheld probe integrating laser diode and ultrasound transducer array for ultrasound/photoacoustic dual modality imaging. *Optics express*, 22(21):26365–26374, 2014.
- [8] John G Endriz, Mitral Vakili, Gerald S Browder, Mark DeVito, James M Haden, Gary L Harnagel, WE Plano, Masamichi Sakamoto, David F Welch, Steven Willing, et al. High power diode laser arrays. *IEEE Journal of quantum electronics*, 28(4):952–965, 1992.
- [9] Stephen T Flock, Steven L Jacques, Brian C Wilson, Willem M Star, and Martin JC van Gemert. Optical properties of intralipid: a phantom medium for light propagation studies. *Lasers in surgery and medicine*, 12(5):510–519, 1992.
- [10] Glen D Gillen and Shekhar Guha. Modeling and propagation of near-field diffraction patterns: a more complete approach. *American journal of physics*, 72(9):1195–1201, 2004.
- [11] George M Hale and Marvin R Query. Optical constants of water in the 200-nm to 200- μm wavelength region. *Applied optics*, 12(3):555–563, 1973.
- [12] Shawn L Hervey-Jumper and Mitchel S Berger. Awake craniotomy: Cortical and sub-cortical mapping for glioma resection. In *Epilepsy Surgery and Intrinsic Brain Tumor Surgery*, pages 137–145. Springer, 2019.

- [13] Nesrine Houhat and Tarek Boutkedjirt. Frequency and concentration dependence of the ultrasonic backscatter coefficient in a soft tissue mimicking material. In *Acoustics 2012*, 2012.
- [14] Steven L Jacques. Optical properties of biological tissues: a review. *Physics in Medicine & Biology*, 58(11):R37, 2013.
- [15] MI Khan, T Sun, and GJ Diebold. Photoacoustic waves generated by absorption of laser radiation in optically thin cylinders. *The Journal of the Acoustical Society of America*, 94(2):931–940, 1993.
- [16] Puxiang Lai, Xiao Xu, and Lihong V Wang. Dependence of optical scattering from intralipid in gelatin-gel based tissue-mimicking phantoms on mixing temperature and time. *Journal of biomedical optics*, 19(3):035002, 2014.
- [17] C-K Liao, M-L Li, and P-C Li. Optoacoustic imaging with synthetic aperture focusing and coherence weighting. *Optics letters*, 29(21):2506–2508, 2004.
- [18] Shao-Pow Lin, Lihong Wang, Steven L Jacques, and Frank K Tittel. Measurement of tissue optical properties by the use of oblique-incidence optical fiber reflectometry. *Applied optics*, 36(1):136–143, 1997.
- [19] Yajing Liu, Liming Nie, and Xiaoyuan Chen. Photoacoustic molecular imaging: from multiscale biomedical applications towards early-stage theranostics. *Trends in biotechnology*, 34(5):420–433, 2016.
- [20] Anil K Maini. *Lasers and optoelectronics: fundamentals, devices and applications*. John Wiley & Sons, 2013.
- [21] D Nicholas. Evaluation of backscattering coefficients for excised human tissues: results, interpretation and associated measurements. *Ultrasound in Medicine and Biology*, 8(1):17–28, 1982.
- [22] Suhyun Park, Andrei B Karpiouk, Salavat R Aglyamov, and Stanislav Y Emelianov. Adaptive beamforming for photoacoustic imaging. *Optics letters*, 33(12):1291–1293, 2008.
- [23] Axel Perneczky and Georg Fries. Endoscope-assisted brain surgery: part 1—evolution, basic concept, and current technique. *Neurosurgery*, 42(2):219–224, 1998.
- [24] PK Pillay, SJ Hassenbusch, and R Sawaya. Minimally invasive brain surgery. *Annals of the Academy of Medicine, Singapore*, 22(3 Suppl):459–463, 1993.
- [25] Eugenio Pozzati, Giuliano Giuliani, Giacomo Nuzzo, and Massimo Poppi. The growth of cerebral cavernous angiomas. *Neurosurgery*, 25(1):92–97, 1989.
- [26] Shigemi Saito, Yasuhiro Shibata, Akira Ichiki, and Akiho Miyazaki. Measurement of sound speed in thread. *Japanese journal of applied physics*, 45(5S):4521, 2006.

- [27] Christopher Samson, Thomas Landry, and Jeremy A Brown. Minimally invasive in vivo functional ultrasound imaging using a 40 mhz phased array endoscope: Mapping the auditory response in rats. In *2019 IEEE International Ultrasonics Symposium (IUS)*, pages 2141–2144. IEEE, 2019.
- [28] Christopher A Samson, Katherine Latham, and Jeremy A Brown. Real-time, 45 mhz, split-aperture phased array beamformer with efficient sign coherence grating lobe suppression. In *2016 IEEE International Ultrasonics Symposium (IUS)*, pages 1–4. IEEE, 2016.
- [29] J Marc Simard, Garcia-Bengochea Francisco, William E Ballinger Jr, J Parker Mickle, and Ronald G Quisling. Cavernous angioma: a review of 126 collected and 12 new clinical cases. *Neurosurgery*, 18(2):162–172, 1986.
- [30] Paul Kumar Upputuri and Manojit Pramanik. Performance characterization of low-cost, high-speed, portable pulsed laser diode photoacoustic tomography (pld-pat) system. *Biomedical optics express*, 6(10):4118–4129, 2015.
- [31] Lihong Wang and Steven L Jacques. Use of a laser beam with an oblique angle of incidence to measure the reduced scattering coefficient of a turbid medium. *Applied optics*, 34(13):2362–2366, 1995.
- [32] LV Wang and H-i Wu. *Biomedical optics: Principles and imaging*. Wiley, 2007.
- [33] Robert C Weast and Melvin J Astle. *CRC Handbook of Chemistry and Physics...: 1983-1984*. CRC press, 1983.
- [34] Eric W Weisstein. ” gaussian function,” mathworld-a wolfram web resource. <http://mathworld.wolfram.com/GaussianFunction.html>, 2009.
- [35] Jun Xia, Junjie Yao, and Lihong V Wang. Photoacoustic tomography: principles and advances. *Electromagnetic waves (Cambridge, Mass.)*, 147:1, 2014.
- [36] Da-Kang Yao, Chi Zhang, Konstantin I Maslov, and Lihong V Wang. Photoacoustic measurement of the grüneisen parameter of tissue. *Journal of biomedical optics*, 19(1):017007, 2014.
- [37] Junjie Yao, Lidai Wang, Joon-Mo Yang, Konstantin I Maslov, Terence TW Wong, Lei Li, Chih-Hsien Huang, Jun Zou, and Lihong V Wang. High-speed label-free functional photoacoustic microscopy of mouse brain in action. *Nature methods*, 12(5):407, 2015.
- [38] Junjie Yao and Lihong V. Wang. Photoacoustic microscopy. *Laser and Photonics Reviews*, 7(5):758–778, 2013.
- [39] Junjie Yao and Lihong V Wang. Photoacoustic brain imaging: from microscopic to macroscopic scales. *Neurophotonics*, 1(1):011003, 2014.
- [40] Junjie Yao and Lihong V Wang. Sensitivity of photoacoustic microscopy. *Photoacoustics*, 2(2):87–101, 2014.

- [41] Richard M Young, Aria Jamshidi, Gregory Davis, and Jonathan H Sherman. Current trends in the surgical management and treatment of adult glioblastoma. *Annals of translational medicine*, 3(9), 2015.
- [42] Qizhi Zhang, Zhao Liu, Paul R Carney, Zhen Yuan, Huanxin Chen, Steven N Roper, and Huabei Jiang. Non-invasive imaging of epileptic seizures in vivo using photoacoustic tomography. *Physics in Medicine & Biology*, 53(7):1921, 2008.